Doctoral Dissertation

Tuning of Characteristic Electronic States in Cerium and Uranium Compounds by High Pressures and High Magnetic Fields

Miho Nakashima

Department of Physics, Graduate School of Science
Osaka University

June, 2004

Abstract

The f electrons of cerium and uranium compounds exhibit a variety of characteristic features including spin and valence fluctuations, heavy fermions and anisotropic superconductivity. In these compounds, the RKKY interaction and the Kondo effect compete with each other. The former interaction enhances the long-range magnetic order, while the latter effect quenches the magnetic moments of the localized f electrons by the spin polarization of the conduction electrons. The electronic states thus depend strongly on the temperature. These unique electronic states are, however, tuned by high pressures and high magnetic fields.

The pressure experiments were demonstrated for antiferromagnets $CeNiGe_3$, $CeNi_2Al_5$, $UNiGa_5$, $UPdGa_5$, $UPtGa_5$, UN and UGa_3, and a ferromagnet $CeAgSb_2$. The magnetic ordering temperature decreases with increasing pressure, and becomes zero at a critical pressure P_c, for example $P_c \simeq 5.5$ GPa in $CeNiGe_3$. The experimental results of $CeNiGe_3$ indicated clearly that a $4f$-localized nature in the antiferromagnetic state of $CeNiGe_3$ is changed into a non-magnetic $4f$-itinerant state, passing through the heavy fermion state at P_c. The crossover from localized to itinerant in the f electron system is also found to be tuned by applying pressure for $CeNi_2Al_5$, $UNiGa_5$, $UPdGa_5$, $UPtGa_5$, UN and UGa_3.

The magnetic susceptibility in URu_2Si_2 and UPt_3 increases with decreasing temperature, following the Curie-Weiss law at high temperatures, and has a maximum at a characteristic temperature $T_{\chi max}$, which approximately corresponds to the Kondo temperature. Below $T_{\chi max}$, the susceptibility becomes almost temperature-independent, and the electronic state of the f electron system is changed into a heavy fermion state. The heavy fermion state, where the f electrons are itinerant, is also tuned by high magnetic fields. Namely, the crossover from the f-itinerant state to the almost localized f electron state occurs at a critical magnetic field H_m, indicating a metamagnetic transition in the magnetization curve. The crossover from itinerant to localized is tuned by applying high magnetic fields $H_m = 40$ T in URu_2Si_2 and $H_m = 20$ T in UPt_3. In the present study it was clarified that the metamagnetism persists up to $T_{\chi max}$: 60 K in URu_2Si_2 and 30 K in UPt_3.

Contents

List of Figures

1 Introduction

The f electrons of rare earth compounds exhibit a variety of characteristics including spin and valence fluctuations, spin and charge orderings, heavy fermions, Kondo insulators and anisotropic superconductivity. In the cerium compounds, the Ruderman-Kittel-Kasuya-Yosida (RKKY) interaction and the Kondo effect compete with each other [1)]. The former interaction enhances the long-range magnetic order, where the $4f$ electrons with the magnetic moments are treated as localized electrons and the indirect f-f interaction is mediated by the conduction electrons with spins. On the other hand, the latter effect quenches the magnetic moments of the localized $4f$ electrons by the spin polarization of the conduction electrons, consequently producing the singlet state with the binding energy $k_{\rm B}T_{\rm K}$, where $T_{\rm K}$ is called the Kondo temperature, which leads to the heavy fermion state with an extremely large effective mass at lower temperatures than $T_{\rm K}$. The similar phenomena were also observed in the $5f$ electron system of uranium compounds.

Competition between the RKKY interaction and the Kondo effect was discussed by Doniach [2)] in terms of a function of $|J_{cf}|D(\varepsilon_{\rm F})$, where $|J_{cf}|$ is a magnitude of the magnetic exchange interaction and $D(\varepsilon_{\rm F})$ is the electronic density of states at the Fermi energy $\varepsilon_{\rm F}$. Most of the cerium compounds order magnetically, because the RKKY interaction overcomes the Kondo effect at low temperatures. On the other hand, some cerium compounds such as $CeCu_6$ and $CeRu_2Si_2$ indicate no long-range magnetic order [1)].

Recently a new aspect of the cerium and uranium compounds with the antiferromagnetic ordering has been revealed. When pressure P is applied to the compounds such as $CeIn_3$ and $CePd_2Si_2$ [3)], the Néel temperature $T_{\rm N}$ decreases and the quantum critical point corresponding to the extrapolation $T_{\rm N} \to 0$ is reached at $P = P_{\rm c}$. Here, $|J_{cf}|D(\varepsilon_{\rm F})$ in the Doniach model can be replaced by the pressure. Surprisingly, superconductivity and/or non-Fermi liquid character appear around $P_{\rm c}$. Correspondingly, the heavy fermion state is formed as P approaches $P_{\rm c}$. Similar pressure-induced superconductivity was also reported for $CeCu_2Ge_2$ [4)], $CeRhIn_5$ [5)] and UGe_2 [6, 7)].

In this paper we studied the electronic state near the quantum critical region in cerium and uranium compounds by measuring the electrical resistivity under high pressures. We also studied the de Haas-van Alphen (dHvA) effect of URu_2Si_2 under high pressures, and magnetization of URu_2Si_2 and UPt_3 in high magnetic fields . We will clarify the characteristic electronic states tuned by high pressures and high magnetic fields in cerium compounds of $CeNiGe_3$, $CeNi_2Al_5$ and $CeAgSb_2$ and also uranium compounds of $UTGa_5$(T: Ni, Pd, Pt), UN, UGa_3, URu_2Si_2 and UPt_3.

In Chap. 2, we will give a review including more detail background of this study and the characteristic properties of the compounds of $CeNiGe_3$, $CeNi_2Al_5$, $CeAgSb_2$, $UTGa_5$(T: Ni, Pd, Pt), UN, UGa_3, URu_2Si_2 and UPt_3. In Chap. 3, we will give the experimental methods of electrical resistivity and dHvA effect under pressure, and also the pulse-field magnetization. Next, we will present the experimental results in the present study in Chap. 4. Finally, we will summarize and conclude the present study in Chap. 5.

2 Reveiw of Relevant Physics

2.1 General property of the f electron systems

The $4f$ electrons in the Ce atom are pushed into the interior of the closed $5s$ and $5p$ shells because of the strong centrifugal potential $l\,(l+1)/r^2$, where $l=3$ holds for the f electrons. This is a reason why the $4f$ electrons possess an atomic-like character in the crystal [8]. On the other hand, the tail of their wave function spreads to the outside of the closed $5s$ and $5p$ shells, which is highly influenced by the potential energy, the relativistic effect and the distance between the Ce atoms. This results in the hybridization of the $4f$ electrons with the conduction electrons. These cause various phenomena such as valence fluctuations, Kondo lattice, heavy fermion, Kondo insulator and unconventional superconductivity.

The Coulomb repulsive force of the $4f$ electron at the same atomic site, U, is so strong, e.g., $U \simeq 5$ eV in the Ce compounds (see Fig. 2.1), that occupancy of a same site by two $4f$ electrons is usually prohibited.

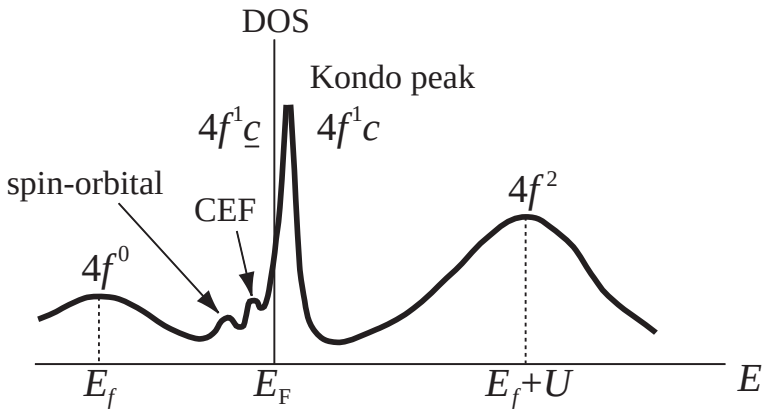

Fig. 2.1 Density of states (DOS) of the $4f$ electron in the Ce compound (Ce^{3+}).

In the Ce compounds the tail of the $4f$ partial density of states extends to the Fermi level even at room temperature, and thus the $4f$ level approaches the Fermi level in energy and the $4f$ electrons hybridize strongly with the conduction electrons. This $4f$-hybridization coupling constant is denoted by V_{cf}. When U is strong and V_{cf} is ignored, the freedom of the charge in the $4f$ electron is suppressed, while the freedom of the spin is retained, representing the $4f$-localized state. Naturally, the degree of localization depends on the level of the $4f$ electrons E_f, where larger E_f helps to increase the localization. This situation is applied to most of the lanthanide compounds in which Ruderman-Kittel-Kasuya-Yosida (RKKY) interaction play a predominant role in magnetism [9, 10, 11]. The mutual magnetic interaction between the $4f$ electrons occupying different atomic sites cannot be of a direct type such as $3d$ metal magnetism, but should be indirect one, which occurs only through the conduction electrons.

In the RKKY interaction, a localized spin S_i interacts with a conduction electron with spin s, which leads to a spin polarization of the conduction electron. This polarization interacts with another spin S_j localized on an ion j and therefore creates an indirect interaction between the spins S_i and S_j. This indirect interaction extends to the far distance and damps with a sinusoidal $2k_{\mathrm{F}}$ oscillation, where k_{F} is half of the caliper dimension of the Fermi surface. When the number of $4f$ electrons increases in such a way that the lanthanide element changes from Ce to Gd or reversely from Yb to Gd in the compound, the magnetic moment becomes larger and the RKKY interaction stronger, leading to the magnetic order. The ordering temperature roughly follows the de Gennes relation, $(g_J - 1)^2 J(J + 1)$. Here g_J is the Landé g-factor and J is the total angular momentum.

2.1.1 Dense Kondo effect

Contrary to what happens at a large U, higher V_{cf} tends to enhance the hybridization of the $4f$ electrons with conduction electrons, thus accelerating the delocalization of the $4f$ electrons. The delocalization of the $4f$ electrons tends to make the $4f$ band wide. When $E_f > V_{cf}$, the $4f$ electrons are still better localized and the Kondo regime are expected in the Ce compounds.

The study of Kondo effect began when a low temperature resistance minimum was found for non-magnetic metals with ppm-order magnetic impurities. Kondo showed theoretically that the logarithmic resistivity increase at low temperatures as a result of the spin-flip scattering of the conduction electrons by the localized magnetic moments of impurities [12]. In the $3d$-based dilute alloys, the magnetic impurity Kondo effects can be observed only in the case of very low concentration $3d$ magnetic impurities. This is because the degeneracy of the localized spins is very important for the Kondo effect. When the concentration of $3d$ magnetic impurities is increased, the $3d$ elements would come near each other and thus the overlapping or interaction between $3d$ shells would occur, which would lift the degeneracy of the impurity spin and suppress the Kondo spin-flip process.

Since the observation of the $\rho(T) \sim -\log T$ dependence in $CeAl_2$ by Buschow *et al.* [13], many rare earth compounds, in particular, Ce compounds were found to show the anomalous behavior similar to the impurity Kondo effect. In these compounds, the $4f$ ions have very high concentration and can even form the crystalline lattice with the anions and thus it cannot be considered as the impurities. From the appearance of a Kondo-like behavior, this phenomenon is called the dense Kondo effect.

The property of the dense Kondo effect at high temperatures is the same as that of the dilute system, but at low temperatures it is quite different in behavior. For instance, we show in Fig. 2.2 the temperature dependence of the electrical resistivity in $Ce_xLa_{1-x}Cu_6$ [14]. This resistivity increases logarithmically with decreasing the temperature for all range of concentration. The Kondo effect occurs independently at each Ce site, because the slope of the logarithmically curve is almost proportional to the concentration of Ce. In $CeCu_6$ the behavior is, however, very different from the dilute Kondo impurity

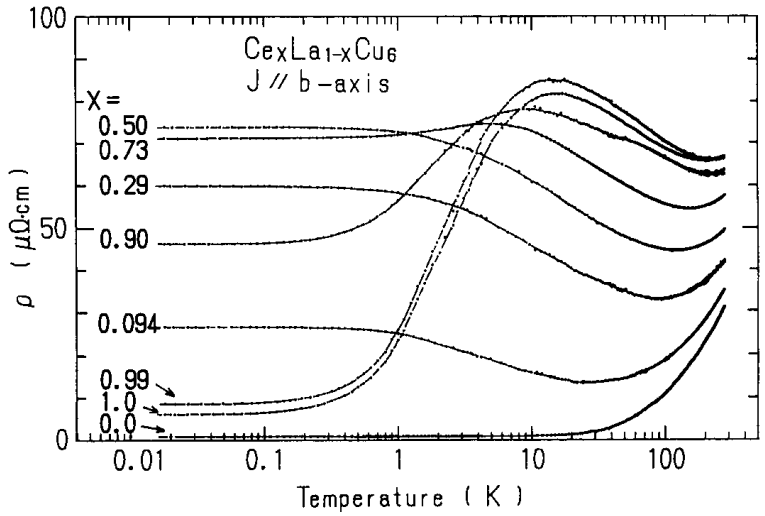

Fig. 2.2 Temperature dependence of the electrical resistivity in $Ce_xLa_{1-x}Cu_6$ [14].

system. The resistivity increases with decreasing the temperature, forms a maximum around 15 K and decrease rapidly at lower temperatures to a unitary limit value. This behavior is in contrast to the dilute system characterized by a resistivity minimum.

The many-body Kondo bound state is now understood as follows: For the simplest case of no orbital degeneracy, the localized spin $S(\uparrow)$ is coupled antiferromagnetically with the conduction electrons $s(\downarrow)$. Consequently the singlet state $\{S(\uparrow)\cdot s(\downarrow) \pm S(\downarrow)\cdot s(\uparrow)\}$ is formed with the binding energy $k_{\rm B}T_{\rm K}$. Here the Kondo temperature $T_{\rm K}$ is the single energy scale. In other words, disappearance of the localized moment is thought to be due to the formation of a spin-compensating cloud of the electrons around the impurity moment.

The Kondo temperature in the Ce compounds is large compared to the magnetic ordering temperature based on the RKKY interaction. For example, the Ce ion is trivalent ($J=\frac{5}{2}$) and the $4f$ energy level is split into the three doublets by the crystalline electric field, namely possessing the splitting energy of Δ_1 and Δ_2, as shown in Fig. 2.3.

The Kondo temperature is given as follows [15]:

$$T_{\rm K}^{\rm h} = D\exp\left(-\frac{1}{3|J_{cf}|D(E_{\rm F})}\right) \qquad \text{when } T > \Delta_1, \Delta_2, \tag{2.1}$$

and

$$T_{\rm K} = \frac{D^2}{\Delta_1\Delta_2} D\exp\left(-\frac{1}{|J_{cf}|D(E_{\rm F})}\right) \quad \text{when } T < \Delta_1, \Delta_2. \tag{2.2}$$

Here D, $|J_{cf}|$ and $D(E_{\rm F})$ are the band width, exchange energy and the density of states at the Fermi energy $E_{\rm F}$, respectively. If we assume $T_{\rm K} \simeq 5$ K, for $D = 10^4$ K,

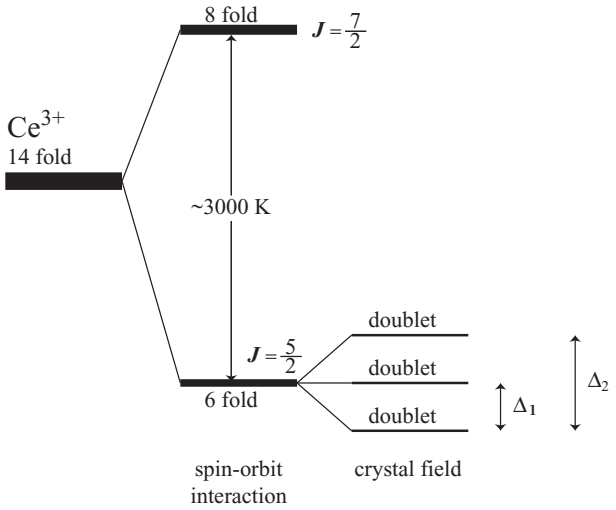

Fig. 2.3 Level scheme of the $4f$ electron in Ce^{3+}.

$\Delta_1 = 100$ K and $\Delta_2 = 200$ K, the value of $T_K^h \simeq 50$ K is obtained, which is compared to the $S = \frac{1}{2}$-Kondo temperature of 10^{-3} K defined as $T_K^0 = D\exp(-1/|J_{cf}|D(E_F))$. These large values of the Kondo temperature shown in eqs. (2.1) and (2.2) are due to the orbital degeneracy of the $4f$ levels. Therefore, even at low temperatures the Kondo temperature is not T_K^0 but T_K shown in eq. (2.2).

On the other hand, the magnetic ordering temperature is about 5 K in the Ce compounds, which can be simply estimated from the de Gennes relation under the consideration of the Curie temperature of about 300 K in Gd. Therefore, it depends on the compound whether magnetic ordering occurs at low temperatures or not.

2.1.2 Heavy fermion system

The ground state properties of the dense Kondo system are interesting in magnetism, which are highly different from the dilute Kondo system. In the cerium intermetallic compounds such as $CeCu_6$, cerium ions are periodically aligned whose ground state cannot be a scattering state but becomes a coherent Kondo-lattice state.

The effective mass of the conduction electron in the Kondo lattice of $CeCu_6$ is extremely large, compared with the one of the free electron. It is reflected in the specific heat coefficient γ and magnetic susceptibility $\chi(0)$, which can be expressed as

$$\gamma = \frac{2\pi^2 {k_B}^2}{3} D(E_F) \tag{2.3a}$$

$$= \frac{{k_B}^2 k_F}{3\hbar^2} m^* \qquad \text{(free electron model)}, \tag{2.3b}$$

and

$$\chi(0) = 2{\mu_\mathrm{B}}^2 D(E_\mathrm{F}) \tag{2.4a}$$

$$= {\mu_\mathrm{B}}^2 \frac{k_\mathrm{F}}{\pi^2\hbar^2} m^* \quad \text{(free electron model)}, \tag{2.4b}$$

where k_F is Fermi wave number. These parameters are proportional to the effective mass. The electrical resistivity ρ decreases steeply with decreasing the temperature, following a Fermi liquid behavior as $\rho \sim AT^2$ with a large value of the coefficient A [16]. The $\sqrt{A}$ value is proportional to the effective mass of the carrier m^* and thus inversely proportional to the Kondo temperature. Correspondingly, the electronic specific heat coefficient γ roughly follows the simple relation $\gamma \sim 10^4/T_\mathrm{K}$ (mJ/K^2·mol) because the Kramers doublet of the $4f$ levels is changed into the γ value in the Ce compound:

$$R\log 2 = \int_0^{T_\mathrm{K}} \frac{C}{T}\mathrm{d}T, \tag{2.5}$$

$$C = \gamma T, \tag{2.6}$$

thus

$$\gamma = \frac{R\log 2}{T_\mathrm{K}} = \frac{5.8\times 10^3}{T_\mathrm{K}}\ (\mathrm{mJ/K^2{\cdot}mol}). \tag{2.7}$$

It reaches 1600 mJ/K^2·mol for $CeCu_6$ [17] because of a small Kondo temperature of 4–5 K. The conduction electrons possess large effective masses and thus move slowly in the crystal. Actually in $CeRu_2Si_2$ an extremely heavy electron of $120m_0$ was detected from the de Haas-van Alphen (dHvA) effect measurements [18, 19]. Therefore the Kondo-lattice system is called a heavy fermion or heavy electron system. The Ce Kondo-lattice compound with magnetic ordering also possesses the large γ value even if the RKKY interaction overcomes the Kondo effect at low temperatures. For example, the γ value of CeB_6 is 250 mJ/K^2·mol [20], which is roughly one hundred times as large as that of LaB_6, 2.6 mJ/K^2·mol [21]. The heavy fermion state is also realized in the uranium compounds with $5f$ electrons.

A significant correlation factor is thought to be the ratio of the measured magnetic susceptibility $\chi(0)$ to the observed γ value:

$$R_\mathrm{W} \equiv \left(\frac{\pi^2{k_\mathrm{B}}^2}{\gamma}\right)\left(\frac{\chi(0)}{{\mu_\mathrm{B}}^2 {g_J}^2 J(J+1)}\right). \tag{2.8}$$

This ratio R_W is called Wilson-Sommerfeld ratio. Stewart [22] evaluated R_W for the heavy fermion system of cerium and uranium compounds, as shown in Fig. 2.4. He suggested that in the f electron system R_W is not 1 but roughly 2. Kadowaki and Woods stressed the importance of a universal relationship between A and γ as shown in Fig. 2.5 [23]. They noted that the ration A/γ has a common value of 1.0×10^{-5} $\mu\Omega$·cm·K^2·mol^2/mJ^2.

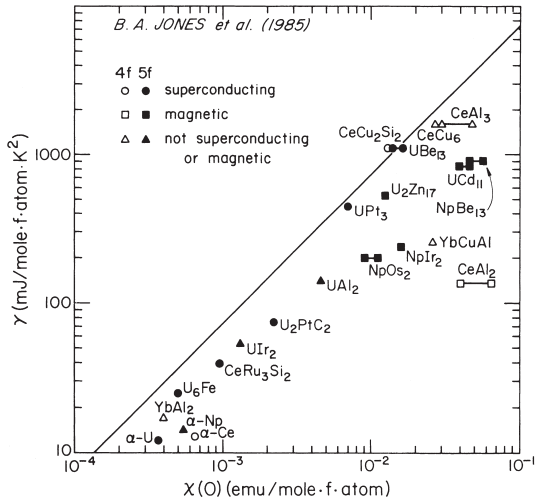

Fig. 2.4 The specific heat coefficient versus the susceptibility for some heavy fermion systems. The values are extrapolated to zero by a variety of methods. Any free, noninteracting fermion gas would lie on the straight line [24].

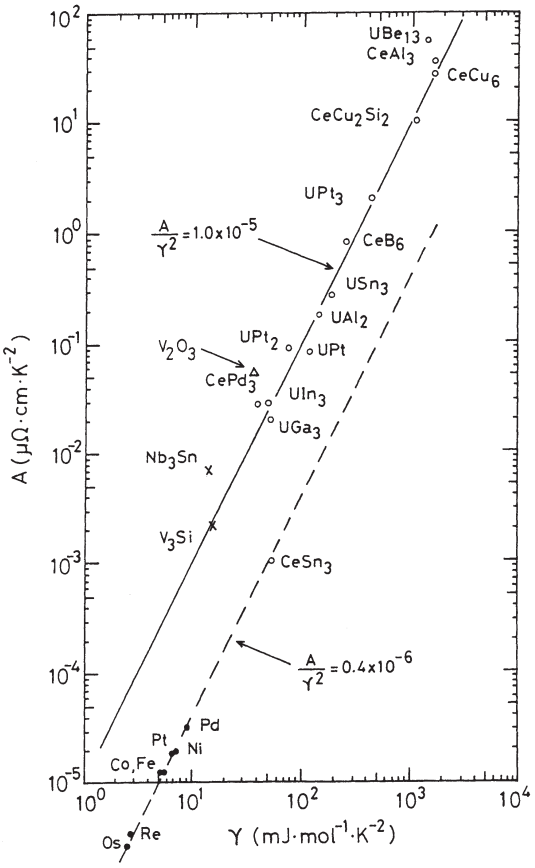

Fig. 2.5 A vs γ in the logarithmic scale [25].

2.1.3 Competition between the RKKY interaction and the Kondo effect

The Kondo effect can be parameterized by a single energy scale $T_{\rm K}$. The hierarchy of ordering temperatures can be qualitatively understood by a competition between the Kondo screening and the tendency towards magnetic ordering via RKKY-type indirect exchange mechanism. The magnitude of an indirect RKKY interaction can be characterized by the ordering temperature $T_{\rm RKKY}$ as follows:

$$T_{\rm RKKY} \propto |J_{cf}|^2 D(E_{\rm F}), \tag{2.9}$$

where

$$J_{cf} \simeq \frac{{V_{cf}}^2}{E_{\rm F} - E_f}. \tag{2.10}$$

Actually the intensity of this interaction is also dominated by the de Gennes factor, and eq. (2.9) is given by the product with coefficient as $(g_J-1)^2J(J+1)$. This leads to the phase diagram for a Kondo lattice, originally derived by Doniach [2, 26] and emphasized by Brandt and Moshchalkov [27]. Figure 2.6 is well known as the Doniach phase diagram. If $|J_{cf}|D(E_{\rm F})$ is small, the compound becomes antiferromagnet with a large magnetic

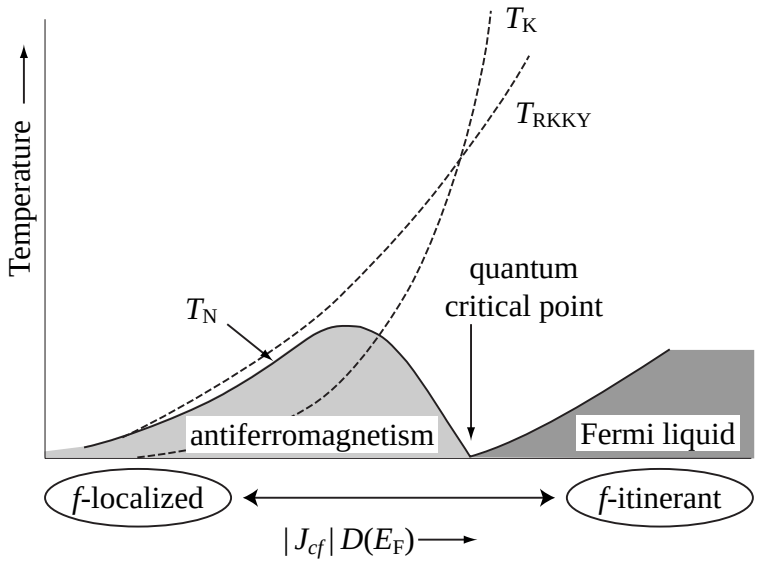

Fig. 2.6 Doniach phase diagram [27].

moment, while with increasing $|J_{cf}|D(E_{\rm F})$ both the magnetic moment and the ordering temperature tend to zero. The critical point where $T_{\rm N}$ becomes zero is called a "quantum critical point". Above the quantum critical point, Kondo-lattice paramagnets show up and consequently the f-atom valency becomes unstable, leading to the heavy fermion system.

The non-Fermi liquid behavior around the quantum critical point is also one of the recent topics in the f electron system. Here, the heavy fermion system is based on the Landau's Fermi liquid. Namely, the interacting electron system or the heavy electron system is related to the non-interacting one by the scaling law without a phase transition. The characteristic features are expressed as $\rho = \rho_0 + AT^2$, $C/T = \gamma$ and $\chi = \chi(0)$ at low temperatures. On the other hand, in the non-Fermi liquid system the following relations are characterized:

$$\rho \sim T^m \quad \text{with } m < 2, \tag{2.11}$$

$$C/T \sim -\log T. \tag{2.12}$$

Nearby the quantum critical point, Ce intermetallic compounds with an extraordinary wide variety of possible ground states are found. These include Kondo-lattice compounds

with magnetic ordering ($CeIn_3$, $CeAl_2$, CeB_6), small-moment antiferromagnets ($CePd_2Si_2$, $CeAl_3$), an anisotropic superconductor ($CeCu_2Si_2$), non-mangnetic Kondo-lattice compounds or the heavy fermion compounds ($CeCu_6$, $CeRu_2Si_2$) and valence fluctuation compounds (CeNi, $CeRh_2$, $CeRu_2$, $CeSn_3$).

We note the non-magnetic Ce compounds at low temperatures. In $CeCu_6$ and $CeRu_2Si_2$ with a small Kondo temperature, there exist no magnetic ordering but antiferromagnetic correlations between the Ce sites [28], showing the metamagnetic transition in the magnetic field: $H_c = 2$ T in $CeCu_6$ [29] and 8 T in $CeRu_2Si_2$ [30]. The results of dHvA experiments [31, 32, 19] and the band calculations [33] in $CeRu_2Si_2$ show that $4f$ electrons are itinerant. Namely the $4f$ electrons in Ce compounds such as $CeSn_3$ with a large Kondo temperature, which belong to the valence-fluctuation regime, are also itinerant in the ground state and contribute directly to the formation of the Fermi surface [34, 35].

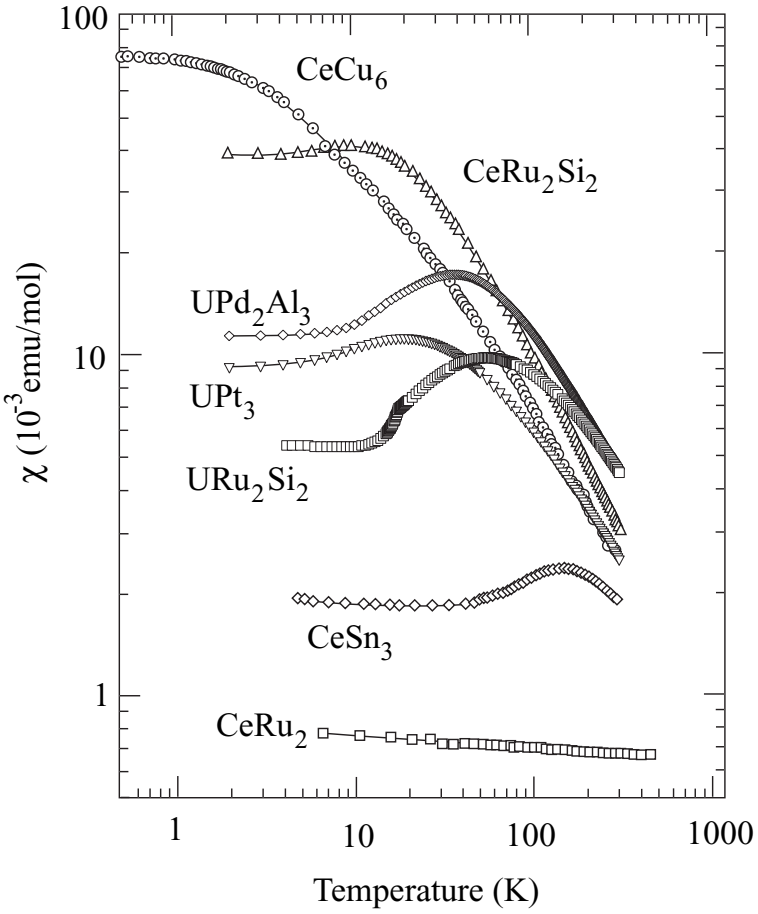

Fig. 2.7 Temperature dependence of the magnetic susceptibility for typical Ce compounds.

We will also pay attention to the non-magnetic Ce compounds to clarify the magnitude of Kondo temperature reflected in the magnetic susceptibility. Figure 2.7 shows the

temperature dependence of the magnetic susceptibility in some Ce compounds without magnetic ordering: $CeCu_6$ (T_K = 3–4 K), $CeRu_2Si_2$ (20 K), CeNi (150 K) and $CeSn_3$ (200 K). The magnetic susceptibility in these compounds follows the Curie-Weiss law at higher temperatures, possessing the magnetic moment near Ce^{3+} of $2.54\mu_B$, while it becomes approximately temperature-independent with decreasing the temperature, namely showing a broad maximum and then forming enhanced Pauli paramagnetism. The temperature indicating the peak of the susceptibility $T_{\chi max}$ almost corresponds to the characteristic temperature T_K. The valence of Ce atoms seems to be changed from Ce^{3+} into Ce^{4+} (non-magnetic state) with decreasing the temperature.

2.1.4 Pressure-induced superconductivity

Unconventional superconductivity has been an active area of research for several decades, ever since the discovery of the first heavy fermion superconductor, $CeCu_2Si_2$ [36]. Recently, some Ce-based heavy fermion compounds were found to exhibit superconducting under pressure, such as $CeIn_3$ and $CePd_2Si_2$ [3] as shown in Figs. 2.8 and 2.9. In these compounds, superconductivity appears around the quantum critical point (see Fig. 2.6). The similar pressure-induced superconductivity was also reported for the other Ce-based compounds such as $CeCu_2Ge_2$ [4], $CeRh_2Si_2$ [37, 38] and $CeRhIn_5$ [5]. In these superconductivity, the attractive force between quasiparticles are possible to be magnetically mediated, not to be phonon-mediated.

As mention above, pressure-induced superconductivity had been discovered in the antiferromagnetic Ce compounds. Surprisingly, Saxena *et al.* [6] found the pressure-induced superconductivity in a ferromagnet UGe_2. In this case, superconductivity appears inside the border of ferromagnetism.

2.1.5 Fermi surface study

Fermi surface studies are very important to know the ground-state properties of the rare earth compounds [8]. As mentioned in Sec. 2.1.3, the ground state of the Ce compounds is mainly determined by the competition between the RKKY interaction and the Kondo effect (see Fig. 2.6). When T_{RKKY} overcomes T_K, the ground state is the magnetic ordered one and the $4f$ electrons are regarded as localized. On the other hand, when T_K is dominant, the ground state is the non-magnetic one and the $4f$ electrons become itinerant.

In the $4f$-localized system, the Fermi surface is similar to that of corresponding La compound, but the presence of the $4f$ electrons alters the Fermi surface through the $4f$-electron contribution to the crystal potential and through the introduction of new Brillouin zone boundaries and magnetic energy gaps which occur when $4f$-electron moments order. The latter effect may be approximated by a band-folding procedure where the paramagnetic Fermi surface is folded into smaller Brillouin zone based on the magnetic unit cell, which is larger than the chemical one. If the magnetic energy gaps associated with the magnetic structure are small enough, conduction electrons undergoing cyclotron

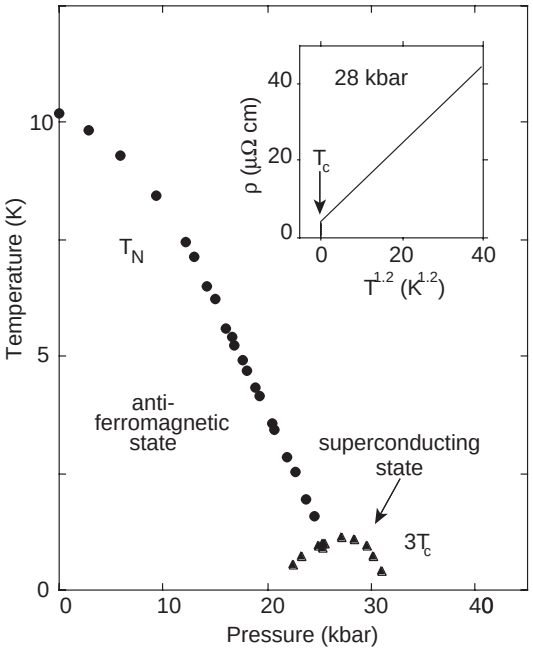

Fig. 2.8 Temperature-pressure phase diagram of $CePd_2Si_2$. Superconductivity appears below T_c in a narrow window where Néel temperature T_N tends to zero [3)].

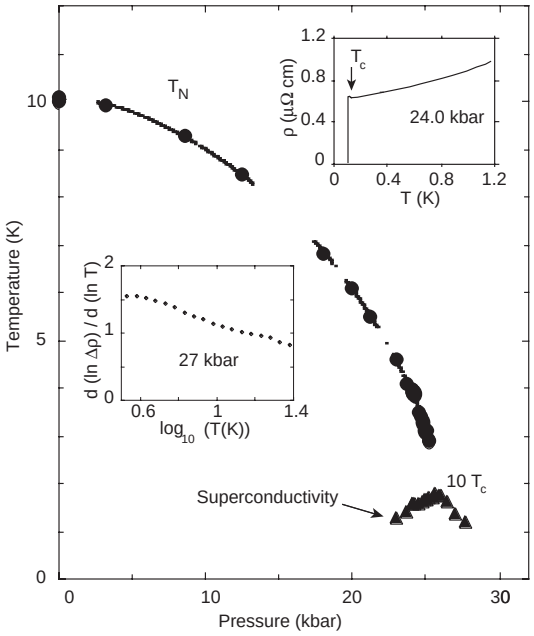

Fig. 2.9 Temperature-pressure phase diagram of $CeIn_3$. Superconductivity is observed in a narrow window near P_c, the pressure at which the Néel temperature T_N tends to zero. [3)].

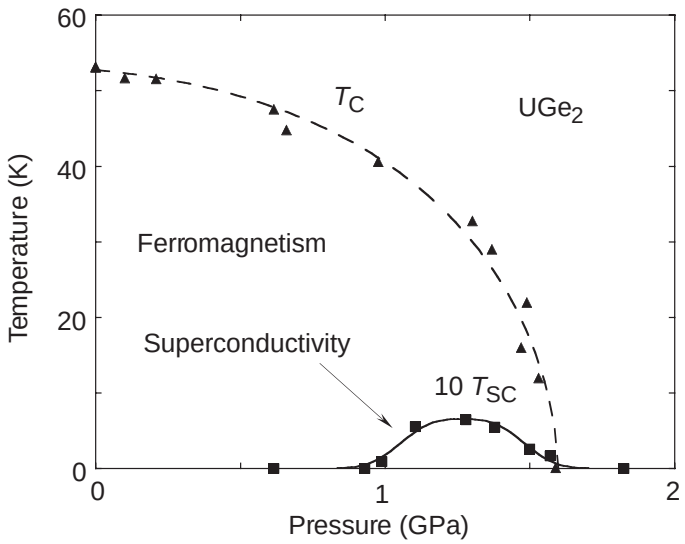

Fig. 2.10 Temperature-pressure phase diagram of UGe_2. T_c denotes the Curie temperature and T_{sc} the superconducting transition temperature [6)].

motion in the presence of magnetic field can tunnel through these gaps and circulate the orbit on the paramagnetic Fermi surface. If this magnetic breakthrough (breakdown) effect occurs, the paramagnetic Fermi surface may be observed in the dHvA effect even in the presence of magnetic order.

For cerium Kondo compounds with magnetic ordering such as CeB_6, the Kondo effect is expected to have minor influence on the topology of the Fermi surface, representing that the Fermi surfaces of the Ce compounds are roughly similar to those of the corresponding La compounds, but are altered by the magnetic Brillouin zone boundaries mentioned above. Nevertheless the effective masses of the conduction carriers are extremely large compared to those of La compounds. In this system a small amount of the $4f$ electron most likely contributes to make a sharp density of states at the Fermi energy. Thus the energy band becomes flat around the Fermi energy, which brings about the large mass.

In some Ce compounds such as $CeCu_6$, $CeRu_2Si_2$, CeNi and $CeSn_3$, the magnetic susceptibility follows the Curie-Weiss law with a moment of Ce^{3+}, $2.54\mu_B$/Ce, has a maximum at a characteristic temperature $T_{\chi\max}$, and becomes constant at lower temperatures (see Fig. 2.7). This characteristic temperature $T_{\chi\max}$ corresponds to the Kondo temperature T_K, as mentioned in Sec. 2.1.3. A characteristic peak in the susceptibility is a crossover from the localized-$4f$ electron to the itinerant one. The Fermi surface is thus highly different from that of the corresponding La compound. The cyclotron mass is also extremely large, reflecting a large γ-value of $\gamma \simeq 10^4/T_K$ (mJ/K^2·mol).

2.1.6 General property of uranium compounds

The $5f$ electron system, including U compounds, are particularly interesting in the sense that they bridge the gap between the $3d$ and the $4f$ electron systems. The $5f$ electrons in the U atom have a character between the $3d$ and $4f$ electrons, located slightly inside the closed $6s$ and $6p$ shells. Therefore, they may possess both band-like and atomic-like characters, even in the crystal. The properties of some U compounds thus have been understood on the basis of the $5f$ band model, similar to the $3d$ transition metals and their intermetallic compounds. The dHvA effect was measured in some of these U compounds. The fully-relativistic spin-polarized $5f$-itinerant band model can explain the observed dHvA results very well. Namely, the $5f$ electrons in the magnetically ordered uranium compounds are itinerant and also contribute to the magnetic moment at the uranium site.

The discovery of heavy fermions in rare earth compounds encouraged the research heavy fermion systems are found in the U compounds too. In particular, UPt_3, UBe_{13}, URu_2Si_2, UPd_2Al_3 and UNi_2Al_3 show unconventional superconductivity with magnetic ordering. Coexitence of superconductivity and magnetism accelerated, furthermore, the study of heavy fermions in the U compounds, and thus Fermi surface studies are interesting and very important. Such studies have actually been done in some of these meterials and they offer interesting information. We summarize the characteristic features in the U compounds, which are compared to those in the Pr compounds with the $4f^2$ configuration: (1) The magnetic ordering temperature is in a wide temperature range from close

to 0 to 300 K, which is compared to 0-20 K in the Pr compounds. (2) The magnetic moment is also in a wide range from close to 0 (0.02 μ_B/U) to 3 μ_B/U, which is compared to about 1 - 2 μ_B/Pr.

2.2 Review of Ce compounds

2.2.1 $CeNiGe_3$

Two crystal structures had been proposed for $CeNiGe_3$: the cubic $Yb_3Rh_4Sn_{13}$-type structure [39] and the orthorhombic $SmNiGe_3$-type structure [40]. Antiferromagnetism below $T_N = 4.2$ K was anticipated from the electrical resistivity data and the crystal structure was analysed as the cubic one [39]. On the other hand, in the orthorhombic derivative antiferromagnetic ordering was reported to set in at $T_N = 7.6$ K from the magnetic susceptibility [41]. Finally, Durivault *et al.* revealed that $CeNiGe_3$ has the orthorhombic $SmNiGe_3$-type structure (space group: Cmmm) from the neutron diffraction experiment [42]. The thermal dependence of magnetization data shows a maximum at 5.5 K, indicating an antiferromagnetic order at T_N=5.5 K. This value is different from the previus ordering temperatures. They clarified from the neutron diffraction data two propergation vectors; $\boldsymbol{k}_1 = (1\ 0\ 0)$ and $\boldsymbol{k}_2 = (0\ 0.409\ 1/2)$. The two propagation vectors showed distinct ordering temperatures, $T_{N1} = 5.9$ K and $T_{N2} = 5.0$ K, respectively, as shown in Fig. 2.12. The $\boldsymbol{k}_1$ is associated with a commensurate collinear antiferromagnetic structure. As shown in Fig. 2.13 (a), this magnetic sturacture is described by ferromagnetic trigonal prisms, an antiferromagnetic arrangement. On the other hand, the incommensurate $\boldsymbol{k}_2$ indicates the helicoidal structure in the *ab*-plane.

Figures 2.14 and 2.15 shows the temperature dependence of electrical resistivity in $CeNiGe_3$ [43, 44]. The antiferromagnetic ordering shows a sudden drop in ρ below $T_N = 5.5$ K. In the paramagnetic region the $\rho(T)$ curve reveals characteristic features of interplay of Kondo and crystal-field interactions. A pronounced rise of the resistivity from 10 K to 100 K is followed by a weak nearly linear increase of the resistivity at higher temperatures.

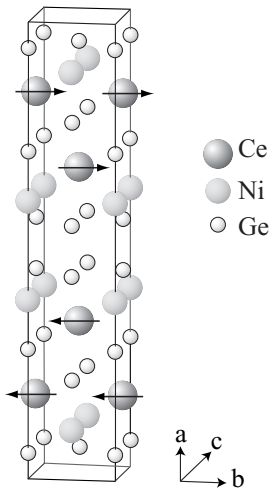

Fig. 2.11 Crystal structure of $CeNiGe_3$. Arrows indicate the magnetic moments correponding the propagation vector $\boldsymbol{k}_1 = (1\ 0\ 0)$.

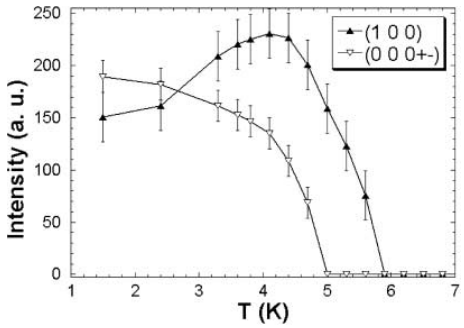

Fig. 2.12 Temperature dependence of the intensity of two magnetic reflections in $CeNiGe_3$ [42].

2.2.2 $CeNi_2Al_5$

$CeNi_2Al_5$ has the body-centerd orthorhombic $PrNi_2Al_5$-type structure (space group: Immm), as shown in Fig. 2.16 [45, 46].

The temperature dependence of the resistivity shows both the -log T dependence from 4 K to 30 K and a broad maximum reflecting the formation of the Kondo lattice around 4 K(see Fig. 2.17). The abrupt drop of the resistivity(Fig. 2.17), the magnetic susceptibility(Fig. 2.18) and the specific heat(Fig. 2.19) exibit an antiferromagnetic ordering below $T_N = 2.6$ K.

Figures 2.18 and 2.20 show the temperature dependence of magnetic susceptibilities and reciprocal susceptibilities in $CeNi_2Al_5$ [47]. The observed large magnetic anisotropy indicates the strong CEF effect, reflecting the orthorhombic structure. The magnetization curve also shows the magnetic anisotropy, as shown in Fig. 2.21. The fitting CEF parameters lead to splittings around 200 K for the first excited state and around 600 K for the total splitting [47, 48].

The magnetic structure below T_N is the modulated structure with a complex propagation vector $\boldsymbol{k} = (0.500,\ 0.405,\ 0.083)$ [47, 49, 48]. Neutron scattering experiments [50] has determined the direction of actual magnetic moment, which is somewhat tilted towards the a-axis. The modulated structure has been kept down to 400 mK, as shown in Figs. 2.22 and 2.23.

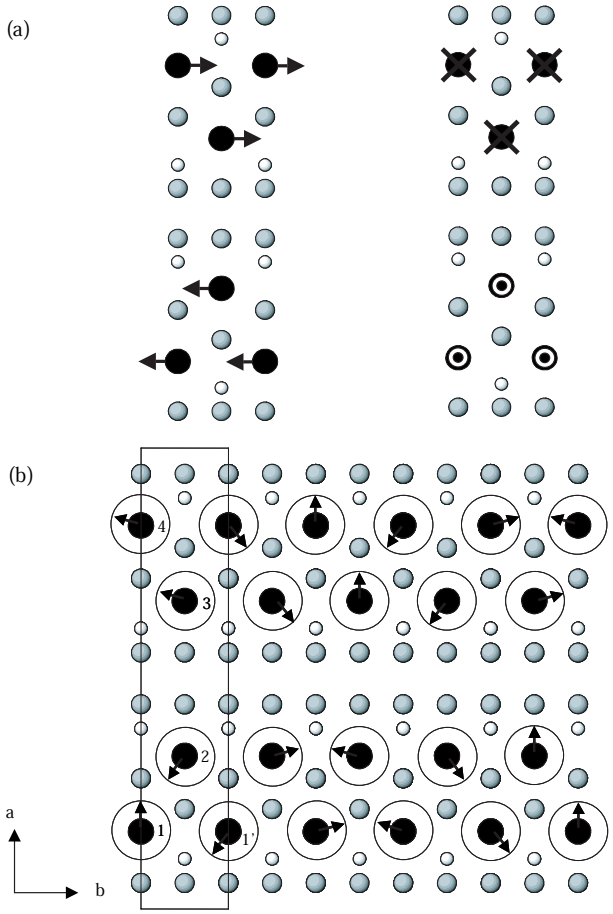

Fig. 2.13 Projection onto the (001)-plane of the magnetic structures of a $CeNiGe_3$. Ce, Ge and Ni: large black, medium grey and small white circles respectively. (a) commensurate part (two possibilities). (b) incommensurate helicoidal part [42].

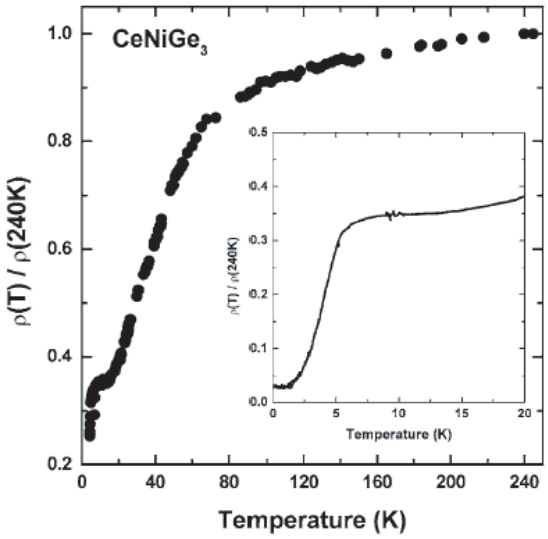

Fig. 2.14 Temperature dependence of the reduced electrical resistivity of $CeNiGe_3$ (inset for $\leq 20K$) [42].

2.2.3 $CeAgSb_2$

$CeAgSb_2$ or more generally RTX_2(R:rare earth, T:transition metal) and UTX_2, as discussed by Kaczorowski *et al.* [52], crystallize in the tetragonal structure (space group P4/nmm) [53, 54], which can be described as a filled UX_2 in UTX_2: planes of transition metal atoms intercalate into the unit cell of the respective binary uranium dipnictide. The crystal structure of $CeAgSb_2$ can also be understood from the stacking arrangement of CeSb-Ag-CeSb-Sb layers [53].

The neutron scattering experiment on a polycrystal of $CeAgSb_2$ done by André *et al.*[55] indicated that the magnetic moment is simply oriented along the [001] direction (c-axis), with a Curie temperature $T_c = 9.6\,\mathrm{K}$ and a magnetic moment μ_s =0.33 μ_B/Ce. However, the magnetization curve is quite anomalous [54], as shown in Fig. 2.25. The magnetization for the field along [001] indicates a typical ferromagnetic magnetization curve with μ_s =0.37 μ_B/Ce, while the magnetization for the field perpendicular to [001] increases almost linearly up to 30 kOe and saturates at higher fields, reaching 1.1 μ_B/Ce. This corresponds to a metamagnetic transition in an antiferromagnet. These magnetization curves cannot be understood from the simple ferromagnetic structure proposed by the neutron scattering experiment.

This compound is also interesting with respect to a quasi-two dimensionality. The dHvA experiments on $CeAgSb_2$ as well as on reference compounds $YAgSb_2$ and $LaAgSb_2$ were reported by Myers *et al.* [56]. A small Fermi surface was observed for $CeAgSb_2$. On the other hand, the Fermi surface in $YAgSb_2$ and $LaAgSb_2$ was found to consist of a cylindrical Fermi surface and two or three kinds of closed (ellipsoidal) ones. The reason why main Fermi surfaces were not observed in $CeAgSb_2$ was mainly due to the fact that

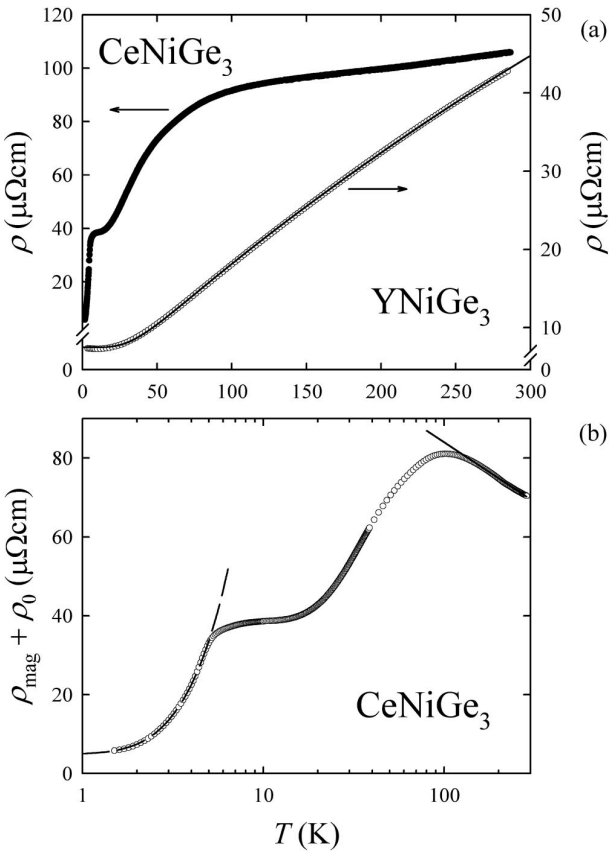

Fig. 2.15 (a)Temperature dependence of electrical resistivity of $CeNiGe_3$ and a non-4f reference compound $YNiGe_3$, and (b)the magnetic resistivity of $CeNiGe_3$ [44].

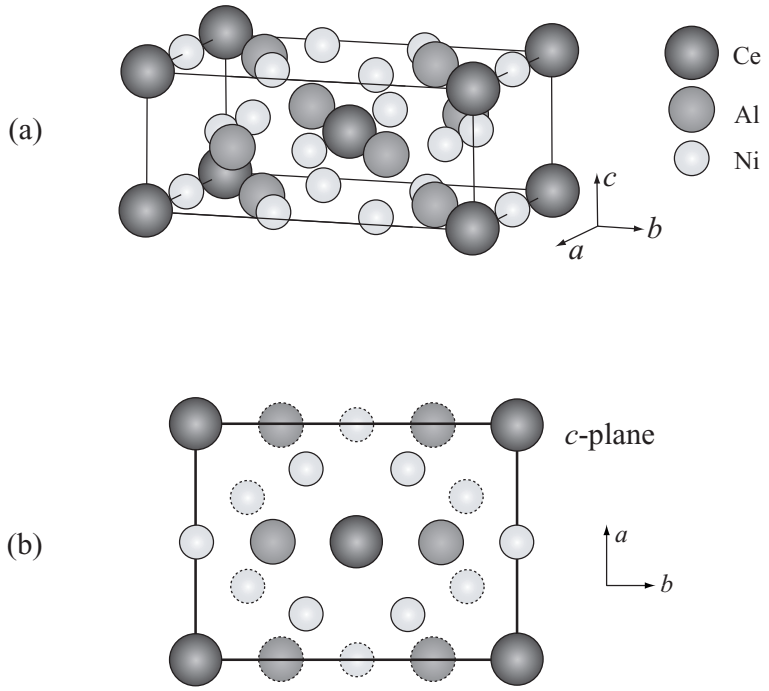

Fig. 2.16 (a)Crystal structure of $CeNi_2Al_5$. (b)Crystal structure from view of c-axis. Circles shown by dashed lines denote the atoms on the plane at $z = 1/2$.

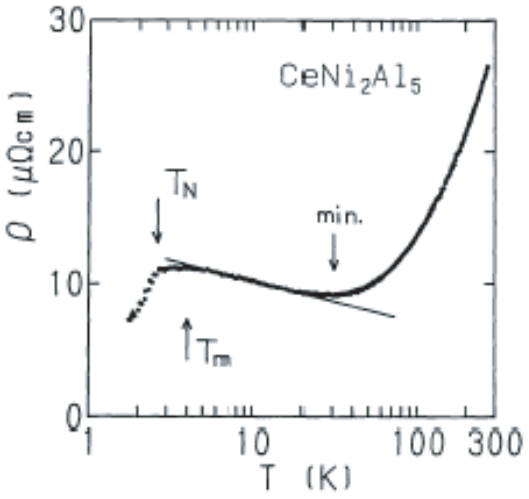

Fig. 2.17 Temperature dependence of electrical resistivity of $CeNi_2Al_5$ [51].

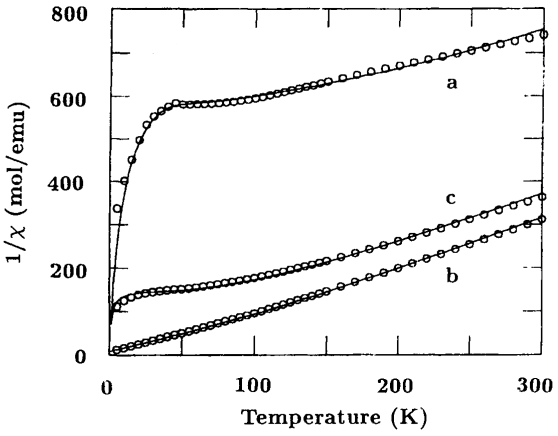

Fig. 2.18 Temperature dependence of reciprocal magnetic susceptibility of $CeNi_2Al_5$ [47].

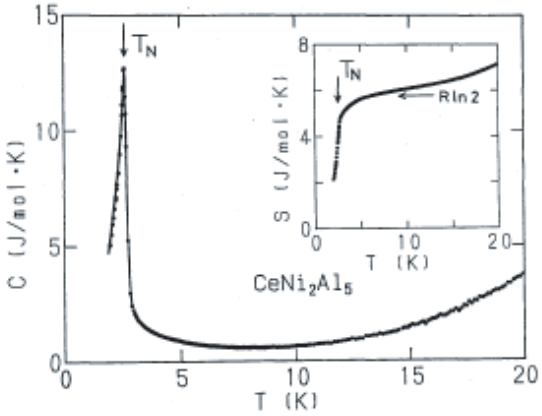

Fig. 2.19 Temperature dependence of specific heat and entropy (inset) of $CeNi_2Al_5$ [51].

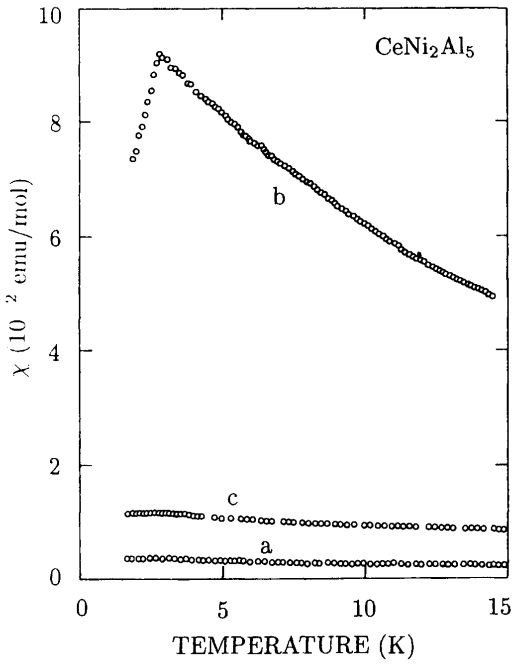

Fig. 2.20 Temperature dependence of magnetic susceptibility of $CeNi_2Al_5$ [47].

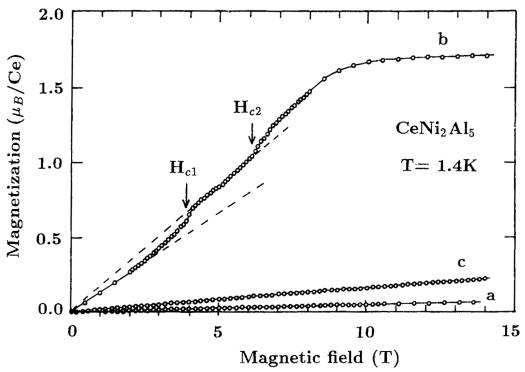

Fig. 2.21 Magnetization curves of $CeNi_2Al_5$ at 1.4 K [47].

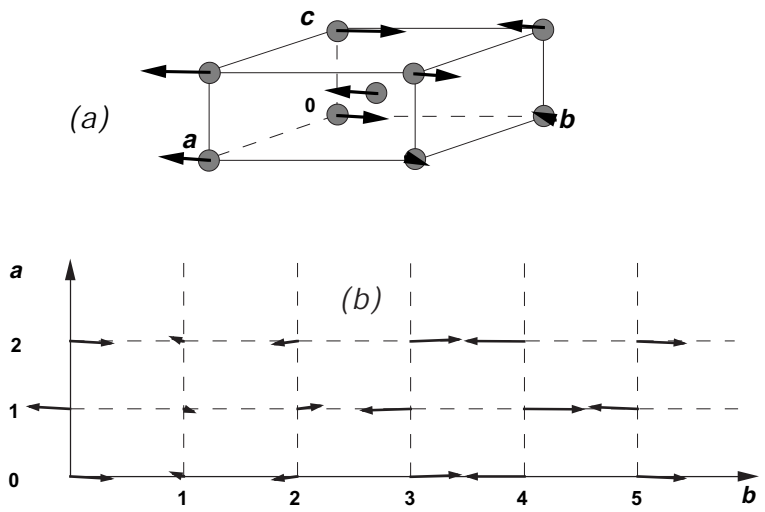

Fig. 2.22 Magnetic structure of $CeNi_2Al_5$ [50]. (a)The crystallographic unit cell and (b)propagation in the ***ab***-plane.

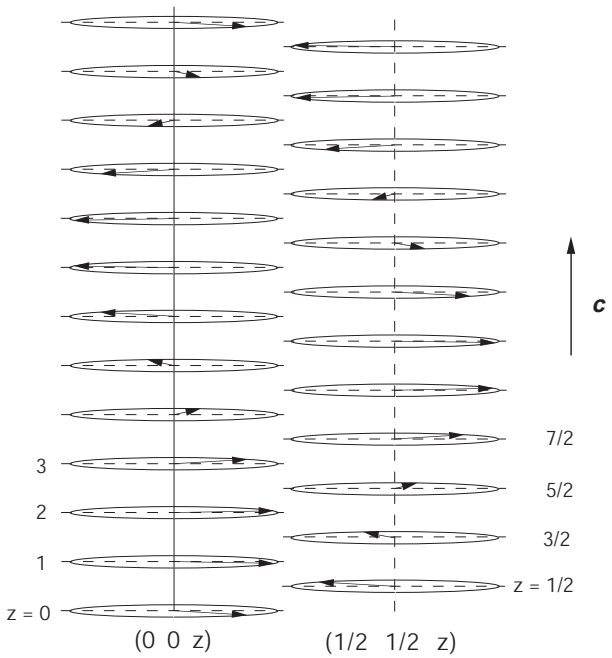

Fig. 2.23 Propagation along the ***c***-direction [50].

the measurement was carried out at a high temperature of 2.1 K and the specific heat coefficient γ is reported to be 75 mJ/K^2·mol for the polycrystalline sample of $CeAgSb_2$ [57], which is larger than that of $LaAgSb_2$ ($\gamma = 2.62$ mJ/K^2·mol) [58].

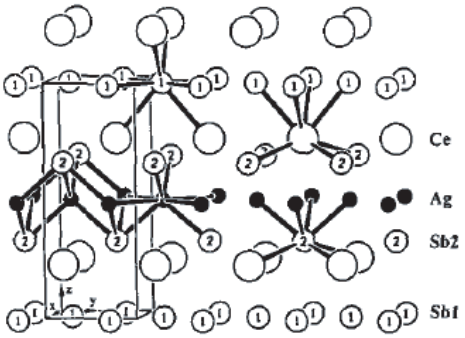

Fig. 2.24 Crystal structure of $CeAgSb_2$ [53].

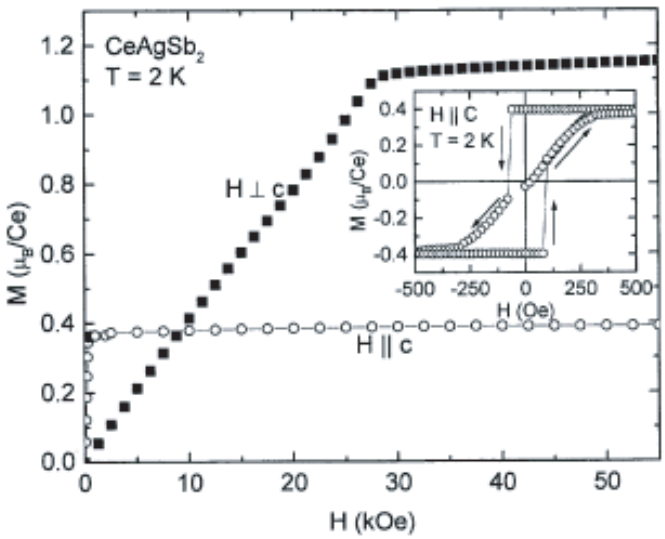

Fig. 2.25 Magnetization curve of $CeAgSb_2$ [54].

2.3 Review of U compounds

2.3.1 $UTGa_5$(T:Ni, Pd, Pt)

$UTGa_5$ (T:Ni, Pd, Pt) has the $HoCoGa_5$-type tetragonal structure with space group P4/mmm as shown in Fig. 2.26. This crystal structure shows a clear two-dimensional nature. One unit of a uniaxially distorted UGa_3 layer with the $AuCu_3$-type structure and a transition metal layer stack sequentially along the [001] direction. $UTGa_5$ (T: Ni, Pd, Pt) orders antiferromagnetically, while the other compounds $UTGa_5$ (T:Fe, Co) exhibit Pauli-paramagnetic behavior. $UNiGa_5$, $UPdGa_5$ and $UPtGa_5$ were reported to have an antiferromagnetic ordering at 86 K, 30 K and 26 K, respectively. Above the Néel temperature, the temperature dependence of the magnetic susceptibility is very weak. This weak temperature dependence in susceptibility is very similar to that of UGa_3, which is a typical $5f$-itinerant antiferromagnet based on the U-$5f$ band.

From the neutron diffraction study, their magnetic structures have revealed [59]. $UNiGa_5$ has the Néel-type magnetic structure with a magnetic moment of 0.9 μ_B/U, while $UPtGa_5$ has an antiferromagnetic sequence along the [001] direction, with a magnetic moment of 0.24 μ_B/U as shown in Fig. 2.27.

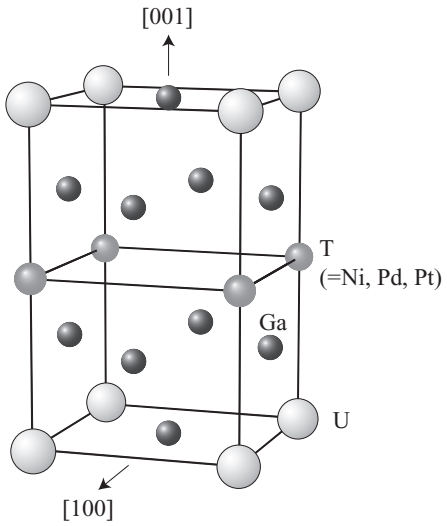

Fig. 2.26 Crystal structure of $UTGa_5$(T=Ni, Pt, Pd).

In $UNiGa_5$, the Néel temperature T_N = 85.5 K is relatively high. The electronic specific heat coefficient γ is 50 mJ/K^2·mol.

$UPdGa_5$ orders antiferromagnetically below T_N = 30 K. The electronic specific heat coefficient γ is reported as 40 mJ/K^{2}mol. The magnetic struture is the same as that of $UPtGa_5$, as shown next. The magnetic moment is 0.33 μ_B/U [60].

$UPtGa_5$ with the tetragonal structure orders antiferromagnetically below T_N = 26 K. From neutron diffraction experiments, magnetic moments of uranium ions are found to

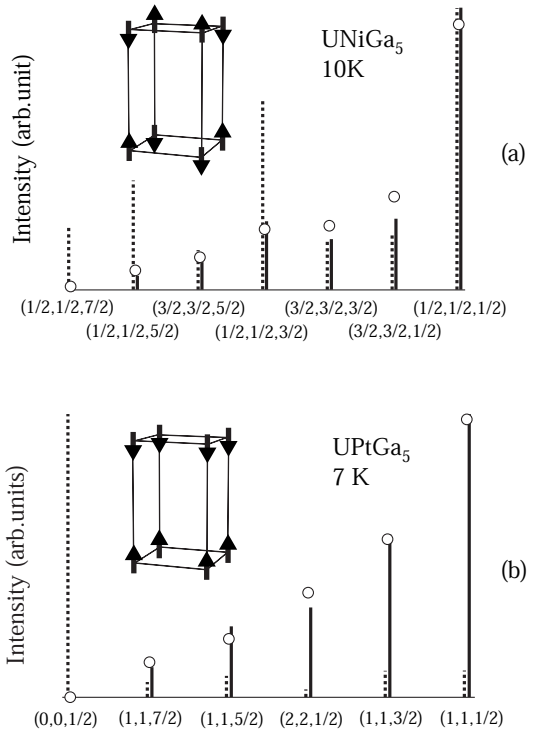

Fig. 2.27 Magnetic structures of $UTGa_5$(T=Ni, Pt) [59].

be aligned ferromagnetically in the (001) plane, directed along the [001] direction [59]. An ordered moment is 0.24 μ_B/U and the electronic specific heat coefficient γ is reported as 57 mJ/K^{2}mol. Tokiwa *et al.* discussed about the magnetic structure in $UNiGa_5$ and $UPtGa_5$ from a viewpoint that the orbital contribution of $5f$ electrons would be essentioally important in the magnetic structure [59].

From dHvA experiments, the Fermi surface of $UNiGa_5$ is found to consists of one cylindrical Fermi surfaces and two ellipsoidal Fermi surfaces, as shown in Figs. 2.28 and 2.29 [61]. $UPtGa_5$ consists of four kinds of cylindrical Fermi surfaces, as shown in Figs. 2.30 and 2.31 [62]. Namely, the topology of the Fermi surface are found to be quasi-two dimensional in $UNiGa_5$ and $UPtGa_5$, reflecting the tetragonal structure.

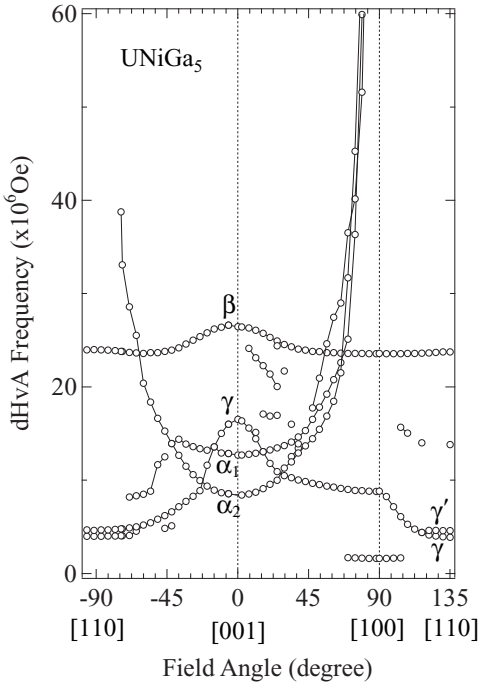

Fig. 2.28 Angular dependence of the dHvA frequencies in $UNiGa_5$ [61].

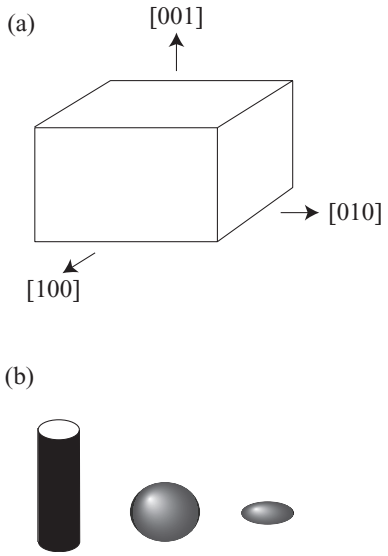

Fig. 2.29 (a) Brillouin zone and (b) simplified Fermi surfaces of $UNiGa_5$ [61].

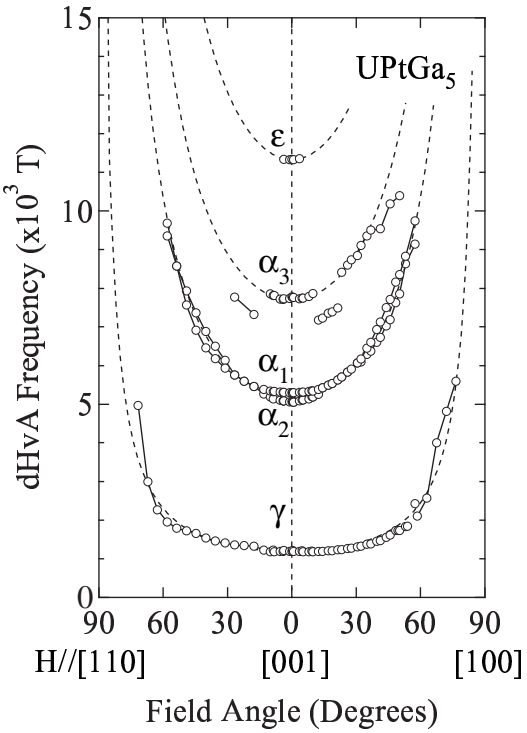

Fig. 2.30 Angular dependence of the dHvA frequencies in $UPtGa_5$ [63].

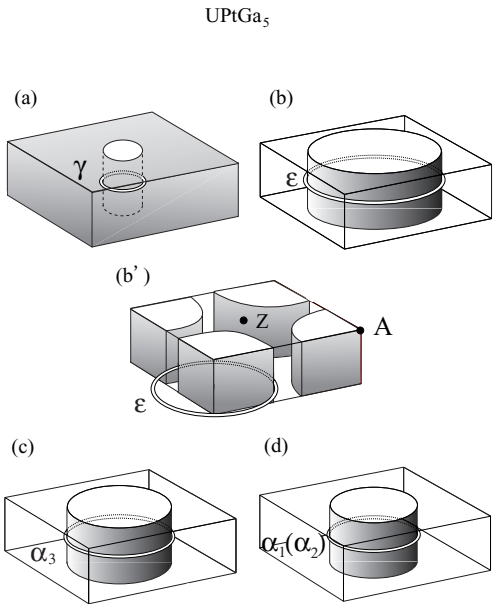

Fig. 2.31 Fermi surfaces for branches (a) γ,(b) ϵ, (c) α_3, (d) $\alpha_1(\alpha_2)$ in $UPtGa_5$ [63].

2.3.2 UN

UN with the cubic NaCl-type structure orders antiferromagnetically below $T_N = 53$ K [64]. Its antiferromagnetic structure [64] is the type-I structure as shown in Fig. 2.32. The orderd moment and effective moment is 0.75 μ_B/U [64] and 3.1 μ_B/U, respectively. Its U-U distance is the smallest in uranium pnictides and is in the critical region for an appearence of magnetism on a Hill plot. UN is thus considerd to be situated in an crossover between a itinarant and localized electron magnetism. Figure 2.33 shows a temperature dependence of electrical resistivity [65]. There is a hump at 52 K coresponding to T_N.

The susceptibility and neutron diffraction of UN under pressure were measured by Fournier *et al* [66, 67]. As shown in Fig. 2.34, T_N decreases with increasing pressure. Moreover, an ordered moment μ_s and the Néel temperature T_N decrease similarly as a function of pressure, as shown in Fig. 2.35. From this experimental result, they concluded that UN is a band antiferromagnet.

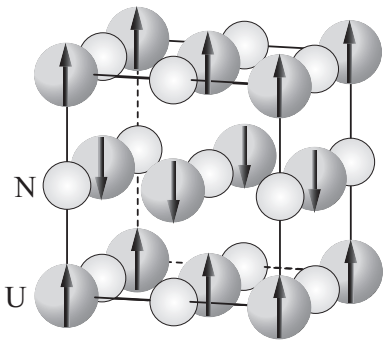

Fig. 2.32 Magnetic structure of UN.

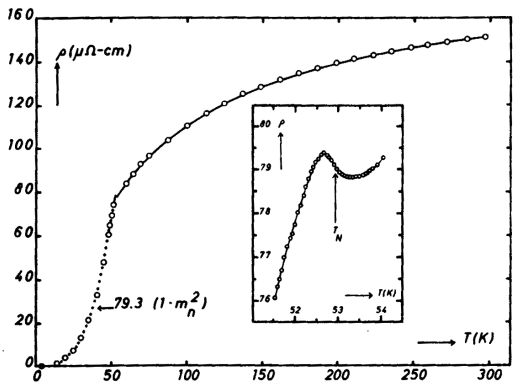

Fig. 2.33 Temperature dependence of electrical resistivity in UN [65].

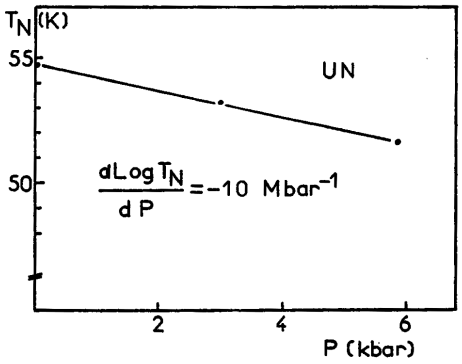

Fig. 2.34 Pressure dependence of T_N in UN [66].

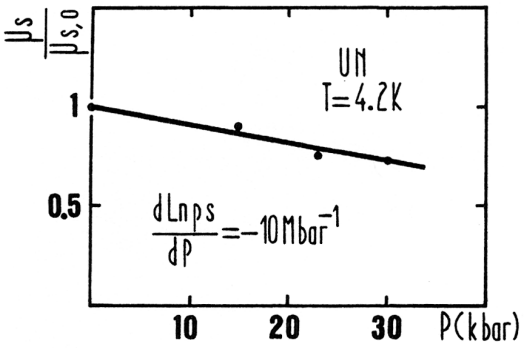

Fig. 2.35 Pressure dependence of the ordered moment in UN [67].

2.3.3 UGa_3

UGa_3 was once studied from a viewpoint of the $5f$-itinerant antiferromagnetism [68, 69, 70, 71]. Its Néel temperature $T_N = 67$K is relatively high. Characteristic properties are a small ordered moment of 0.75 or 0.95 μ_s/U and a relatively large electronic specific heat coefficient $\gamma = 50\text{mJ/K}^2\cdot\text{mol}$. Furthermore, the magnetic susceptibility in the paramagnetic region does not follow the Curie-Weiss law, being dominated by a Pauli-like contribution. From the magnetoresistance experiment, UGa_3 is found to be a compensated metal with equal carrier numbers of electrons and holes. The carriers with relatively larger cyclotron masses of 2.3 - 9.4 m_0 are detected in the recent dHvA experiment [72].

2.3.4 URu_2Si_2

The heavy-fermion compound URu_2Si_2 exhibits two successive transitions at $T_c = 1.4$ and $T_0 = 17.5$ K. The former is the superconducting transition temperature. On the other hand, the latter has still remained unidentified, although several characteristic features are associated with this phase transition. The energy gap was found to open over part of the Fermi surface, which is reflected by a term of $\exp(-\Delta/k_BT)$ for the specific heat, electrical resistively and nuclear spin-lattice relaxation rate below T_0. The neutron diffraction study also indicated the development of a simple type-I antiferromagnetic order with a tiny $5f$-magnetic moment of 0.03 μ_B along the tetragonal [001] direction below T_0 [73], as shown in Fig. 2.36. This tiny moment is compared to the effective magnetic moment $\mu_{\text{eff}} =$

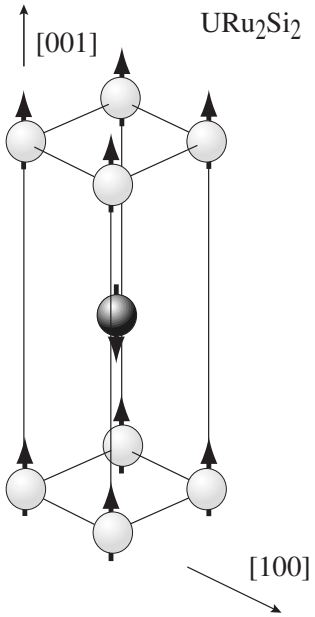

Fig. 2.36 Antiferromagnetic structure in URu_2Si_2.

3.51 μ_B /U obtained from the magnetic susceptibility data above 150 K, which is close to the $5f$-localized one: 3.58 μ_B/U for $5f^2(U^{4+})$ or 3.62 μ_B/U for $5f^3(U^{3+})$.

From the dHvA effect of URu_2Si_2, Ohkuni *et al.* studied the Fermi surface property [74]. Figures 2.37 and 2.38 show the experimental and theoritical angular dependence of the dHvA frequency, respectively. The theoritical data are based on the Fermi surfaces in Figs. 2.39 and 2.40. The dHvA branches named α, β and γ most likely correspond to bands 17-hole, 19-electron centered at X and 20-electron, respectively.

One of the characteristic phenomena in URu_2Si_2 is a metamagnetic transition, as shown in Fig.**??**. The sharp metamagnetic transition with three-steps is observed[75].

Recent neutron scattering and NMR experiments under pressure shed a new insight to this phase transition. It was clarified from the neutron scattering experiment that the magnetic moment increases linearly as a function of pressure, saturates in the pressure region from 1.0 to 1.5 GPa, with a moment of $0.25\mu_B$, and jumps to $0.4\mu_B$, indicating a sharp phase transition at $P_c = 1.5$ GPa [76], as shown in Fig. 2.42. Furthermore, the result of NMR experiment indicated that there exist distinct antiferromagnetic and paramagnetic regions, and with increasing pressure the antiferromagnetic region increases in space, reaching 100% of the antiferromagnetic volume fraction at 1.0 GPa [77], as shown in Fig. 2.43.

In the thermal expansion experiment under pressure, an additional anomaly is observed below T_0 [78]. They plotted this anomaly in the temperatuer-pressure phase diagram, as shown in Fig. 2.44.

Very recently Chandra *et al.* represented a new theoretical model for the unknown order parameter to explain the pressure-induced antiferromagnetism. They proposed incommensurate orbital antiferromagnetism associated with circulating currents between the uranium ions [79, 80].

2.3.5 UPt_3

Figure 2.41 also shows the metamagnetic transition in UPt_3. UPt_3 is the most intensively studied heavy fermion superconductor. Superconductivity coexists with antiferromagnetic ordering, as shown in Fig. 2.45. This ordering, which occurs below $T_N = 5$ K, plays an important role in breaking the degeneracy of the multiple superconducting phases, which results in the existence of three well-known phases called A, B and C. It has recently been reported that UPt_3 is of odd-parity symmetry as determined by an NMR-Knight shift experiment [83, 84]. This antiferromagnetic ordering is, however, quite unusual. The staggered moment in Fig. 2.45, which is oriented along the $[\bar{1}100]$ or $[1\bar{1}00]$ direction in the hexagonal structure, is extremely small, 0.02 μ_B/U [85], although the effective moment in the Curie-Weiss law is 3.0 μ_B/U at high temperatures [86]. The magnetic Bragg peak intensity increases almost linearly when the temperature decreases below 5 K, and the magnetic correlation length remains finite down to 100 mK; it is in the range 300-700 Å [87]. On the other hand, no trace of magnetic ordering has been reported by slow and/or thermodynamic probes such as the magnetic susceptibility, specific heat and NMR experiments. These results indicate that the antiferromagnetic ordering in UPt_3 is

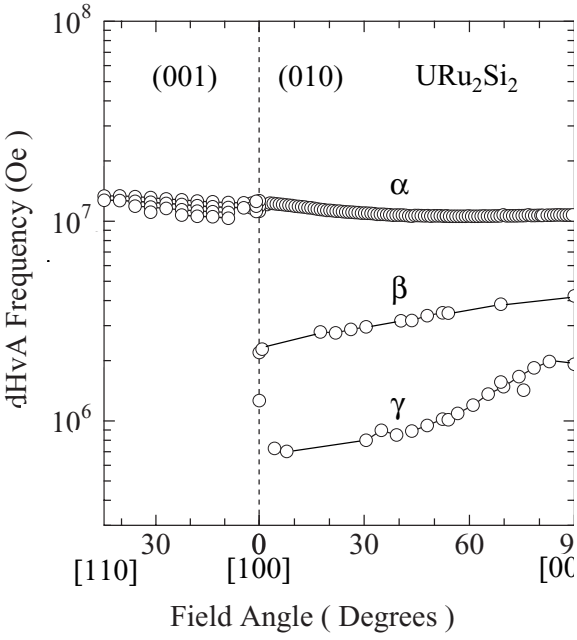

Fig. 2.37 Angular dependence of the dHvA frequency in URu_2Si_2 [74].

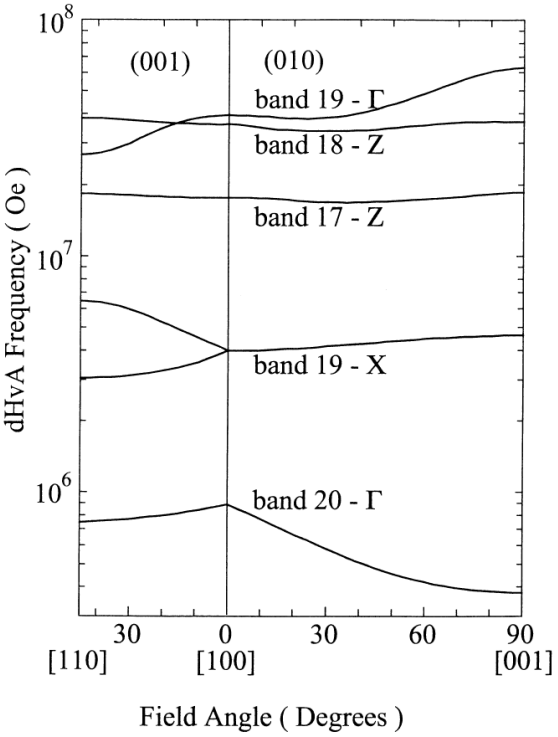

Fig. 2.38 Angular dependence of the theoritical dHvA frequency in the paramagnetci state of URu_2Si_2 [74].

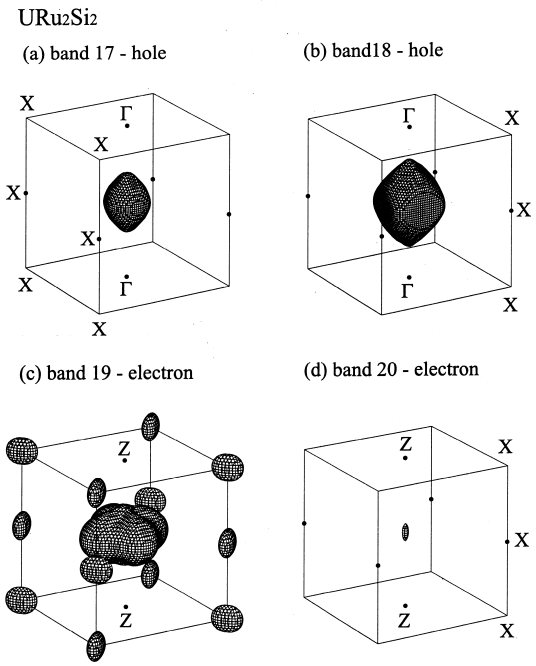

Fig. 2.39 Fermi surfaces in the paramagnetic state of URu_2Si_2 [74].

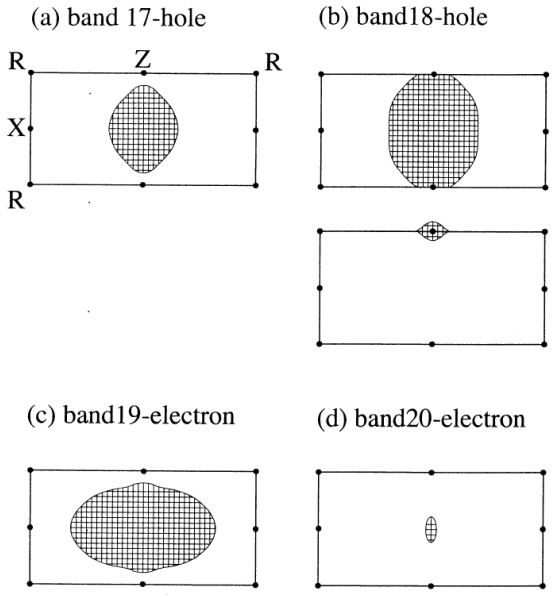

Fig. 2.40 Coss-section of the paramagnetic Fermi surface in the antiferromagnetic Brillouin zone in URu_2Si_2 [74].

not static but dynamic.

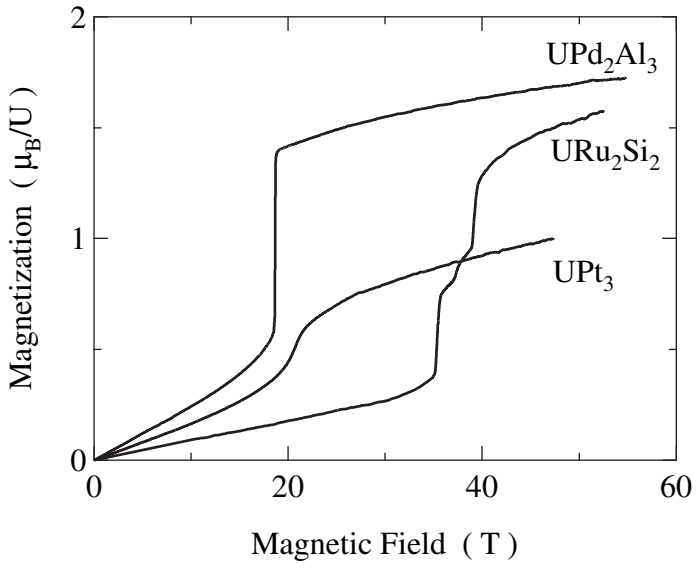

Fig. 2.41 Magnetization curves at 1.3 K for UPd_2Al_3, URu_2Si_2 and UPt_3. Magnetic fields are applied along $[11\bar{2}0]$, [001] and $[11\bar{2}0]$, respectively.

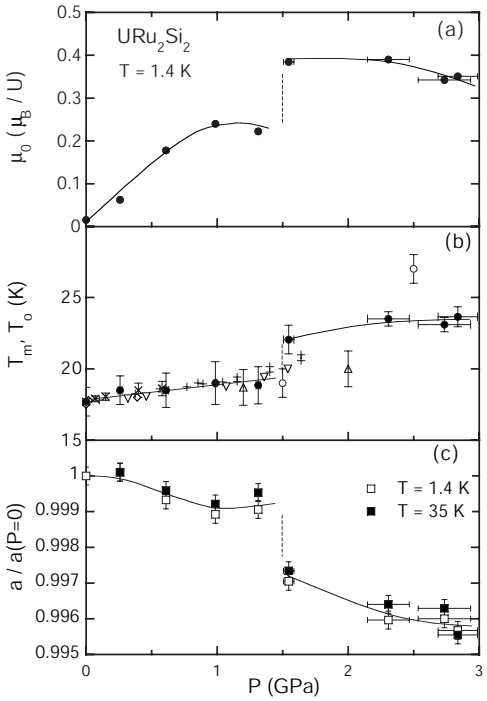

Fig. 2.42 Pressure dependence of (a) the magnetci moment, (b) characteristic transition temperature and (c) lattice constant in URu_2Si_2 [76].

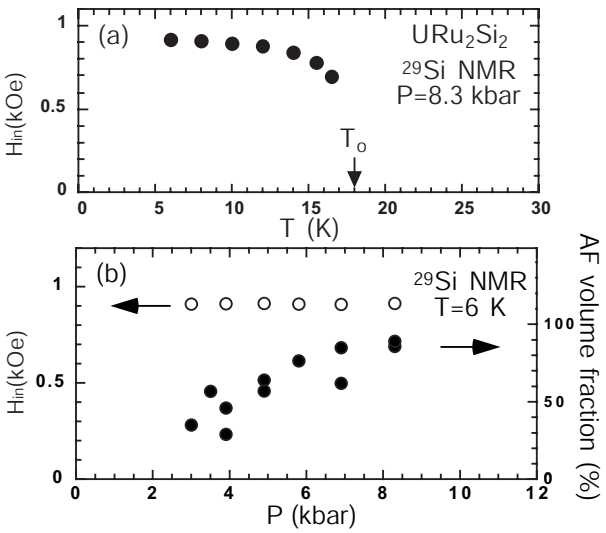

Fig. 2.43 (a) Tempearure dependence of $H_{\rm in}$, and (b) pressure dependence of $H_{\rm in}$ the antiferromagnetic region for URu_2Si_2. [81]

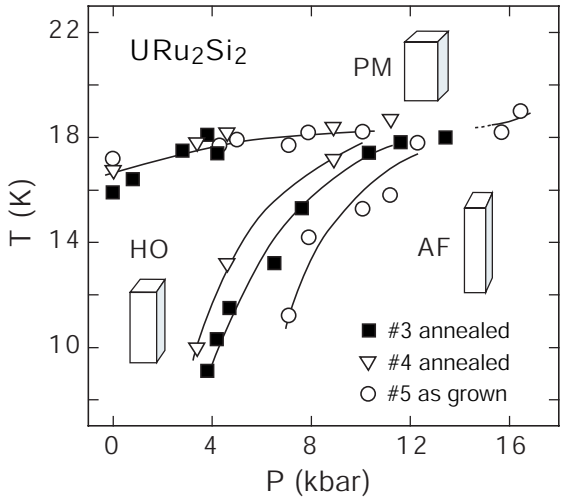

Fig. 2.44 T-P phase diagram from the thermal expansion measurements under pressure [82]. PM, HO, and AF indicate the paramagnetic, hidden order, and antiferromagnetic order phases, respectively.

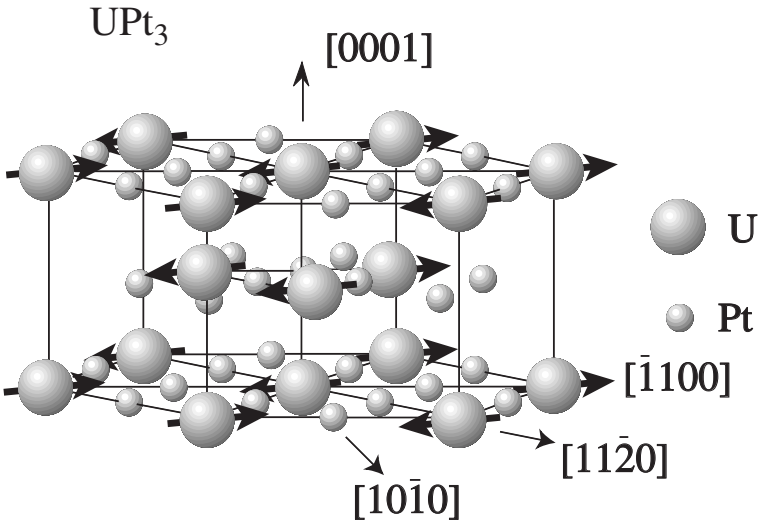

Fig. 2.45 Antiferromagnetic structure at zero field for UPt_3.

3 Experimental

3.1 Pressure

3.1.1 High-pressure technique

(a) Piston cyllinder cell

The electrical resistivity and the dHvA experiments under pressure were performed with a conventional Be-Cu, piston-cylinder clamping type pressure cell as shown in Fig. 3.1. Most part of the pressure cell is made of Be-Cu and piston is made of tungsten carbide (WC). Electrical leads were introduced into the sample region through a hole (0.6 mmϕ) of an obturator. Then, the hole was sealed by Stycast 2850FT epoxy. The anti-extrusion ring are used to prevent extrusion of Teflon into the clearance between piston or obturator, and cylinder under pressure.

We used a 1:1 mixture of Daphne7373 and kerosine as a pressure transmitting medium.

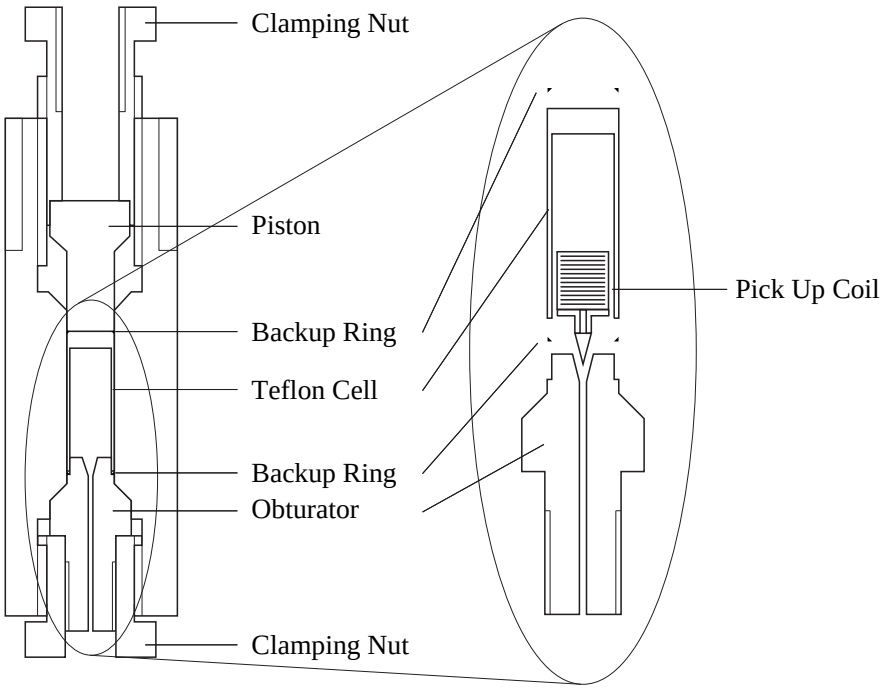

Fig. 3.1 Cross-sectional view of the pressure cell.

(b) Cubic anvil cell

As mentioned above, the piston cylinder cell is a usefull method up to around 2-3 GPa. To obtain higer pressure, we used a cubic-anvil device which has been developed by Môri *et al.* for precise electrical measurements at low temperatures in Institute for Solid State Physics, University of Tokyo (ISSP). The cubic anvils made of tungsten carbides having 4 mm on edge of square face press the sample from 6 directions as shown in Fig. 3.2. In Fig. 3.3 is shown the internal configuration of a gasket with a teflon cell in which the sample is immersed in fluid. The electrical resistivity of sample was measured by means of a four-terminal method. As electrical leads, gold wires of 20 micron in diam. were used with silver paint contact on the surface of the specimen and connected to thin gold ribbons attached to back up blocks, as shown in Fig. 3.3. As a pressure transmitting fluid, we used a mixture of fluorinert No. FC70 and No. FC77.

The cubic anvil dies were placed between the end of a pair of pressure transmitting columns consisting of fiber-reinforced plastic (FRP) disks as shown in Fig. 3.4. The whole specimen is cooled by liquid N_2 and liquid He down to 4.2 K. To vacuum liquid He was cooled down to around 2 K. During the cooling of the cell, the pressure changes due to the thermal contractions and stiffening of the various parts of the cell, compressing medium and sample. The pressure keeps constant to temperature change. The pressure was determined from the measurements of the resistivity change of bismuth associated with the phase transitions, Bi I-II (2.55 GPa), II-III(2.7 GPa) and III-V(7.7 GPa) at room temperature. Pressure was also determined at low temperatures from the superconducting transition temperature T_c of lead with the pressure coefficient of $dT_c/dP = -3.81 \times 10^{-1}$ K/GPa up to 2.5 GPa. Above 2.5 GPa the pressure was estimated from a pressure-load caliblation curve at room temperature.

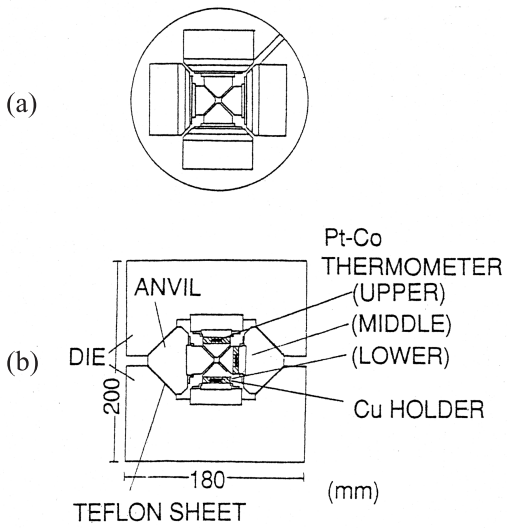

Fig. 3.2 Cubic anvil device: top(a) and side(b) views.

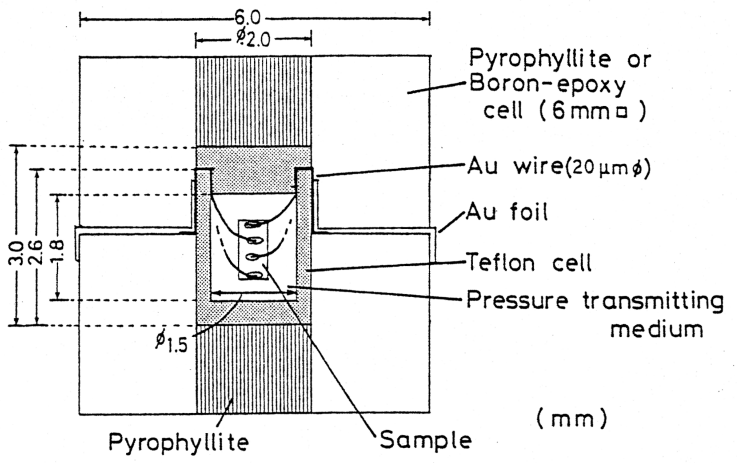

Fig. 3.3 Cross-sectional view of internal configuration of gasket with teflon capsule.

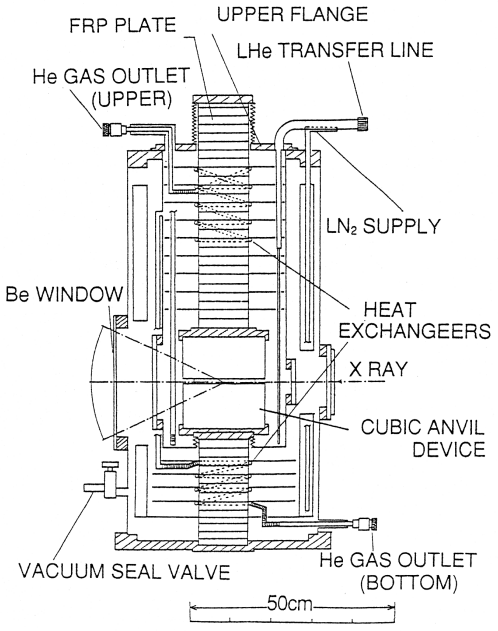

Fig. 3.4 Cross-sectional view of high pressure cryostat.

(c) Bridgman anvil

Figure 3.5 shows the cross-section view of the lower part of the apparatus, consisting of three parts: the pistons driven by a hydraulic press, the modified-Bridgman anvils made of tungsten carbide, in which pressure is produced by the advance of the piston, and the holder made of Cu-Be.

The force applied to the piston is controlled by a hydraulic press in order to keep the load constant during the measurement in the cooling and warming processes. Therefore, pressure remains almost constant in a wide range of temperature, as shown in the results described below.

Figure 3.6 shows the top and side views of the sample assembly, illustrating the configration for the Hall-effect measurement. A sample with a typical size of about 0.6 0.4 0.2 mm^3 is set up in a Teflon cell of 1.8 mm in height with inner and outer diameters of 1.0 and 1.5 mm, respectively. The Teflon cell is filled with a 1 : 1 mixture of Fluorinert FC70 and FC77 as a pressure transmitting medium. Au wires of 20μmϕ, attached to the sample, are connected to each part of a four divided stainless-steel disk with 0.15 mm in thickness, and to the upper anvil by Au foils 10 μm thick. In order to ensure electrical insulation, the surfaces of the stainless steels and the anvils are coated with epoxy resin. Stycast is also used between the parts of a divided stainless-steel disk.

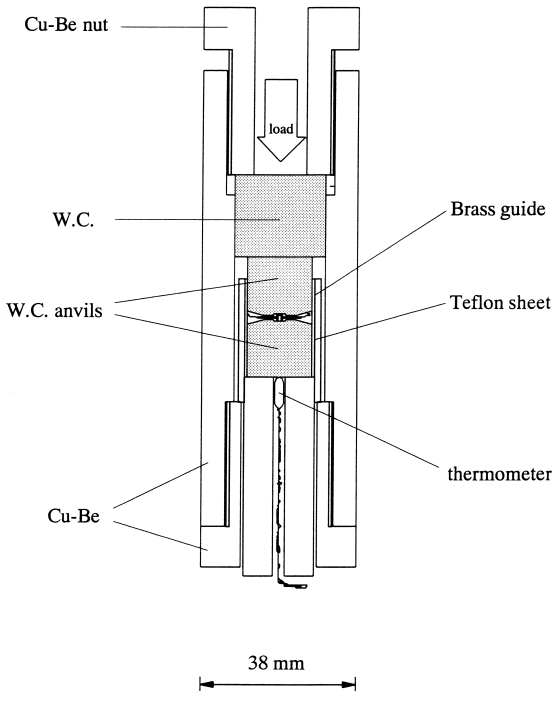

Fig. 3.5 Cross-section view of the lower part of the apparatus [88].

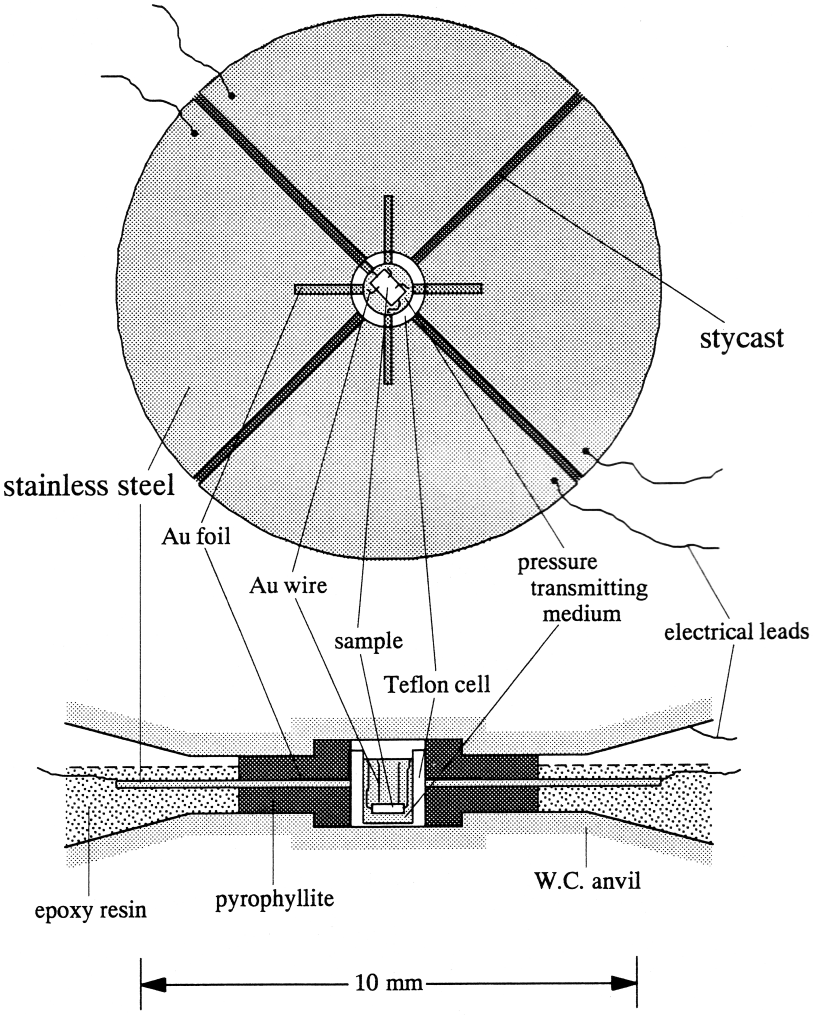

Fig. 3.6 Top and side views of the sample assembly with a five-probe configuration [88].

(d) Indenter cell

Indenter cell has been developed by Kobayashi *et al.* Figure 3.7 show the indenter cell. The sample is set on the WC piston, as shown in Fig. 3.8. The piston indented in the holl made of NiCrAl or MP35N, and the pressure is hold by the clamp nut. When pressure is applied, high pressure up to about 4 GPa is realized by piston and gusket, as shown in Fig. 3.7. We used Daphne7373 oil as a pressure transmitting medium.

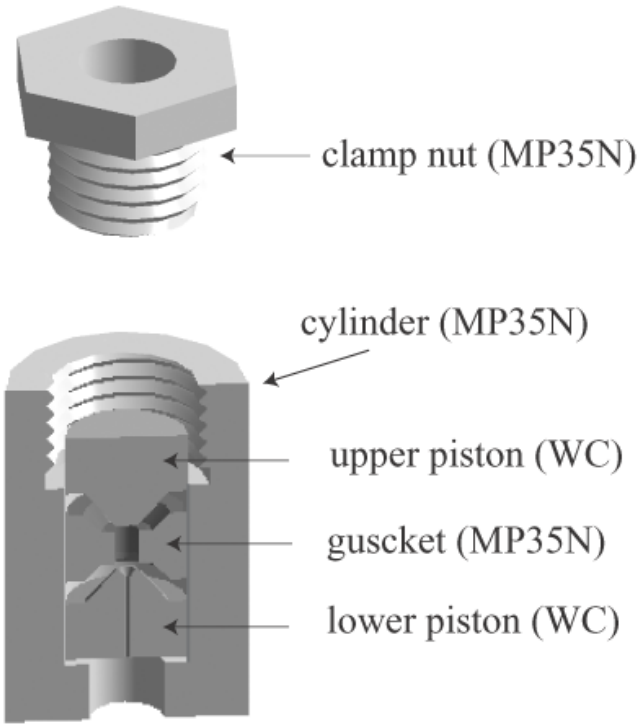

Fig. 3.7 Cross-sectional view of indenter cell.

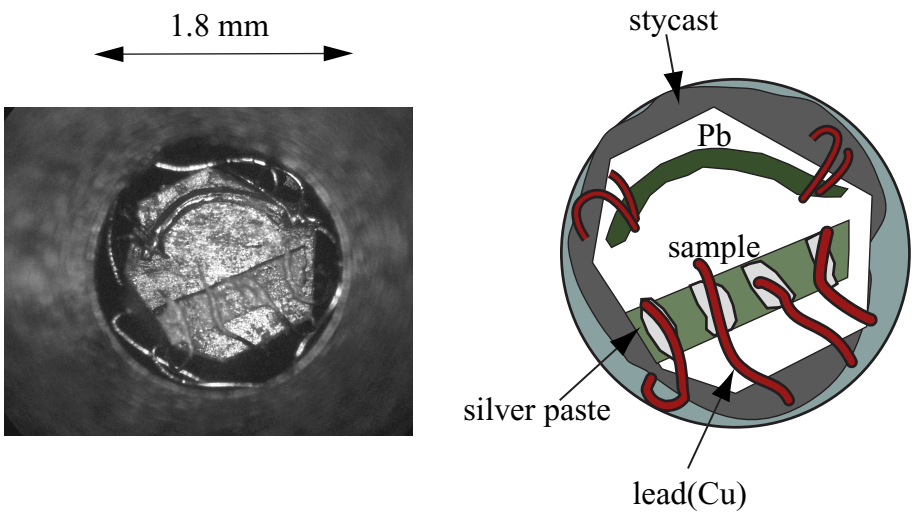

Fig. 3.8 Top view of the sample setting on the lower piston.

3.2 de Haas-van Alphen effect

3.2.1 Introduction to the de Haas-van Alphen effect

Under a high magnetic field, the orbital motion of the conduction electron is quantized and forms Landau levels[89]. Therefore various physical qualities shows a periodic variation with H^{-1} since increasing the field strength H causes a sharp change in the free energy of the electron system when Landaus level cross the Fermi energy. In a three-dimensional system this sharp structure is observed at extremal areas in $\boldsymbol{k}$-space, perpendicular to the field direction and enclosed by the Fermi energy because the density of state also becomes extremal. From the field and temperature dependence of various physical quantities, we can obtain the extremal area S, the cyclotron mass m_{c}^* and the scattering lifetime τ for this cyclotron orbit. The magnetization or the magnetic susceptibility is the most common one of these physical quantities, and its periodic character is called the de Haas-van Alphen (dHvA) effect. It provides one of the best tools for the investigation of Fermi surfaces of metals.

The theoretical expression for the oscillatory component of magnetization M_{osc} due to the conduction electrons was given by Lifshitz and Kosevich as follows:

$$M_{\mathrm{osc}} = \sum_r \sum_i \frac{(-1)^r}{r^{3/2}} A_i \sin\left(\frac{2\pi r F_i}{H} + \beta_i\right), \tag{3.1a}$$

$$A_i \propto F H^{1/2} \left|\frac{\partial^2 S_i}{\partial {k_{\mathrm{H}}}^2}\right|^{-1/2} R_{\mathrm{T}} R_{\mathrm{D}} R_{\mathrm{S}}, \tag{3.1b}$$

$$R_{\mathrm{T}} = \frac{\alpha r m_{ci}^* T/H}{\sinh(\alpha r m_{ci}^* T/H)}, \tag{3.1c}$$

$$R_{\mathrm{D}} = \exp(-\alpha r m_{ci}^* T_{\mathrm{D}}/H), \tag{3.1d}$$

$$R_{\mathrm{S}} = \cos(\pi g_i r m_{ci}^*/2m_0), \tag{3.1e}$$

$$\alpha = \frac{2\pi^2 k_{\mathrm{B}}}{e\hbar}. \tag{3.1f}$$

Here the magnetization is periodic on $1/H$ and has a dHvA frequency F_i

$$\begin{aligned} F_i &= \frac{\hbar}{2\pi e} S_i \\ &= 1.05 \times 10^{-12}\ [\mathrm{T}\cdot\mathrm{cm}^2]\cdot S_i, \end{aligned} \tag{3.2}$$

which is directly proportional to the i-th extremal (maximum or minimum) cross-sectional area S_i $(i = 1, \ldots, n)$. The extremal area means a gray plane in Figure 3.9, where there is one extremal area in a spherical Fermi surface. The factor R_{T} in the amplitude A_i is related to the thermal damping at a finite temperature T. The factor R_{D} is also related to the Landau level broadening $k_{\mathrm{B}}T_{\mathrm{D}}$. Here T_{D} is due to both the lifetime broadening and inhomogeneous broadening caused by impurities, crystalline imperfections or strains.

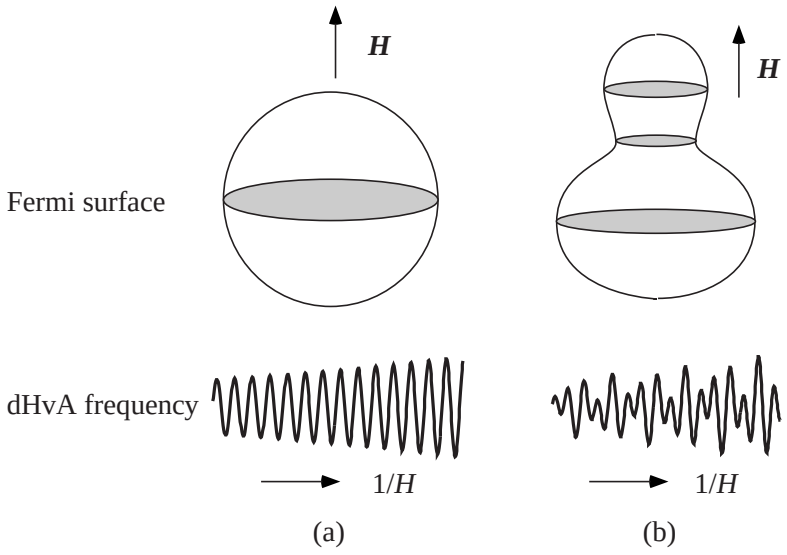

Fig. 3.9 Simulations of the cross-sectional area and its dHvA signal for a simple Fermi surface. There is one dHvA frequency in (a), while there are three different frequencies in (b).

The factor T_{D} is called the Dingle temperature and is given by

$$\begin{aligned} T_{\mathrm{D}} &= \frac{\hbar}{2\pi k_{\mathrm{B}}}\tau^{-1} \\ &= 1.22 \times 10^{-12}\ [\mathrm{K}\cdot\mathrm{sec}]\cdot\tau^{-1}. \end{aligned} \tag{3.3}$$

The factor R_{S} is called the spin factor and related to the difference of phase between the Landau levels due to the Zeeman split. When $g_i = 2$ (a free electron value) and $m_{\mathrm{c}}^* = 0.5m_0$, this term becomes zero for $r = 1$. The fundamental oscillation vanishes for all values of the field. This is called the zero spin splitting situation in which the up and down spin contributions to the oscillation cancelled out, and this can be useful for determining the value of g_i. Note that in this second harmonics for $r = 2$ the dHvA oscillation should show a full amplitude. The quantity $|\partial^2 S/\partial {k_{\mathrm{H}}}^2|^{-1/2}$ is called the curvature factor. The rapid change of cross-sectional area around the extremal area along the field direction diminishes the dHvA amplitude for this extremal area.

The detectable conditions of dHvA effect are as follows:

1) The distance between the Landau levels $\hbar\omega_{\mathrm{c}}$ must be larger than the thermal broadening width $k_{\mathrm{B}}T$: $\hbar\omega_{\mathrm{c}} \ll k_{\mathrm{B}}T$ (high fields, low temperatures).

2) At least one cyclotron motion must be performed during the scattering, namely $\omega_{\mathrm{c}}\tau/2\pi > 1$ (high quality samples). In reality, however, it can be observed even if a cyclotron motion is about ten percent of one cycle.

3) The fluctuation of the static magnetic field must be smaller than the field interval of one cycle of the dHvA oscillation (homogeneity of the magnetic field).

3.2.2 Shape of the Fermi surface

The angular dependence of dHvA frequencies gives very important information about a shape of the Fermi surface. As a value of Fermi surface corresponds to a carrier number, we can obtain the carrier number of a metal directly.

We show the typical Fermi surfaces and their angular dependences of dHvA frequencies in Figure 3.10. In a spherical Fermi surface, the dHvA frequency is constant for any field direction. On the other hand, in a ellipsoidal Fermi surface such as in Figure 3.10(b), it takes a minimum value for the field along the z-axis. These relatively simple shape Fermi surfaces can be determined only by the experiment. However, information from an energy band calculation is needed to determine a complicated one.

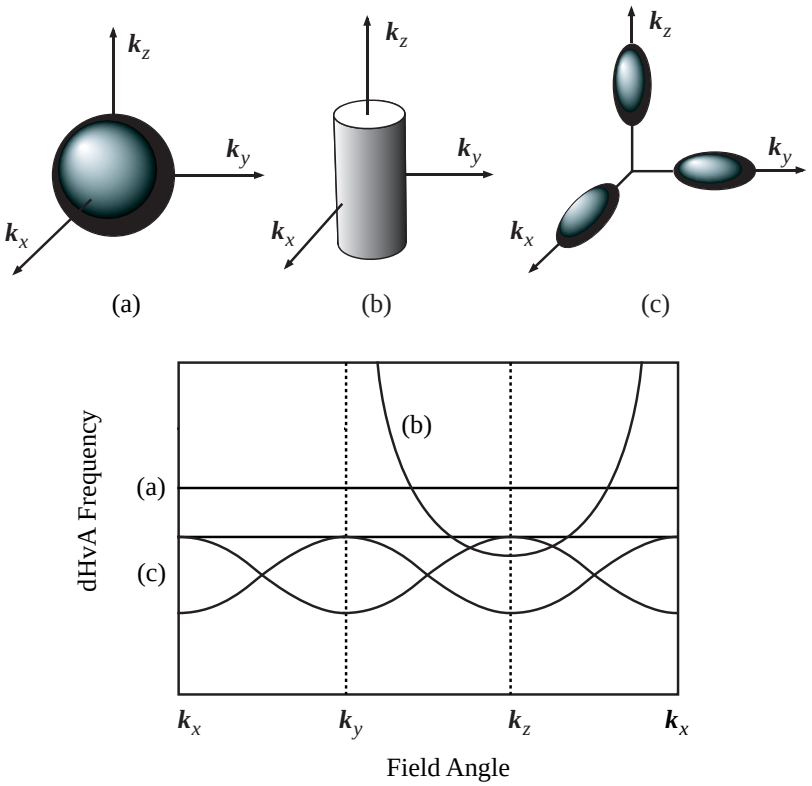

Fig. 3.10 Angular dependence of the dHvA frequency in three typical Fermi surfaces (a) sphere, (b) cylinder and (c) ellipsoid.

3.2.3 Cyclotron effective mass

We can determine the cyclotron effective mass m^*_{ci} from the measuring a temperature dependence of a dHvA amplitude. Equation (3.1c) is transformed into

$$\log\left\{A_i\left[1-\exp\left(\frac{-2\alpha m^*_{ci}T}{H}\right)\right]/T\right\}=\frac{-\alpha m^*_{ci}}{H}T+\text{const.} \tag{3.4}$$

Therefore, from the slope of a plot of $\log\{A_i[1-\exp(-2\lambda m^*_{ci}T/H)]/T\}$ versus T at constant field H, the effective mass can be obtained.

Let us consider the relation between the cyclotron mass and the electrical specific heat γ. Using a density of states $D(E_\mathrm{F})$, γ is written as

$$\gamma=\frac{\pi^2}{3}{k_\mathrm{B}}^2D(E_\mathrm{F}). \tag{3.5}$$

In the spherical Fermi surface, using $E_\mathrm{F}=\hbar^2{k_\mathrm{F}}^2/2m^*_\mathrm{c}$ takes

$$\begin{aligned}\gamma&=\frac{\pi^2}{3}{k_\mathrm{B}}^2\frac{V}{2\pi^2}\left(\frac{2m^*_\mathrm{c}}{\hbar^2}\right)^{3/2}{E_\mathrm{F}}^{1/2}\\&=\frac{{k_\mathrm{B}}^2V}{3\hbar^2}m^*_\mathrm{c}k_\mathrm{F},\end{aligned} \tag{3.6}$$

where V is molar volume and $k_\mathrm{F}=(S_\mathrm{F}/\pi)^{1/2}$. We obtain from eq. (3.2)

$$\begin{aligned}\gamma&=\frac{{k_\mathrm{B}}^2m_0}{3\hbar^2}\left(\frac{2e}{\hbar}\right)^{1/2}V\frac{m^*_\mathrm{c}}{m_0}F^{1/2}\\&=2.87\times10^{-4}\ [(\mathrm{mJ/K^2\cdot mol})(\mathrm{mol/cm^3})\mathrm{T}^{-1/2}]\cdot V\frac{m^*_\mathrm{c}}{m_0}F^{1/2}.\end{aligned} \tag{3.7}$$

In the case of the cylindrical Fermi surface,

$$\begin{aligned}\gamma&=\frac{\pi^2}{3}{k_\mathrm{B}}^2\frac{V}{2\pi^2\hbar^2}m^*_\mathrm{c}k_z\\&=\frac{{k_\mathrm{B}}^2V}{6\hbar^2}m^*_\mathrm{c}k_z,\end{aligned} \tag{3.8}$$

where the Fermi wave number k_z is parallel to an axial direction of the cylinder. If we regard simply the Fermi surfaces as sphere, ellipse or cylinder approximately and then we can calculate them.

3.2.4 Dingle temperature

We can determine the Dingle temperature T_D from measuring a field dependence of a dHvA amplitude. Equations (3.1b)-(3.1d) yield

$$\log\left\{A_iH^{1/2}\left[1-\exp\left(\frac{-2\lambda m^*_{ci}T}{H}\right)\right]\right\}=-\lambda m^*_{ci}(T+T_\mathrm{D})\frac{1}{H}+\text{const.} \tag{3.9}$$

From the slope of a plot of $\log\{A_i H^{1/2}[1-\exp(-2\lambda m^*_{ci}T/H)]\}$ versus $1/H$ at constant T, the Dingle temperature can be obtained. Here, the cyclotron effective mass must have been already obtained.

We can estimate the mean free path l or the scattering life time τ from the Dingle temperature. The relation between an effective mass and life time takes the form

$$\hbar k_{\mathrm{F}} = m^* v_{\mathrm{F}}, \tag{3.10}$$

$$l = v_{\mathrm{F}}\tau. \tag{3.11}$$

Then eq. (3.3) is transformed into

$$l = \frac{\hbar^2 k_{\mathrm{F}}}{2\pi k_{\mathrm{B}} m^*_{\mathrm{c}} T_{\mathrm{D}}}. \tag{3.12}$$

When the extremal area can be regarded as a circle approximately, using the eq. (3.2), the mean free path is expressed as

$$\begin{aligned} l &= \frac{\hbar^2}{2\pi k_{\mathrm{B}} m_0}\left(\frac{2e}{\hbar c}\right)^{1/2} F^{1/2}\left(\frac{m^*_{\mathrm{c}}}{m_0}\right)^{-1} {T_{\mathrm{D}}}^{-1} \\ &= 77.6\ [\text{Å}\cdot \mathrm{T}^{-1/2}\cdot \mathrm{K}]\cdot F^{1/2}\left(\frac{m^*_{\mathrm{c}}}{m_0}\right)^{-1} {T_{\mathrm{D}}}^{-1}. \end{aligned} \tag{3.13}$$

3.2.5 Field modulation method

Experiments of the dHvA effect were constructed by using the usual ac-susceptibility field modulation method. Now we give an outline of the field modulation method in the present study.

A small ac-field $h_0 \cos\omega t$ is varied on an external field H_0 ($H_0 \gg h_0$) in order to obtain the periodic variation of the magnetic moment M. The sample is set up into a pair of balanced coils (pick up and compensation coils), as shown in Figure 3.11. An induced emf V will be proportional to $\mathrm{d}M/\mathrm{d}t$:

$$\begin{aligned} V &= c\frac{\mathrm{d}M}{\mathrm{d}t} \\ &= c\frac{\mathrm{d}M}{\mathrm{d}H}\frac{\mathrm{d}H}{\mathrm{d}t} \\ &= -ch_0\omega\sin\omega t\sum_{k=1}^{\infty}\frac{h_0^k}{2^{k-1}(k-1)!}\left(\frac{\mathrm{d}^k M}{\mathrm{d}H^k}\right)_{H_0}\sin k\omega t, \end{aligned} \tag{3.14}$$

where c is constant which is fixed by the number of turns in the coil and so on, and the higher differential terms of the coefficient of $\sin k\omega t$ are neglected. Calculating the $\mathrm{d}^k M/\mathrm{d}H^k$ it becomes

$$V = -c\omega A\sum_{k=1}^{\infty}\frac{1}{2^{k-1}(k-1)!}\left(\frac{2\pi h_0}{\Delta H}\right)^k \sin\left(\frac{2\pi F}{H}+\beta-\frac{k\pi}{2}\right)\sin k\omega t. \tag{3.15}$$

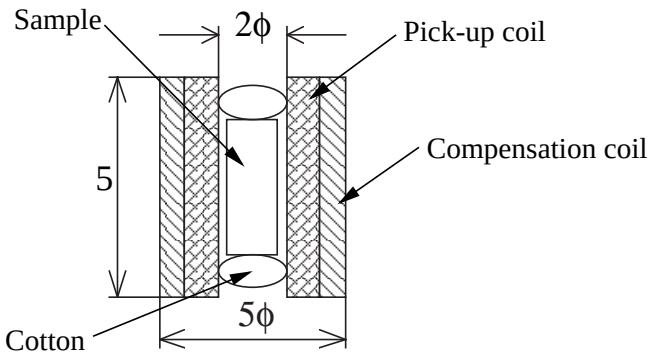

Fig. 3.11 Detecting coil and the sample location.

Here, $\Delta H = H^2/F$. Considering ${h_0}^2 \ll {H_0}^2$ the time dependence of magnetization $M(t)$ is given by

$$M(t) = A\left[J_0(\lambda)\sin\left(\frac{2\pi F}{H_0}+\beta\right) + 2\sum_{k=1}^{\infty} kJ_k(\lambda)\cos k\omega t\,\sin\left(\frac{2\pi F}{H_0}+\beta-\frac{k\pi}{2}\right)\right], \quad (3.16)$$

where

$$\lambda = \frac{2\pi F h_0}{{H_0}^2}. \quad (3.17)$$

Here, J_k is k-th Bessel function. Figure 3.12 shows the Bessel function of the first kind

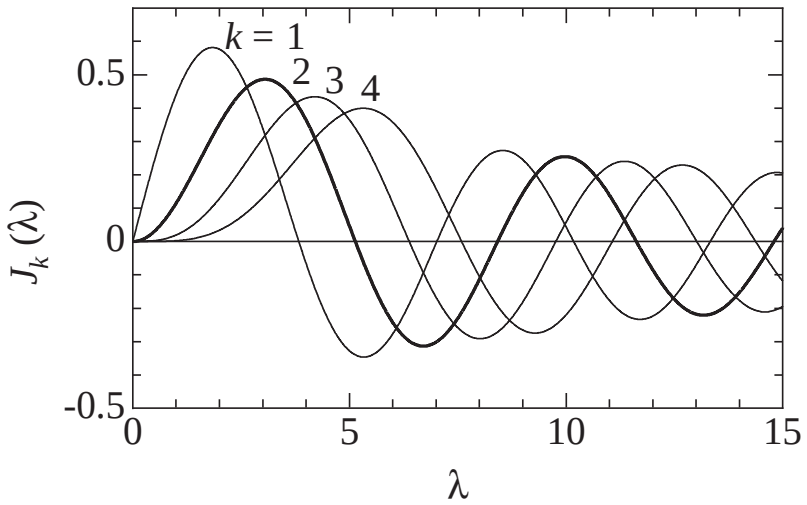

Fig. 3.12 Bessel function $J_k(\lambda)$ of the first kind.

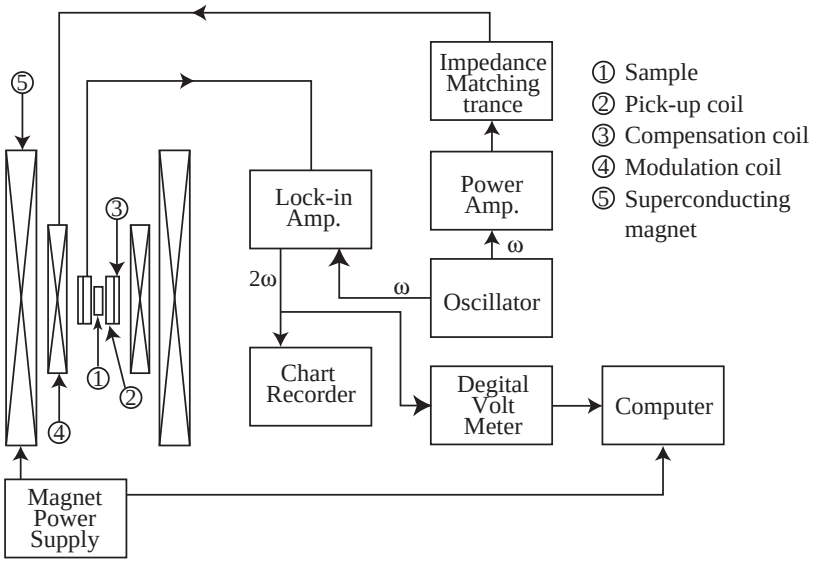

Fig. 3.13 Block diagram for the dHvA measurement.

for the various order k. Finally we can obtain the output emf as follows:

$$V = c\left(\frac{\mathrm{d}M}{\mathrm{d}t}\right) = -2c\omega A\sum_{k=1}^{\infty} kJ_k(\lambda)\sin\left(\frac{2\pi F}{H_0} + \beta - \frac{k\pi}{2}\right)\sin k\omega t. \tag{3.18}$$

The signal was detected at the second harmonic of the modulation frequency 2ω using a Lock-in Amplifier, since this condition may cut off the offset magnetization and then detect the component of the quantum oscillation only. We usually choose the modulation field h_0 to make the value of $J_2(\lambda)$ maximum, namely $\lambda = 3.1$. We used a modulation frequency of 3.5 Hz for dilution refrigerator. Figure 3.13 shows a block diagram for the dHvA measurement in the present study.

3.3 Magnetization in High Magnetic Field

We measured the high field magnetization in at High-field laboratory, Research center for extreme materials, Osaka University (KYOKUGEN).

Figure 3.14 shows the block diagram of magnetization measurement. At first, the huge condencer bank is electrically charged. When we turn on the switch of circuit, the charge flow through the magnet coil and generate high magnetic field in the coil. The long-pulse magnet that we used for this research can generate the magnetic field up to 47 T. The pulse width is 10 msec.

We used the uniaxial coil in order to compensate a background flux change due to a transient fielde, as shown in Fig. 3.14. The turn number of outer coil B is half of A, and B is twice the area of A. Ideally, we can compensete perfectly by A and B coil. However this scenario is ideal and in fact the background signals are not zero, containing linear and nonlinear components of the dH/dt. The linear component can be minimized by tuning a bridgh balance circuit connected with a compensation coil-C.

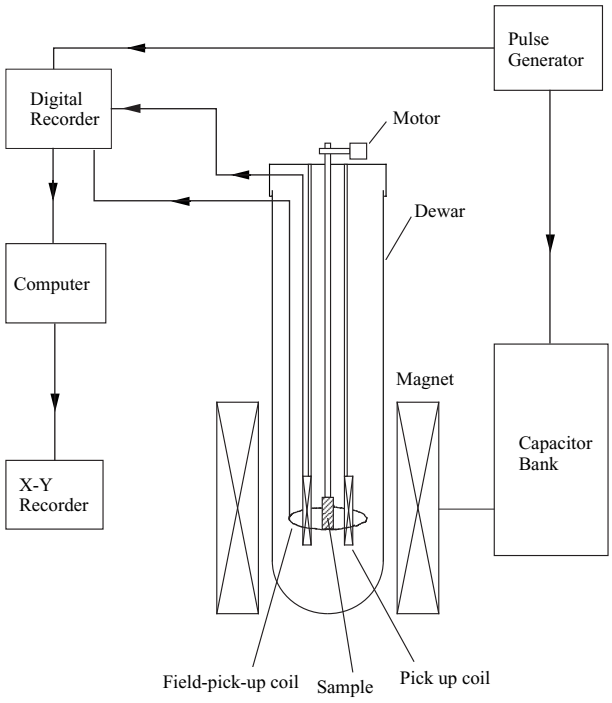

Fig. 3.14 Block diagram of measurement of magnetization with a pulse field magnet.

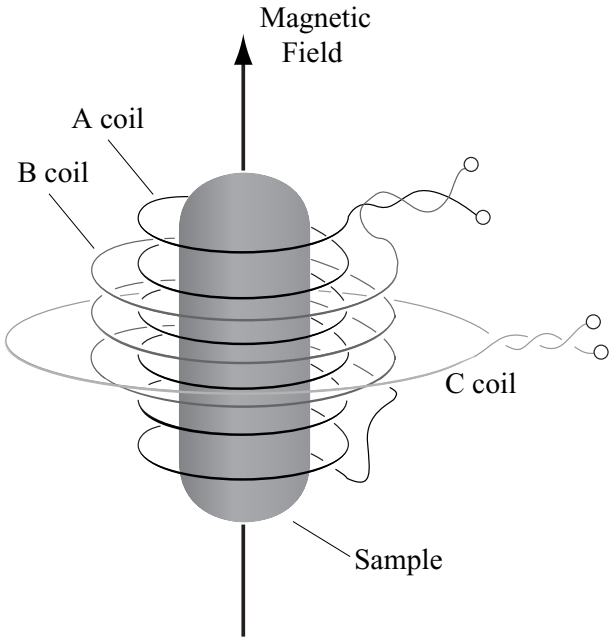

Fig. 3.15 Pick up coil.

4 Experimental Results and Analyses

4.1 Cerium Compounds

4.1.1 $CeNiGe_3$

Prior to the present pressure experiment, pressure was applied to $CeNiGe_3$ by the indenter cell up to 4.46 GPa by Tabata *et al.* Figures 4.1 and 4.2 show the temperature dependence of the electrical resistivity under pressures up to 4.46 GPa. The electrical resistivity at ambient pressure has a broad hump around 100 K and also a broad peak around 8 K, and decreases steeply below $T_N = 5.5$ K, which are the same as the previous data by Pikul *et al.* [44]. These are characteristic features in the cerium Kondo compound with antiferromagnetic ordering. As mentioned in Chap.2, there are two characteristic Kondo temperatures T_K^h and T_K in cerium Kondo compounds. For $CeNiGe_3$, T_K^h most likely corresponds to the temperature of 100 K showing the hump, which is named here $T_{\rho max1} = 100$ K, and shown by an arrow in Fig. 4.2. T_K roughly corresponds to 8 K, although $CeNiGe_3$ orders antiferromagnetically below $T_N = 5.5$ K. We define the temperature showing the broad resistivity peak as $T_{\rho max2} = 8$ K, as shown by an arrow in Fig. 4.2.

With increasing pressure, the electrical resistivity increases in magnitude, and $T_{\rho max1}$ shifts to lower temperatures, while $T_{\rho max2}$ increases with increasing pressure, as shown in Fig. 4.2. It is, however, difficult to define $T_{\rho max2}$ above 1 GPa. On the other hand, the Néel temperature increases from $T_N = 5.5$ K at ambient pressure to 8.5 K at 3.03 GPa, as shown by an arrow in Fig. 4.3, but decreases with further increasing pressure. These results are plotted in Fig. 4.4, showing the pressure dependence of T_N in $CeNiGe_3$.

To investigate the property at higher pressures, we used the cubic anvil cell up to 8 GPa. Figure 4.5 shows the temperature dependence of ρ under pressure. We show in Fig. 4.6 the logarithmic scale of temperature dependence of the electrical resistivity to clarify the behavior of resistivity at higher pressures. The resistivity data at different pressures are arbitrarily shifted downwards for simplicity. The two characteristic features at $T_{\rho max1}$ and $T_{\rho max2}$ are found to merge at 5 GPa into a single resistivity peak at $T_{\rho max} = 50$ K. This single resistivity peak at 5 GPa shifts to higher temperatures with further increasing pressure: $T_{\rho max} = 153$ K at 8.0 GPa. T_N decreases with increasing pressure and seems to disappear above 5.5 GPa, as shown by arrows in Fig. 4.7. The overall temperature dependence of the electrical resistivity around 5-6 GPa is very similar to that in a heavy fermion superconductor $CeCu_2Si_2$ [90]. On the other hand, the electrical resistivity at 8.0 GPa is typically similar to that observed in a valence fluctuating compound such as CeNi, where the $4f$ electron is itinerant [91].

Figure 4.8(a) shows the pressure dependence of the Néel temperature T_N [92]. The data shown by triangles and circles were obtained by using the indenter and cubic anvil cells, respectively. Solid lines connecting the data are guidelines. As mentioned above, the Néel temperature attains a maximum at 3 GPa, decreases rather steeply at higher pressures and becomes zero at $P_c \simeq 5.5$ GPa. The two characteristic tempratuers $T_{\rho max1}$

and $T_{\rho max2}$ merge into a single characteristic temperature $T_{\rho max}$ above 5 GPa, as shown in Fig. 4.8(b).

Here we tried to obtain the A and ρ_0 values from the T^2-dependence of the electrical resistivity at low temperatures, following a Fermi liquid relation, as shown in Fig. 4.9. The resistivity data, which were obtained by using the cubic anvil cell, are arbitrarily shifted. Solid lines represent the $\rho = \rho_0 + AT^2$ relation. The A value, which corresponds to the slope of solid line, becomes maximum around $P_c \simeq 5.5$ GPa, as shown in Figs. 4.9 and 4.8(c). The A value at 5 GPa, 10.5 $\mu\Omega$·cm/K^2 is the same as 10 $\mu\Omega$·cm/K^2 in a heavy fermion superconductor $CeCu_2Si_2$ with an extremely large γ value of 1.1 J/K^2·mol [90]. The heavy fermion state is thus formed around $P_c \simeq 5.5$ GPa. Correspondingly, the residual resistivity ρ_0 value also becomes maximum around $P_c \simeq 5.5$ GPa, as shown in Fig. 4.8(d).

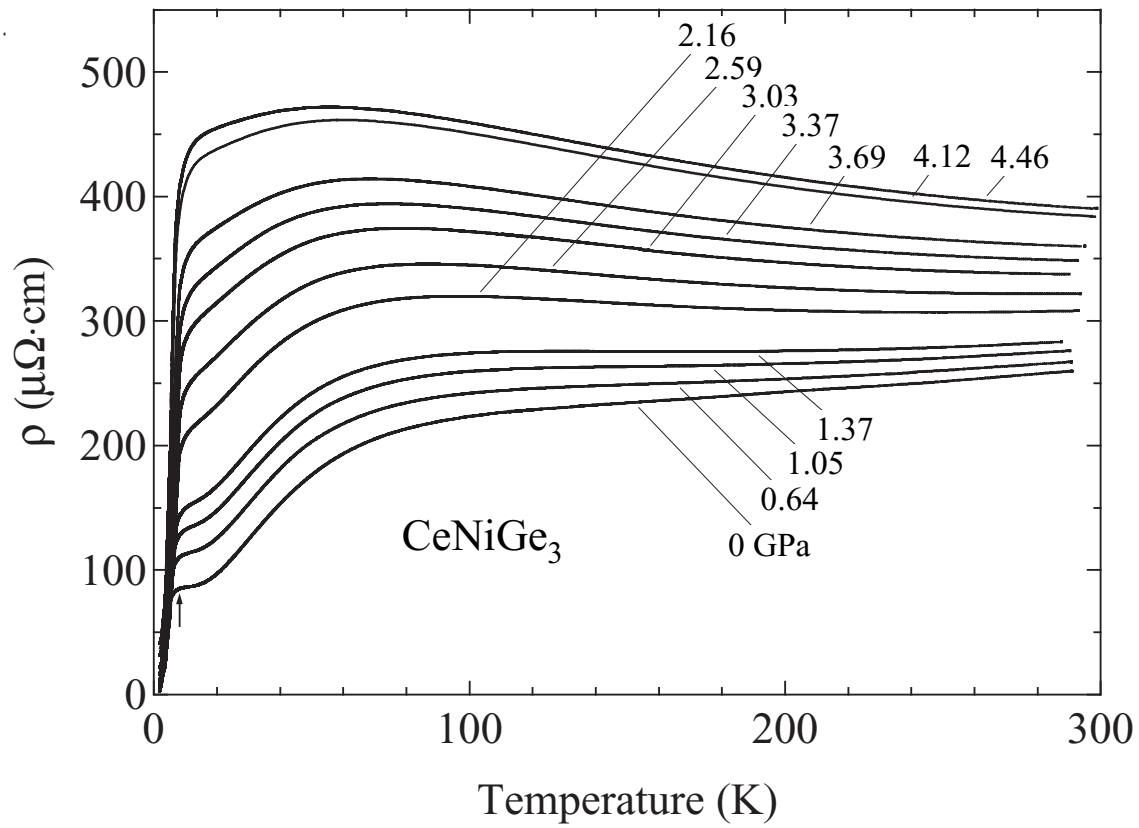

Fig. 4.1 Temperature dependence of the electrical resistivity in $CeNiGe_3$ ρ under pressure, which was applied by the indenter cell.

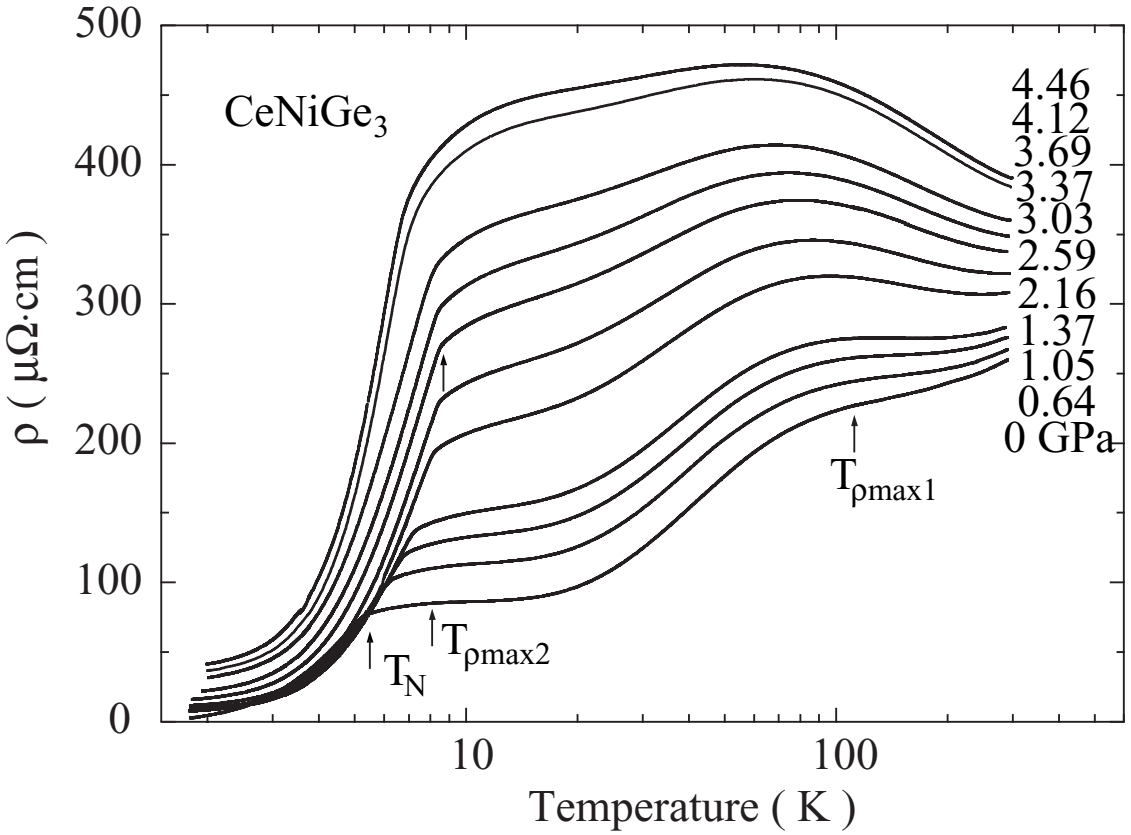

Fig. 4.2 Temperature dependence of the electrical resistivity in $CeNiGe_3$ ρ under pressure, which was applied by the indenter cell.

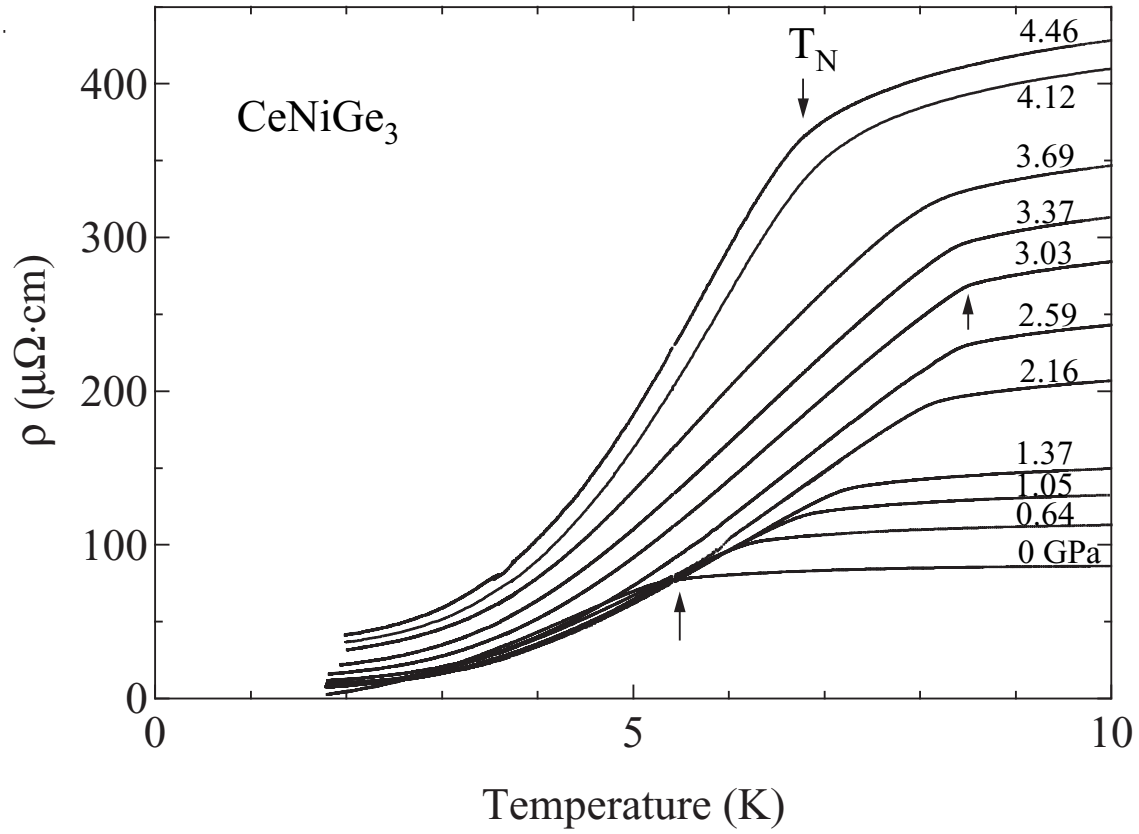

Fig. 4.3 Temperature dependence of the electrical resistivity ρ in $CeNiGe_3$ under pressure , which was applied by the indenter cell.

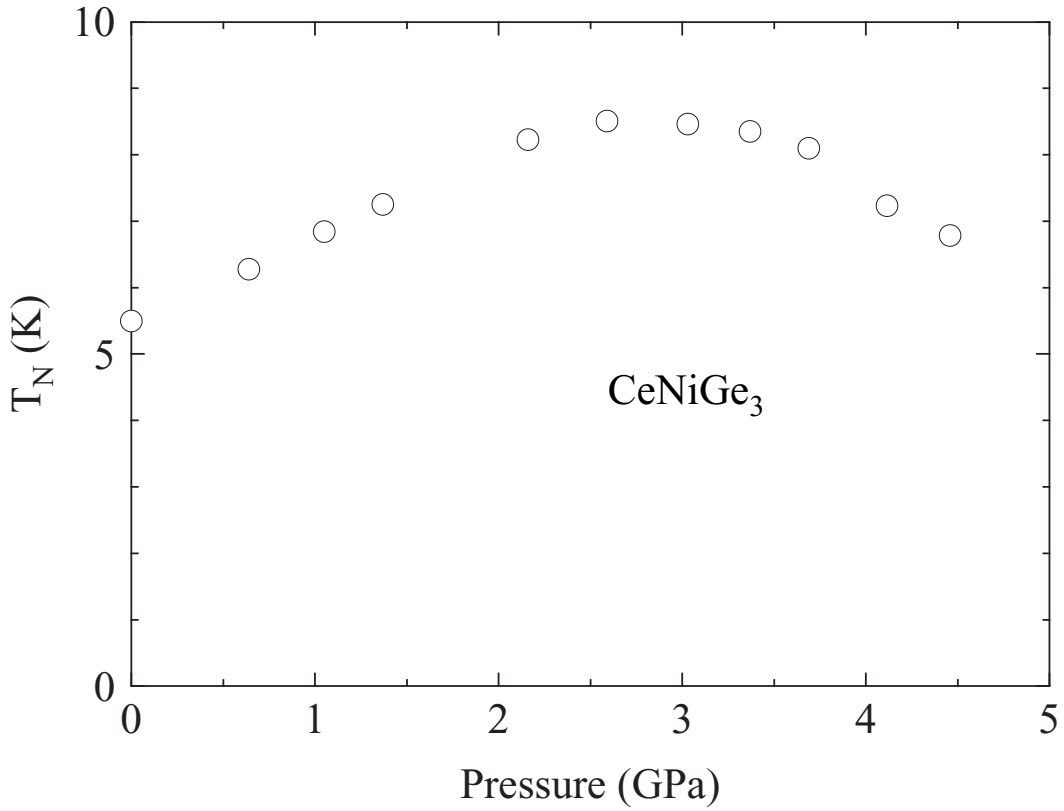

Fig. 4.4 Pressure dependence of T_{N} in $CeNiGe_3$, which was applied by the indenter cell.

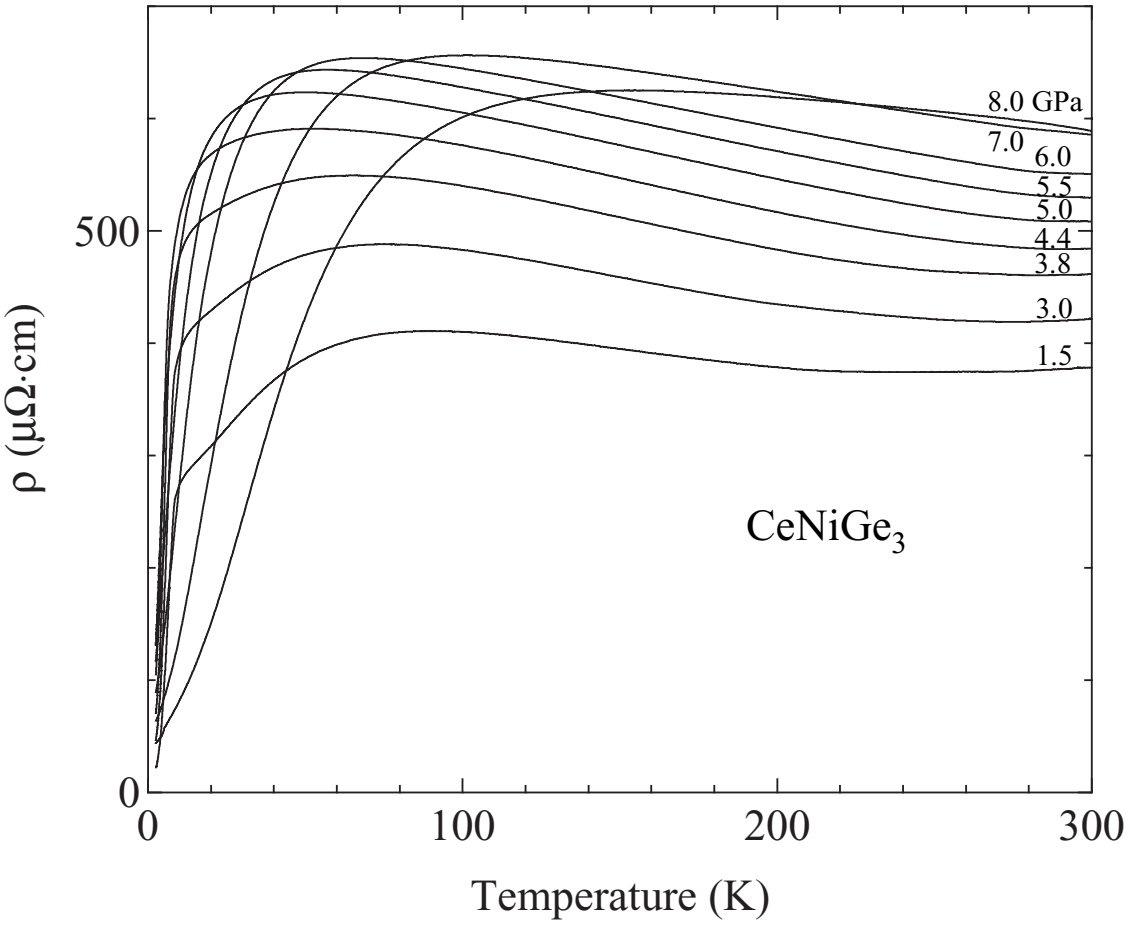

Fig. 4.5 Temperature dependence of the electrical resistivity ρ in $CeNiGe_3$ under pressure, which was applied by the cubic anvil cell.

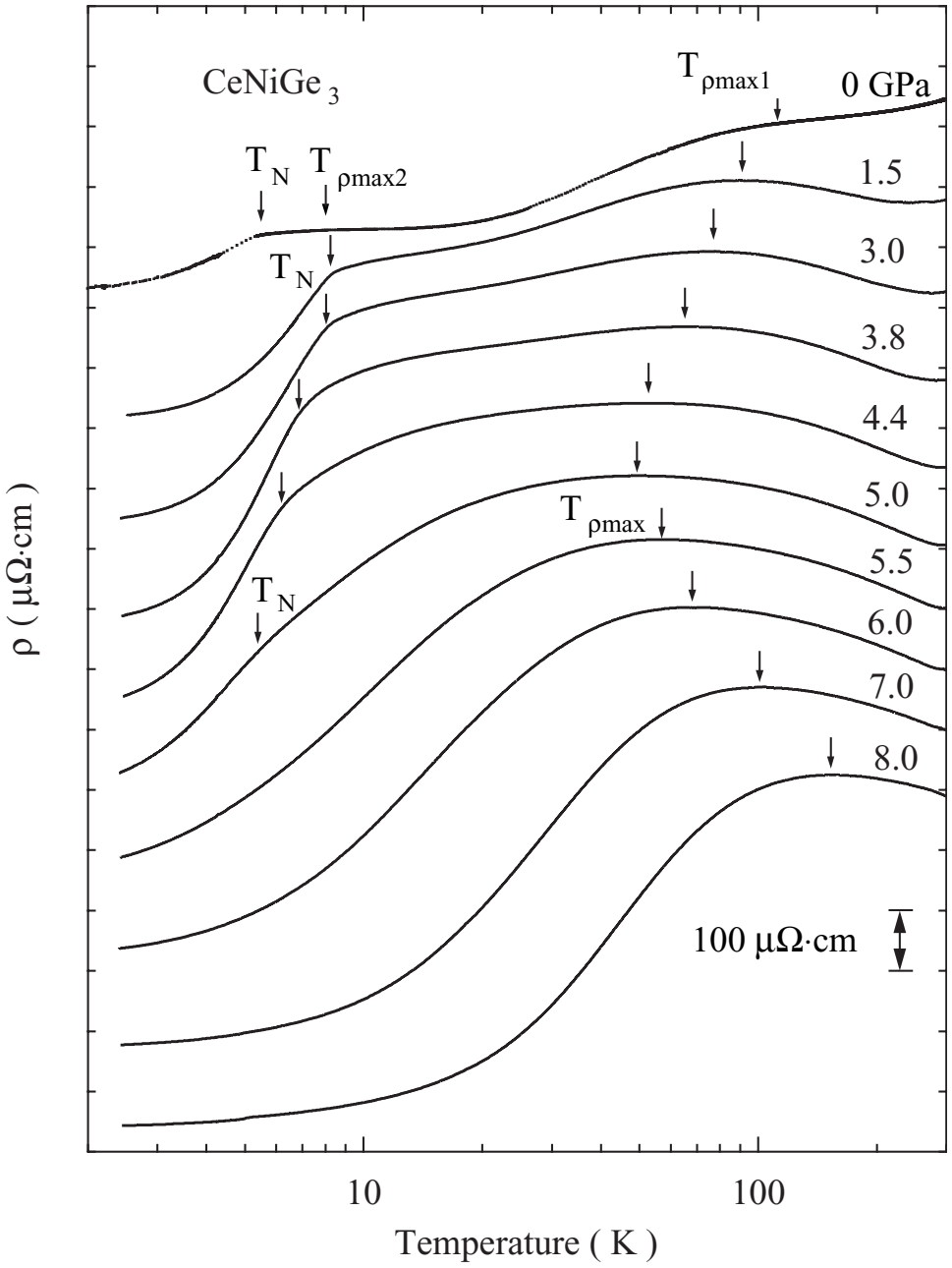

Fig. 4.6 Temperature dependence of the electrical resistivity ρ in $CeNiGe_3$ under pressure, which was applied by the cubic anvil cell.

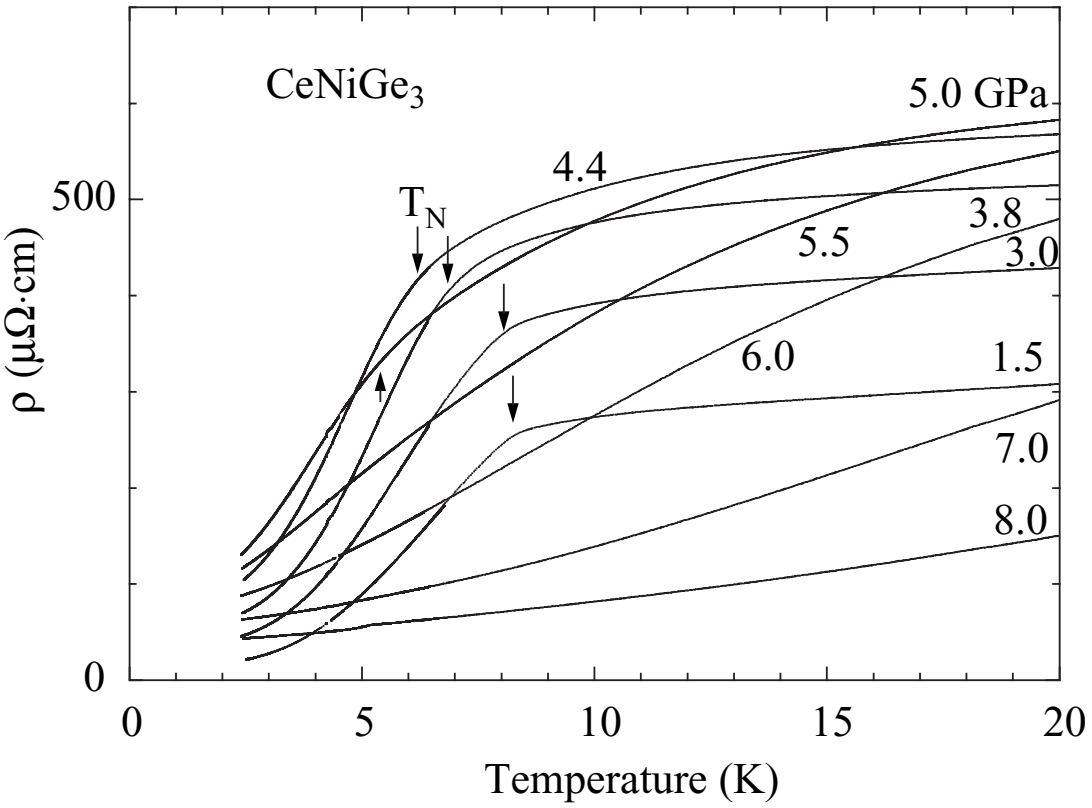

Fig. 4.7 Temperature dependence of the electrical resistivity ρ in $CeNiGe_3$ under pressure, which was applied by the cubic anvil cell.

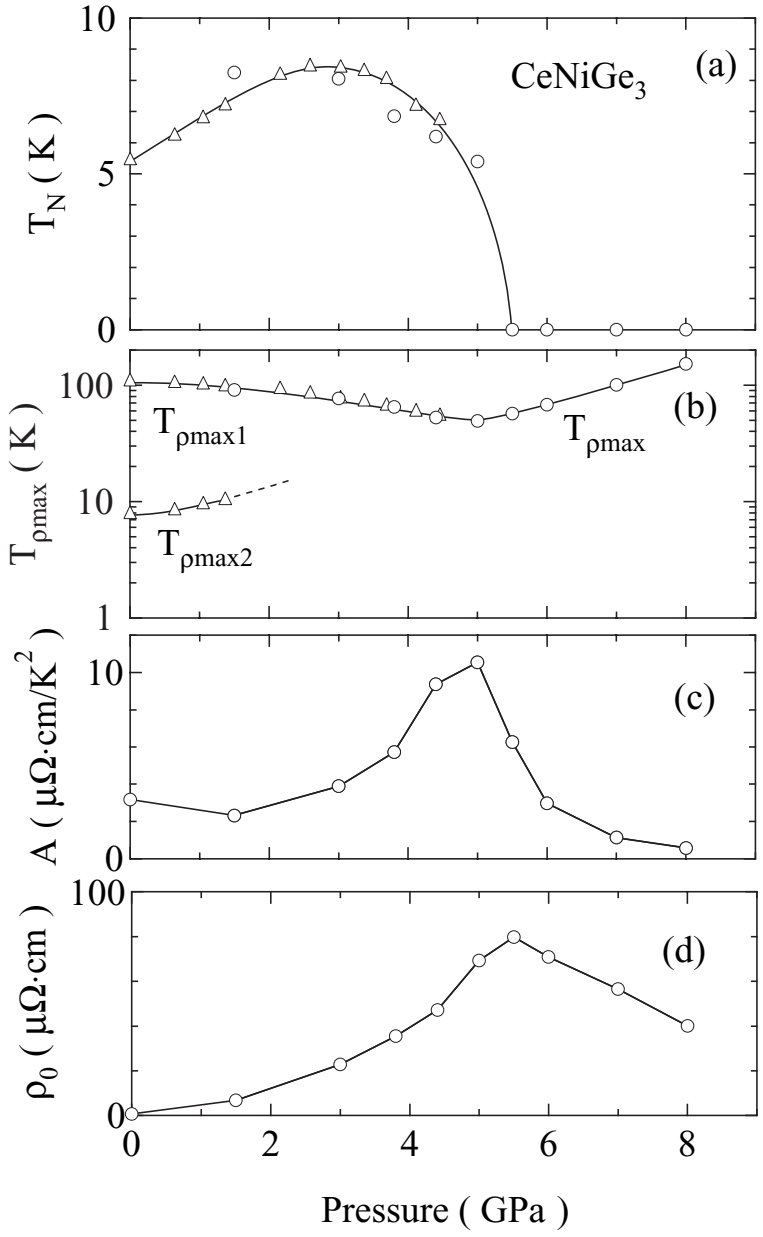

Fig. 4.8 Pressure dependence of $T_{\rm N}$, $T_{\rm sc}$, $T_{\rho{\rm max}}$, A and ρ_0 values in $CeNiGe_3$. The data shown by triangles and circles were obtained by the indenter cell and the cubic anvil cell, respectively.

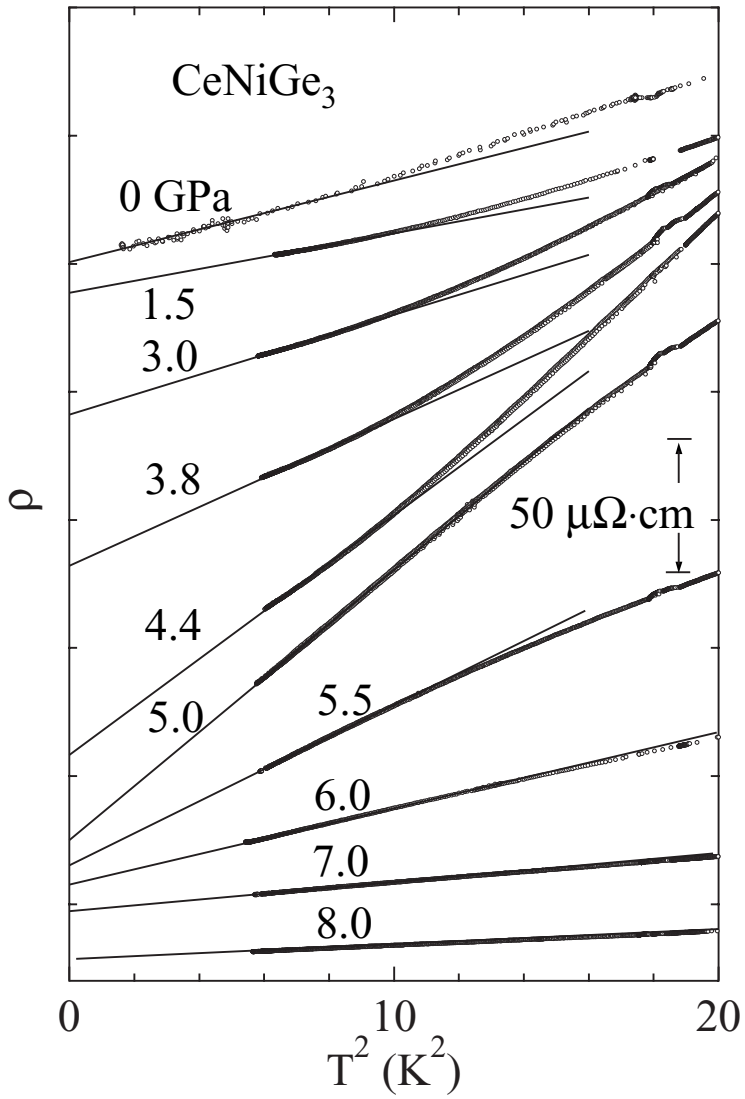

Fig. 4.9 T^2-dependence of the electrical resistivity of $CeNiGe_3$.

4.1.2 $CeNi_2Al_5$

Prior to the present pressure experiment pressure applied to $CeNi_2Al_5$ by indenter cell up to 4.3 GPa by Tabata *et al.* Figures 4.10 and 4.11 shows the temperature dependence of the electrical resistivity under pressures up to 4.3 GPa.

At ambient pressure, the $\rho(T)$ curve shows a linear decrease from 300 K and make a minimum around 25 K. Below 25 K, $\rho(T)$ increases with decreasing temperature, showing the behavior of $-\log T$. It also shows a sudden drop at 2.7 K, corresponding to the Néel temperature T_N. These characteristic features behaviors are consistent with the previous report by Isikawa *et al* [51].

T_N increases gradually with increasig pressure, and the ρ - value is considerably enhanced. The slope of $-\log T$ becomes steep, as shown in Fig. 4.11.

T_N reaches 3.9 K at 3.9 GPa and decreases slightly to 3.5 K at 4.3 GPa, as shown in Fig. 4.12. Figure 4.13 is a pressure dependence of T_N in $CeNi_2Al_5$.

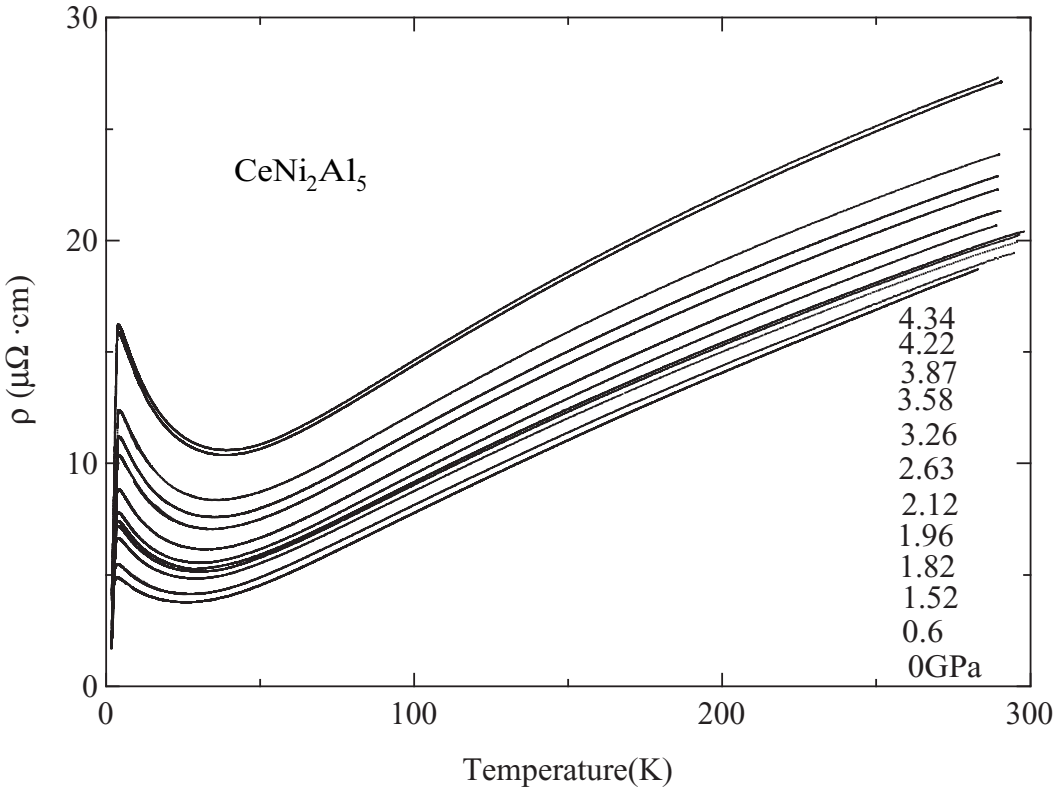

Fig. 4.10 Temperature dependence of the electrical resistivity ρ in $CeNi_2Al_5$ under pressure, which was applied by the indenter cell.

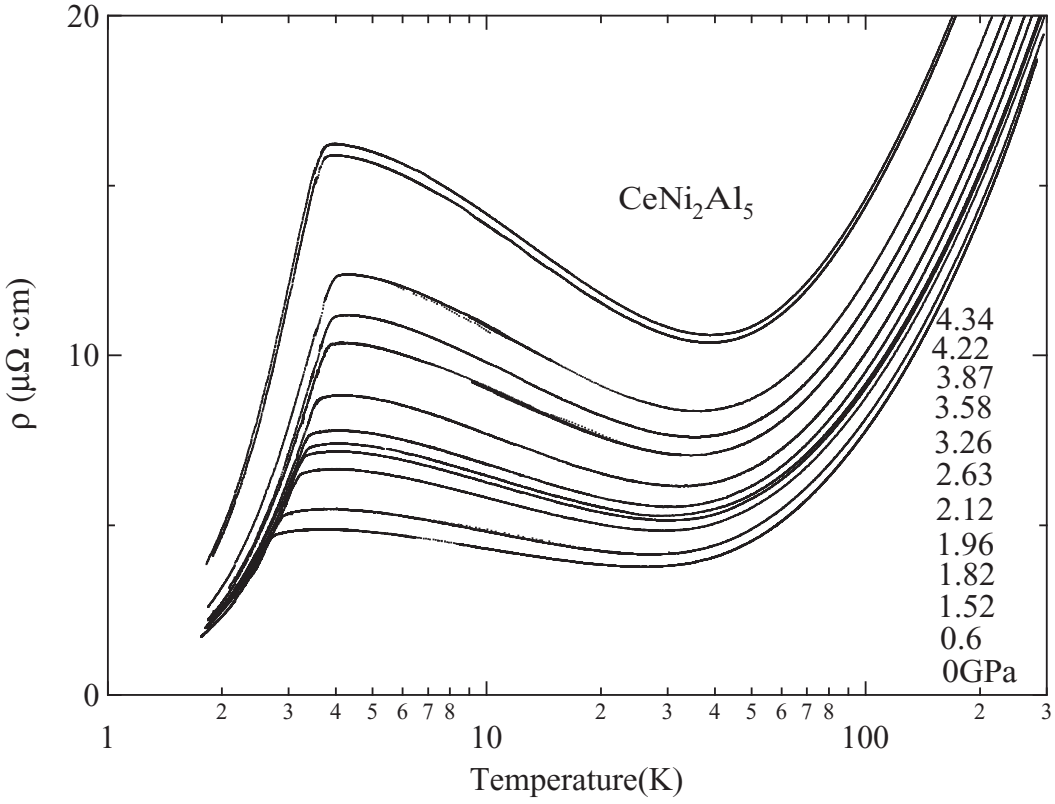

Fig. 4.11 Temperature dependence of the electrical resistivity ρ in $CeNi_2Al_5$ under pressure, which was applied by the indenter cell.

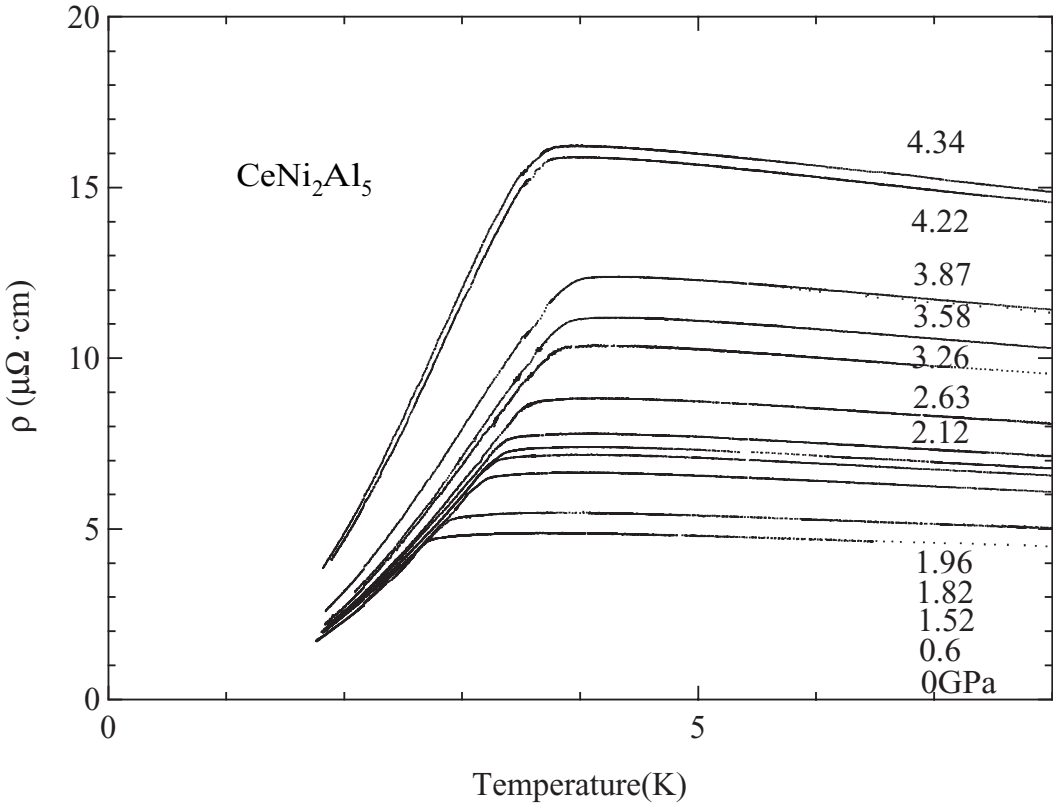

Fig. 4.12 Temperature dependence of the electrical resistivity ρ in $CeNi_2Al_5$ under pressure, which was applied by the indenter cell.

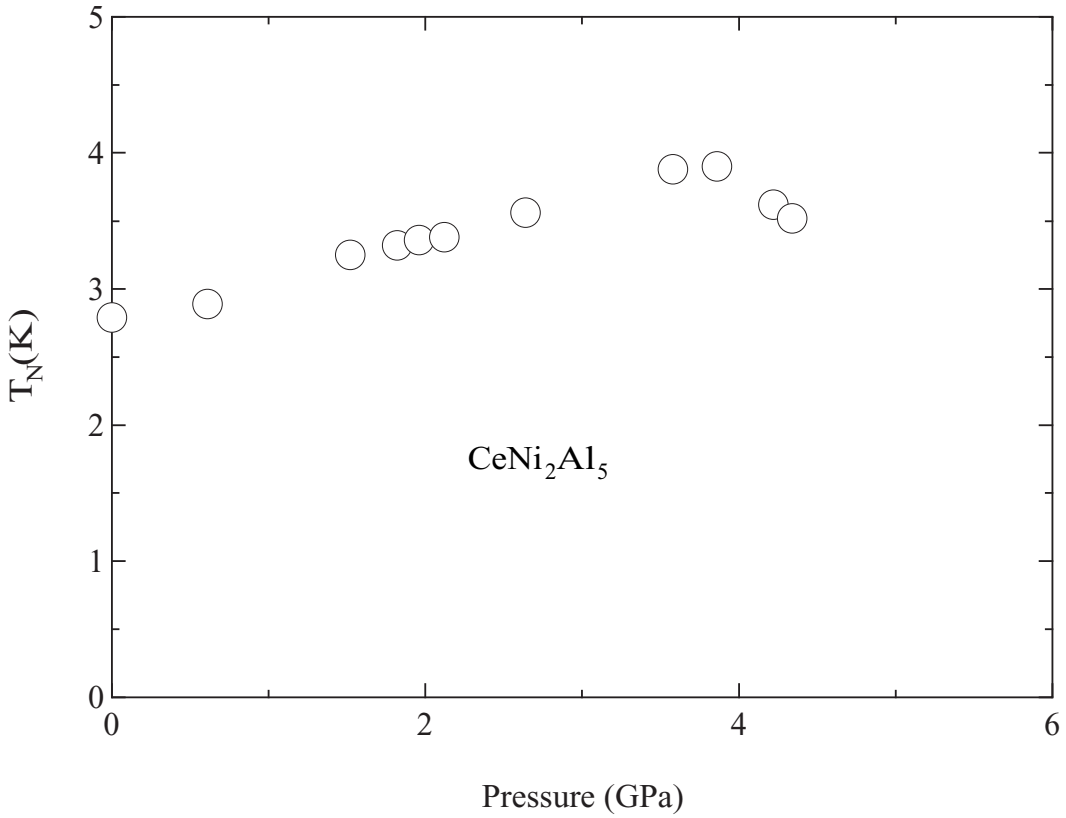

Fig. 4.13 Temperature dependence of the electrical resistivity ρ in $CeNi_2Al_5$ under pressure, which was applied by the indenter cell.

To apply higher pressures, we used the cubic anvil cell up to 8 GPa. T_N - values and the overall behavior of ρ are consistent with data obtained by the indenter cell up to 5 GPa. Applying pressures up to 6 GPa, however, changed the behavior of ρ drastically, as shown in Figs. 4.14 and 4.15. The minimum of ρ and $\log T$ - increase nearly dissapeard, as shown in Fig. 4.16. Moreover, the sudden drop of the electrical resistivity at T_N disappeared and decreased smoothly, with decreasing temperature. At this pressure, T_N seems to disappear or becomes zero. The pressure dependence of T_N is shown in Fig. 4.17. The $\rho(T)$ behavior of 7.0 GPa is also changed compered with that of 6.0 GPa. The maximum of the resistivity is not seen in the $\rho(T)$ curve.

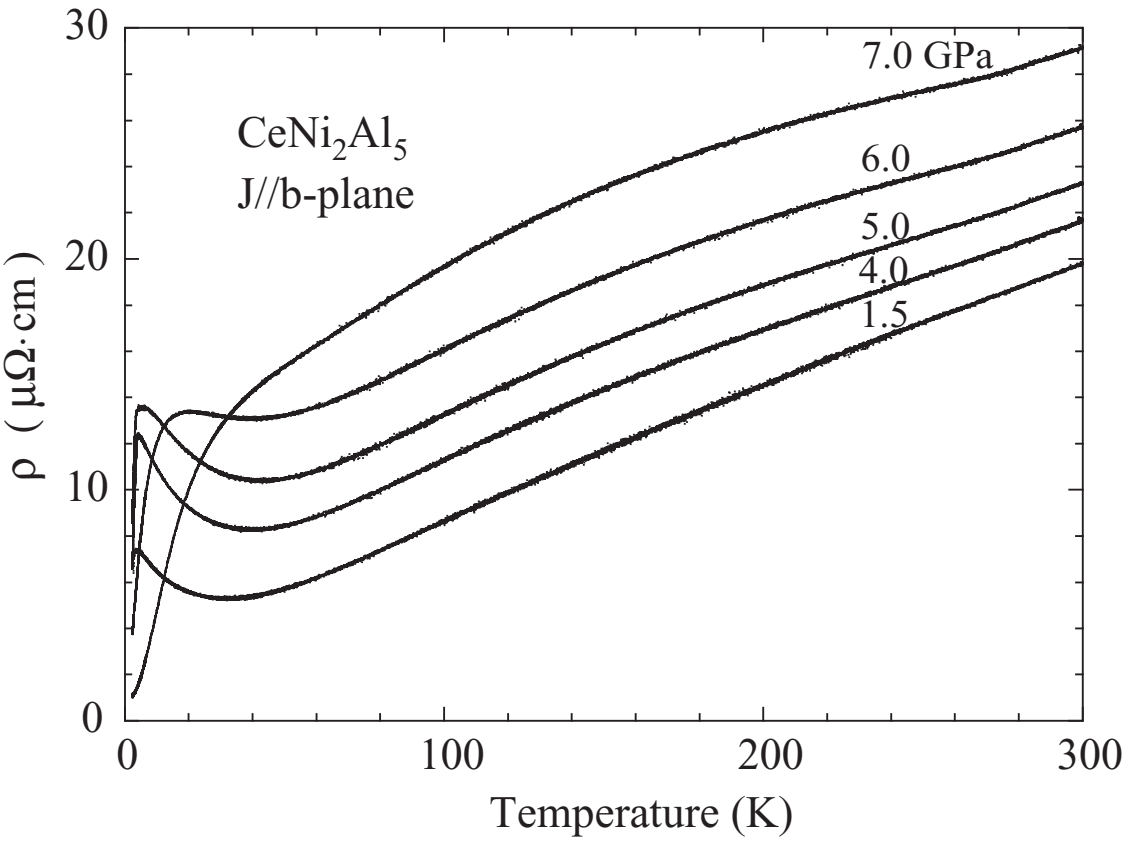

Fig. 4.14 Temperature dependence of the electrical resistivity ρ in $CeNi_2Al_5$ under pressure, which was applied by the cubic anvil cell.

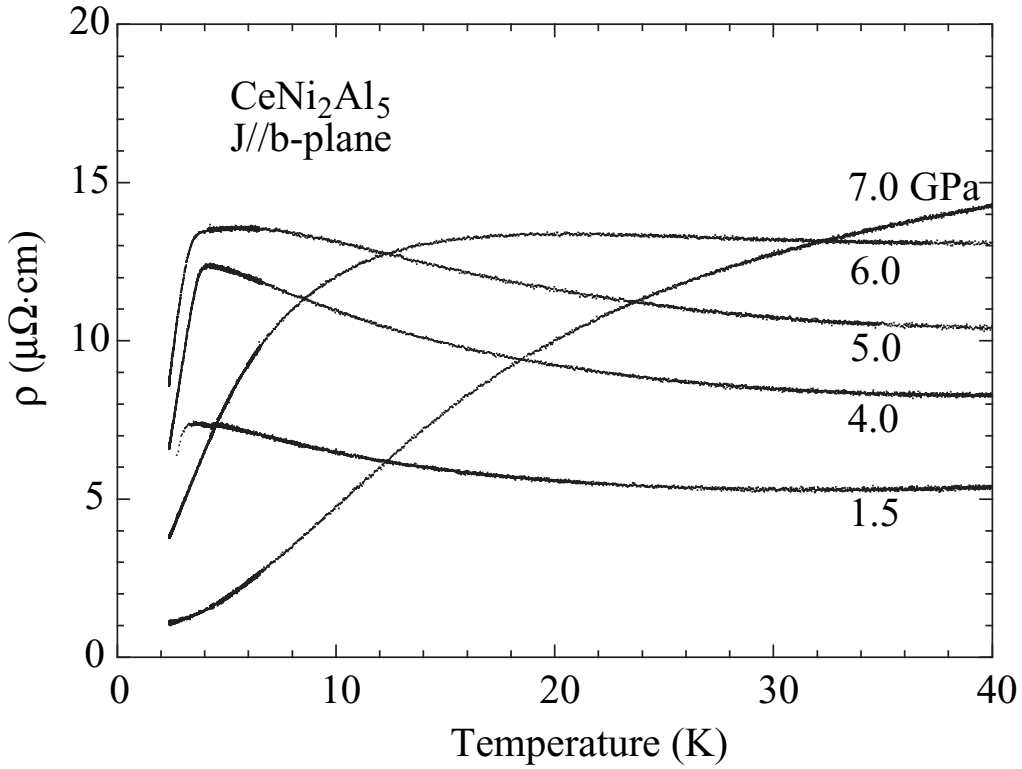

Fig. 4.15 Temperature dependence of the electrical resistivity ρ in $CeNi_2Al_5$ under pressure, which was applied by the cubic anvil cell.

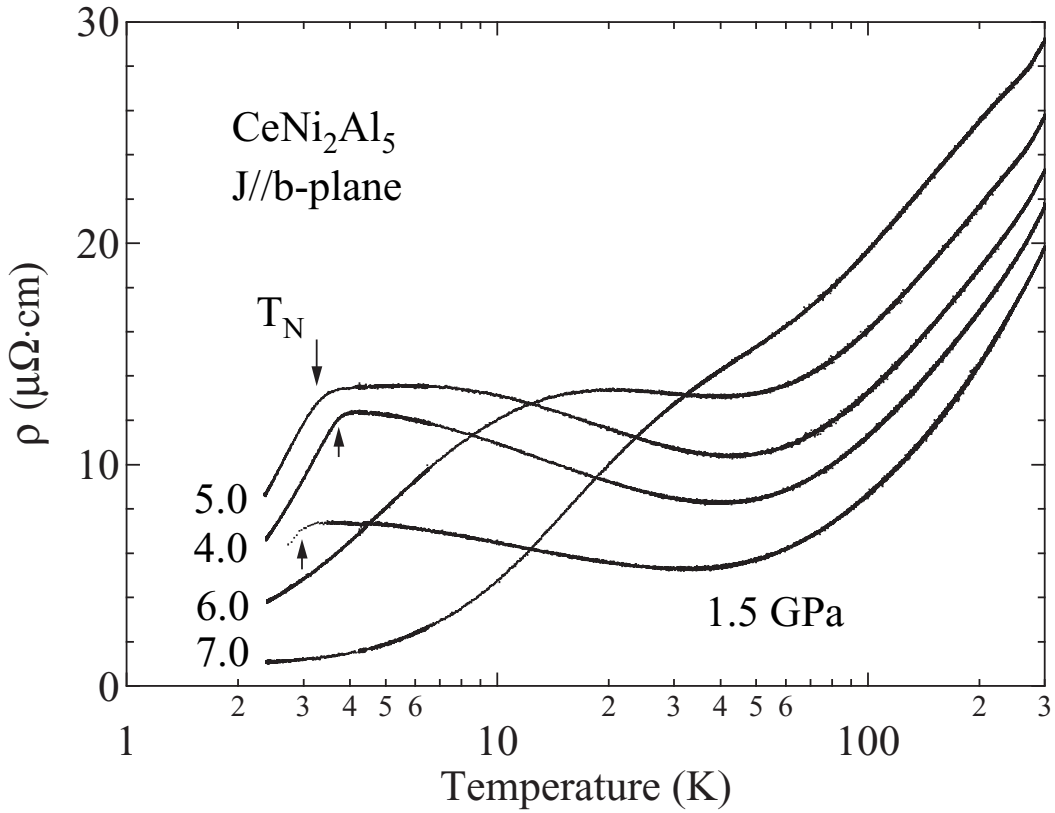

Fig. 4.16 Temperature dependence of the electrical resistivity ρ in $CeNi_2Al_5$ under pressure, which was applied by the cubic anvil cell.

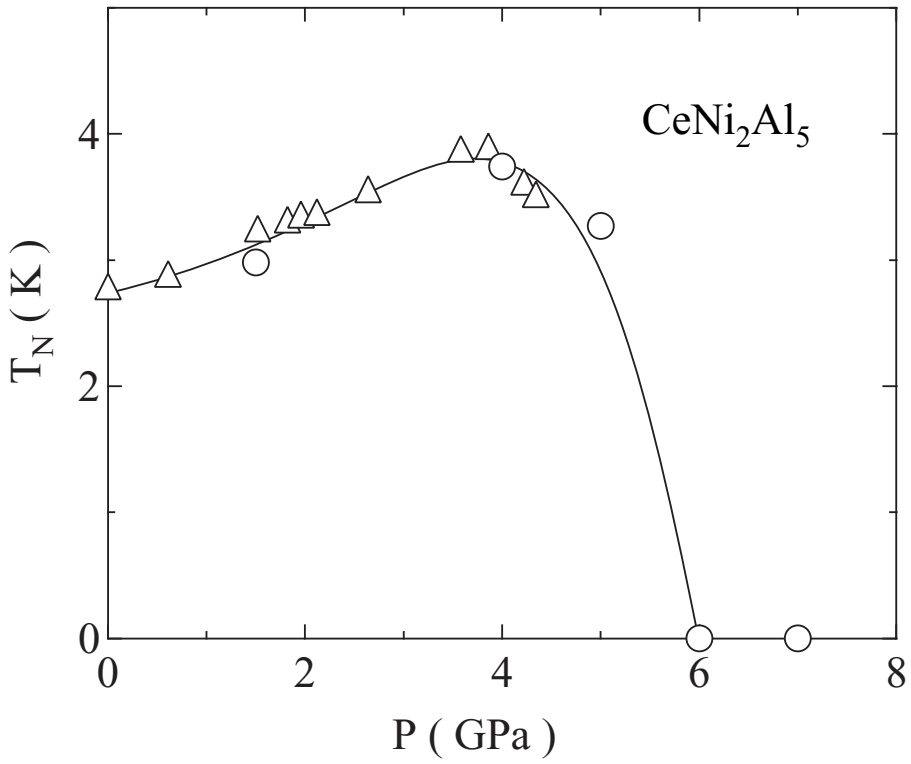

Fig. 4.17 Pressure dependence of T_{N}, obtainied by the cubic anvil cell (circles) and the indenter cell (triangles) in $CeNi_2Al_5$.

4.1.3 $CeAgSb_2$

Figure 4.18(a) shows the temperature dependence of the electrical resistivity ρ in the current J along [100] and [001]. Anisotropy of the resistivity is large: the resistivity ratio between $J \parallel$ [001] and [100] at room temperature and 10 K is $\rho_{[001]}/\rho_{[100]} = 8.3$ and 18, respectively, reflecting the quasi-two dimensional electronic state. The residual resistivity ρ_0 and residual resistivity ratio (RRR $= \rho_{RT}/\rho_0$) are 0.19 $\mu\Omega$·cm and 430 for $J \parallel$ [100], and 0.38 $\mu\Omega$·cm and 1700 for $J \parallel$ [001], indicating a high-quality sample.

Figure 4.18(b) shows the T^2-dependence of the specific heat C in the form of C/T, together with that of $LaAgSb_2$. The electronic specific heat coefficient γ is 46 mJ/K^2·mol in $CeAgSb_2$ and 2.2 mJ/K^2·mol in $LaAgSb_2$, which are approximately in agreement with the previous values for the polycrystal samples [57, 58]. We note that the magnetic specific heat C_m becomes dominant below $T_{ord} = 9.7$ K, and follows the T^3-dependence which is expected for the antiferromagnetic excitation or the antiferromagnetic ordering.

As noted above, the magnetization for $H \parallel$ [001] has a hysteresis, not shown here, as in the usual ferromagnet with a saturated moment of 0.40 μ_B/Ce, as shown in Figure 4.18(c). On the other hand, the magnetization for $H \parallel$ [100] increases almost linearly with increasing the field and saturates above 30 kOe, indicating 1.20 μ_B/Ce at 32 kOe. This corresponds to a metamagnetic transition at 30 kOe as in an antiferromagnet. We note that the magnetization curve for $H \parallel$ [100] is reversible with increasing and decreasing the field. These results of the magnetization curves are not understood from a simple ferromagnetic structure proposed by the neutron scattering experiment. The antiferromagnetic exchange interaction is essential in magnetization curves. Additional experiments such as neutron scattering on single crystals are required to clarify the magnetism in $CeAgSb_2$. We focus our interest on the pressure effect around the critical pressure P_c where the magnetic ordering temperature becomes zero.

Figure 4.19 shows the logarithmic scale of temperature dependence of the electrical resistivity in the current parallel to the (001) plane or the c-plane under several pressures. The resistivity at room temperature is 170 $\mu\Omega$·cm, which is larger than that for $J \parallel$ [100], about 80 $\mu\Omega$·cm. This is mainly due to both a small sample size and the contact of the current lead wires to the sample, related to the quasi-two dimensional nature. The resistivity thus contains the contribution of the resistivity for $J \parallel$ [001]

To clarify the magnetic ordering behavior, we show in Fig. 4.20(a) and (b) the low-temperature resistivity. The magnetic ordering temperature T_{ord} is 9.7 K at ambient pressure, as shown by an arrow. With increasing pressures T_{ord} shifts to lower temperatures. Above about 3 GPa we could not identify the magnetic ordering in the resistivity. The resistivity peak at 5.8 K for $P = 3.6$ GPa shifts to 10 K for higher pressure of 4.2 GPa. This characteristic temperature showing the resistivity peak approximately corresponds to the Kondo temperature, although it is influenced by the crystalline electric field effect. The temperature dependence of the electrical resistivity at 4.2 GPa in $CeAgSb_2$ is very similar to that of a typical non-magnetic heavy fermion compound $CeCu_6$ where the electrical resistivity increases with decreasing the temperature, has a maximum at 15 K and decreases rapidly at lower temperatures [89].

Figure 4.21 shows the pressure dependence of the magnetic ordering temperature. A solid line is a guideline:

$$T_{\rm ord}(P) = T_{\rm ord}(P=0)(1-\frac{P}{P_{\rm c}})^n \tag{4.1}$$

where $T_{\rm ord}(P=0)$ =9.7 K, $P_{\rm c} \simeq 3.3$ GPa and n =0.38. An interesting finding is that above $P_{\rm c} = 3.3$ GPa, the residual resistivity becomes extremely large, as shown in Fig. 4.20(b). The residual resistivity is about 50 $\mu\Omega$·cm, which is extremely larger than about 0.5 $\mu\Omega$·cm below $P_{\rm c}$.

Figure 4.22 shows the pressure dependence of the residual resistivity ρ_0, showing a maximum of the residual resistivity at $P_{\rm c}$. When the pressure was released, the residual resistivity was close to zero as in the case of the initial experiment. The present large residual resistivity is intrinsic and is a characteristic feature in the quantum critical region of $CeAgSb_2$.

Here the resistivity above 3.6 GPa decreases below 0.9 K, as shown by an arrow in Fig. 4.20(b). This resistivity decrease below 0.9 K was observed at 3.6, 3.8 and 4.2 GPa, and was also confirmed for another sample. There is a possibility that this is due to superconductivity, although the resistivity zero is not obtained. To clarify the present resistivity decrease, we measured the electrical resistivity under magnetic field.

Figure 4.23 shows the low temperature resistivity under $H = 0$ and 70 kOe for another sample. Configuration between $J \parallel (001)$ and $H \parallel [001]$ is transverse, $J \perp H$. The negative magnetoresistance is observed, as shown in Fig. 4.23. An interesting finding is that the resistivity under $H = 70$ kOe follows the usual Fermi liquid relation of the T^2-dependence. The present result is very similar to the non-Fermi liquid nature in $CeCoIn_5$, which is known as a heavy fermion superconductor in the quantum critical region [93]. Namely, $CeCoIn_5$ indicates a clear T^1-dependence of the resistivity and shows the negative magnetoresistance. At present it is not clear whether the resistivity decrease in $CeAgSb_2$ is due to onset of superconductivity or not.

A new finding in the present experiment of $CeAgSb_2$ is that the residual resistivity possesses a huge value in the critical pressure region: $\rho_0 = 0.3\mu\Omega$·cm at ambient pressure is changed into 55 $\mu\Omega$·cm at $P_{\rm c} = 3.3$ GPa. Recently Miyake and Maebashi explained theoretically the origin of the huge residual resistivity around the quantum critical region [94]. This theory explains a sharp peak of the residual resistivity observed in $CeCu_2Ge_2$ at $P \simeq 17$ GPa where the superconducting transition temperature also exhibits the sharp peak: $\rho_0 = 2.5\mu\Omega$·cm at ambient pressure and 39 $\mu\Omega$·cm at 17 GPa in $CeCu_2Ge_2$ [95]. The similar pressure-induced superconductor is $CeRhIn_5$: $\rho_0 = 0.2\,\mu\Omega$·cm at ambient pressure and 13.2 $\mu\Omega$·cm at 2.5 GPa in $CeRhIn_5$ [96]. The theory is based on the impurity scattering due to critical valence fluctuations of the $4f$ electron in the cerium heavy fermion system. The present enhancement of the residual resistivity in $CeAgSb_2$ is large compared to those in $CeCu_2Ge_2$ and $CeRhIn_5$.

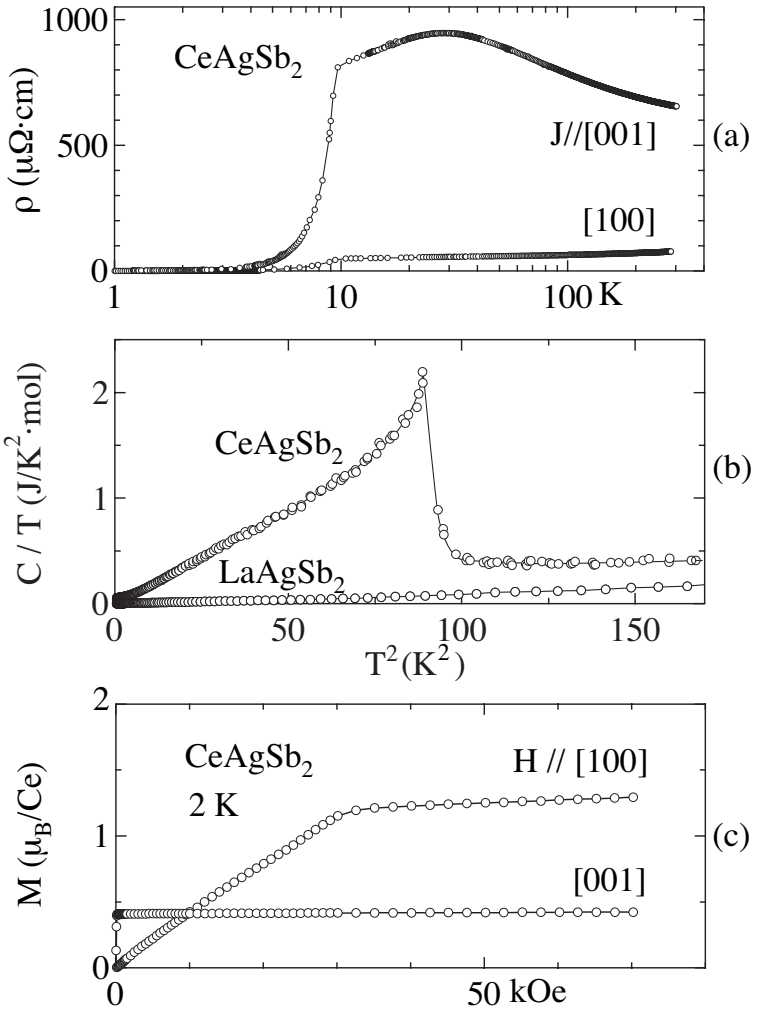

Fig. 4.18 Temperature dependence of (a) the electrical resistivity in $CeAgSb_2$, (b) the specific heat in the form of C/T in $CeAgSb_2$ and $LaAgSb_2$ and (c) the magnetization curve for $H \parallel [001]$ in $CeAgSb_2$.

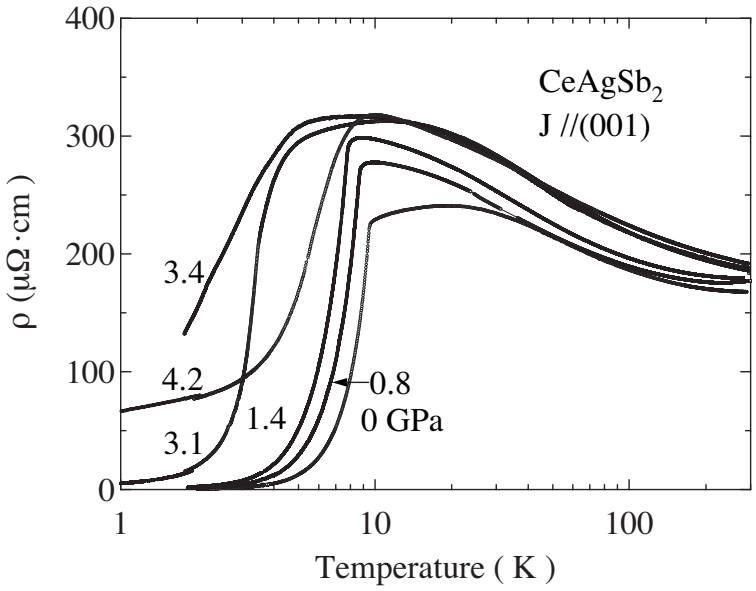

Fig. 4.19 Temperature dependence of the electrical resistivity under several pressures in $CeAgSb_2$.

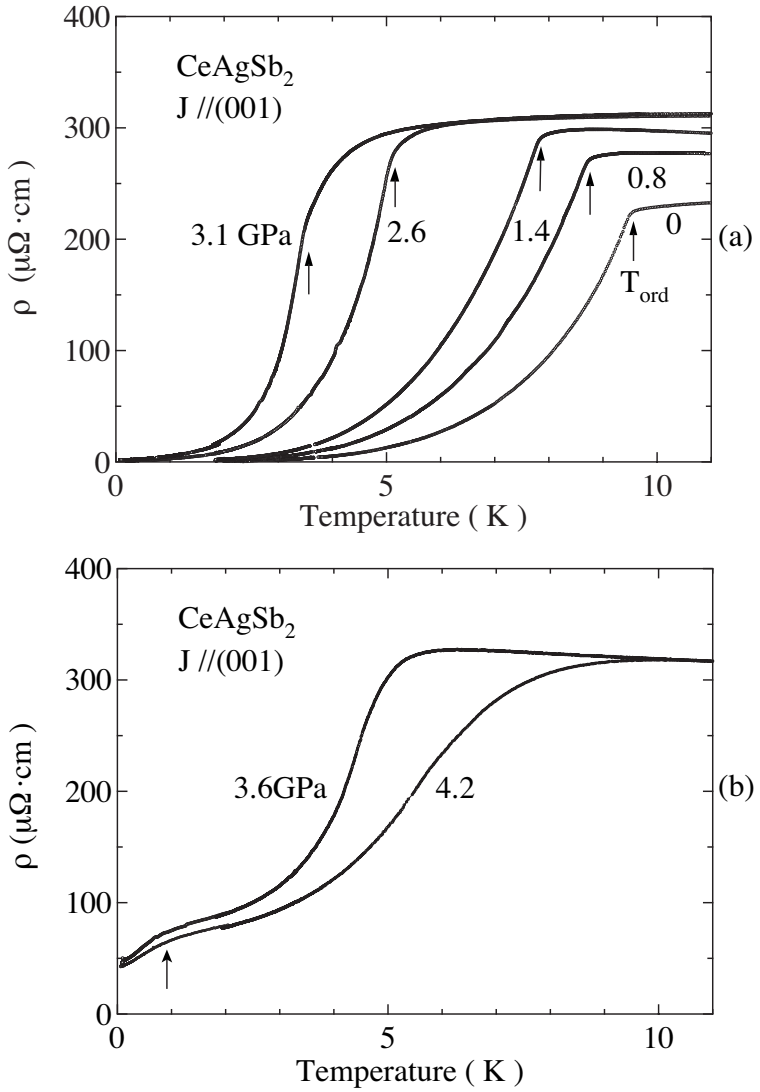

Fig. 4.20 Low-temperature electrical resistivity under several pressures (a) below and (b) above 3.3 GPa in $CeAgSb_2$.

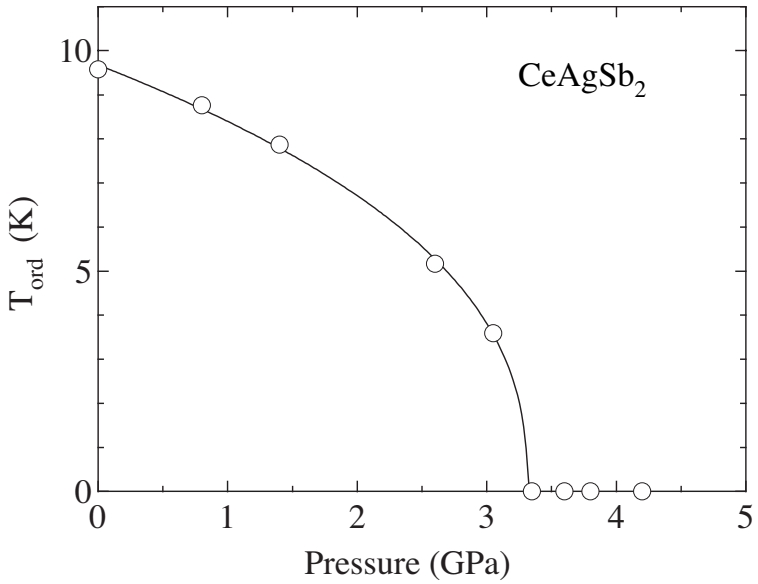

Fig. 4.21 Pressure dependence of the magnetic ordering temperature in $CeAgSb_2$. A solid line connecting the data is a guideline.

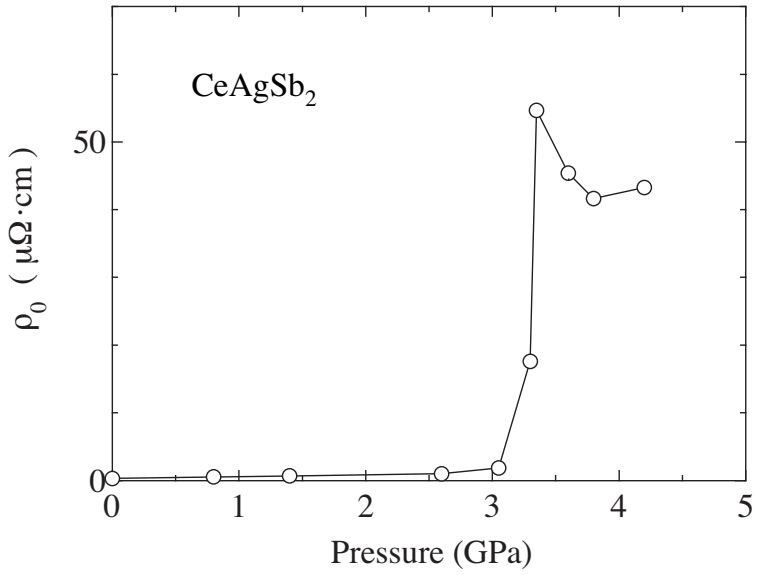

Fig. 4.22 Pressure dependence of the residual resistivity in $CeAgSb_2$.

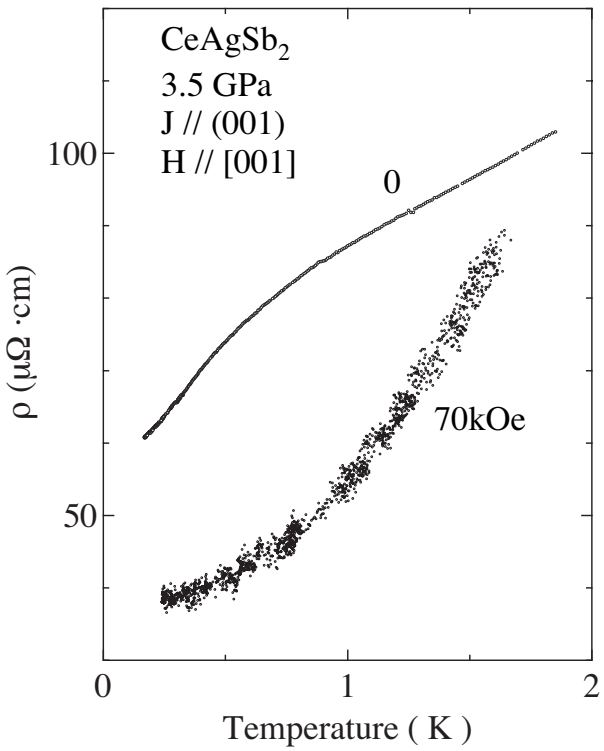

Fig. 4.23 Temperature dependence of the electrical resistivity at 3.5 GPa under the magnetic field of 0 and 70 kOe in $CeAgSb_2$.

4.2 Uranium Compounds

4.2.1 $UNiGa_5$, $UPdGa_5$, $UPtGa_5$

Figure 4.24 shows the temperature dependence of the electrical resistivity ρ under pressure for the current along the [001] direction. A sharp kink in the resistivity at T_N = 86.5 K at ambient pressure indicates the Néel temperature. T_N decreases with increaseing pressure, and the kink is not found above 4.5 GPa. Moreover, another decrease of the resistivity below about 5 K (=T^*) was found in the pressure range from 0.5 to 1.05 GPa, as shown in Fig. 4.25.

Figure 4.26 shows a T_N and T^* vs. pressure phase diagram. A critical pressure P_c is about 4.5 GPa, where T_N becomes zero. A solid line in Fig. 4.26 indicates a guideline: $T_N(P) = T_N(P=0)\left(1-\frac{P}{P_c}\right)^n$ with $T_N(P=0)$ = 89 K, P_c = 4.5 GPa and n = 0.48. T^* is nearly constant against the pressure.

We will discuss these resistivity data from a viewpoint of the Fermi liquid nature, namely following a relation of $\rho = \rho_0 + AT^2$. The $\sqrt{A}$ value correlates with a Pauli susceptibility $\chi \simeq \chi_0$ and an electronic specific heat coefficient γ. This Fermi liquid nature is found at 1.5 and 2.5 GPa below about 15 K, as shown in Fig. 4.27. From 5.0 to 5.5 GPa, the slopes of T^2-dependence become steep, or the T^2-dependence of the electrical resisivity is doubtful. With further increasing pressure, the Fermi liquid nature fully recovers and is satisfied in a wide temperature range, as seen at 7.0 and 8.5 GPa.

Figure 4.28 shows the pressure dependence of the coefficient A and the residual resistivity ρ_0. The A value indicates a maximum around 5 GPa, close to P_c . On the other hand, the residual resistivity decreases steeply from 3 GPa, and becomes constant above 6 GPa.

Recently, it was argued that superconductivity under pressure is related to both the A and ρ_0 values in some cerium compounds [97, 98, 99]. Superconductivity is found around the critical pressure P_c and/or the non-Fermi liquid nature appears around P_c, as mentioned in Chap.2. Moreover, the A and ρ_0 values also have a maximum at P_c.

In the present experiment for $UNiGa_5$, the A value has a maximum at 5 GPa, which is close to P_c = 4.5 GPa. The ρ_0 value, however, does not have a maximum at P_c. In uranium compounds, the superconductivity appears below 1 K in general. Measurements under presssure at much lower temperature are needed to confirm superconductivity, together with the non-Fermi liquid nature for $UNiGa_5$.

In conclusion, the quantum critical pressure P_c, where T_N becomes zero, was determined to be $P_c \simeq$ 4.5 GPa from the resistivity measurement under pressures up to 8.5 GPa. Around P_c, the A value has a maximum, and the Fermi liquid nature is not fully satisfied around P_c.

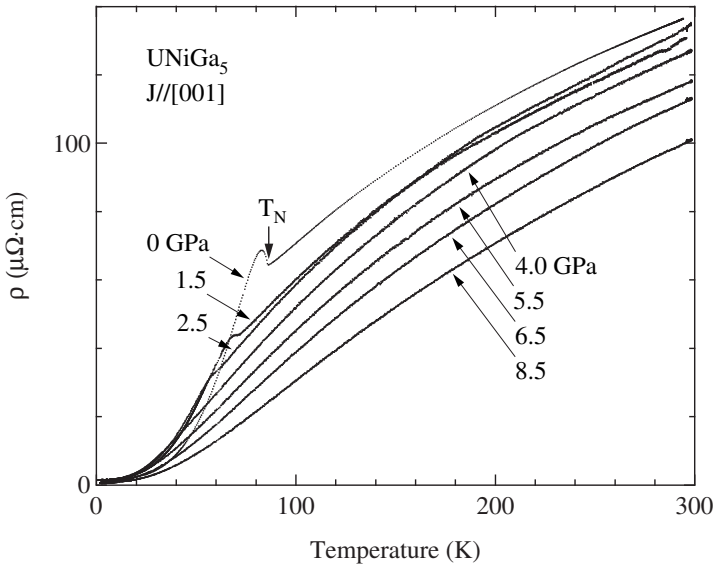

Fig. 4.24 Temperature dependence of the electrical resistivity ρ under pressure in $UNiGa_5$.

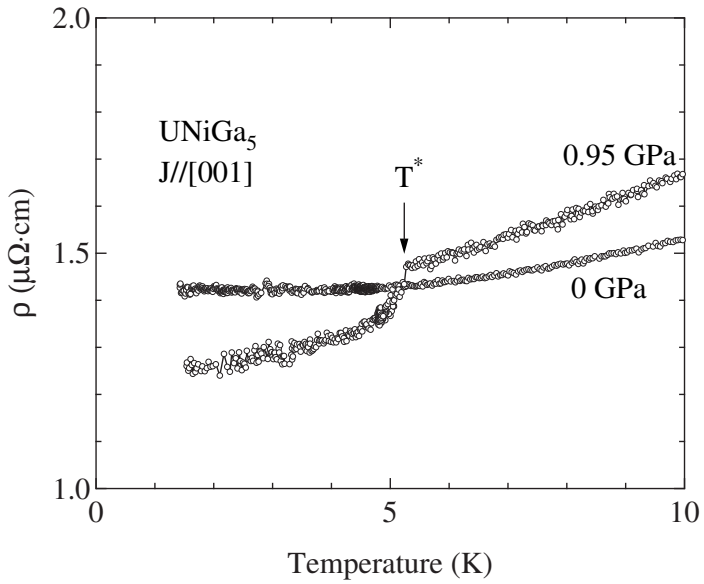

Fig. 4.25 Temperature dependence of the electrical resistivity ρ under ambient pressure and 0.95 GPa in $UNiGa_5$. Under 0.95 GPa, there is a steep decrease of the resistivity below 5.3 K.

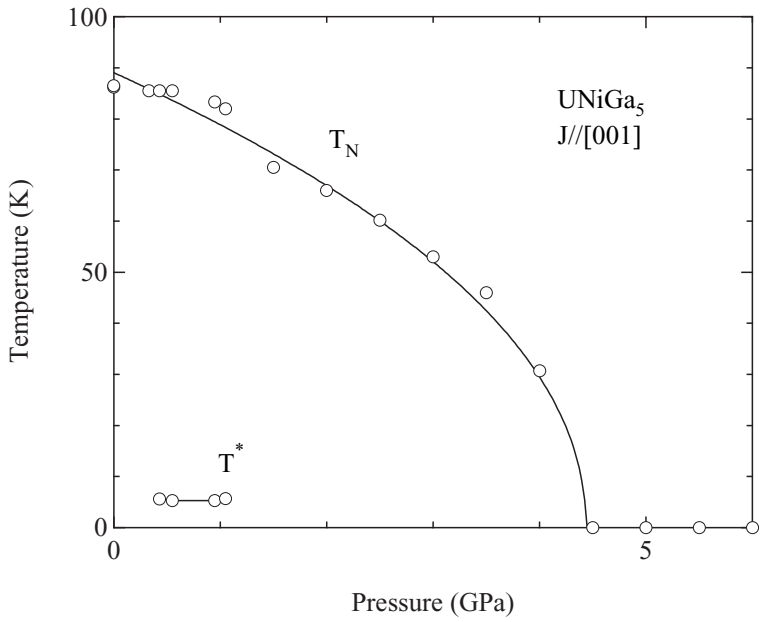

Fig. 4.26 Pressure dependence of T_{N} and T^* in $UNiGa_5$.

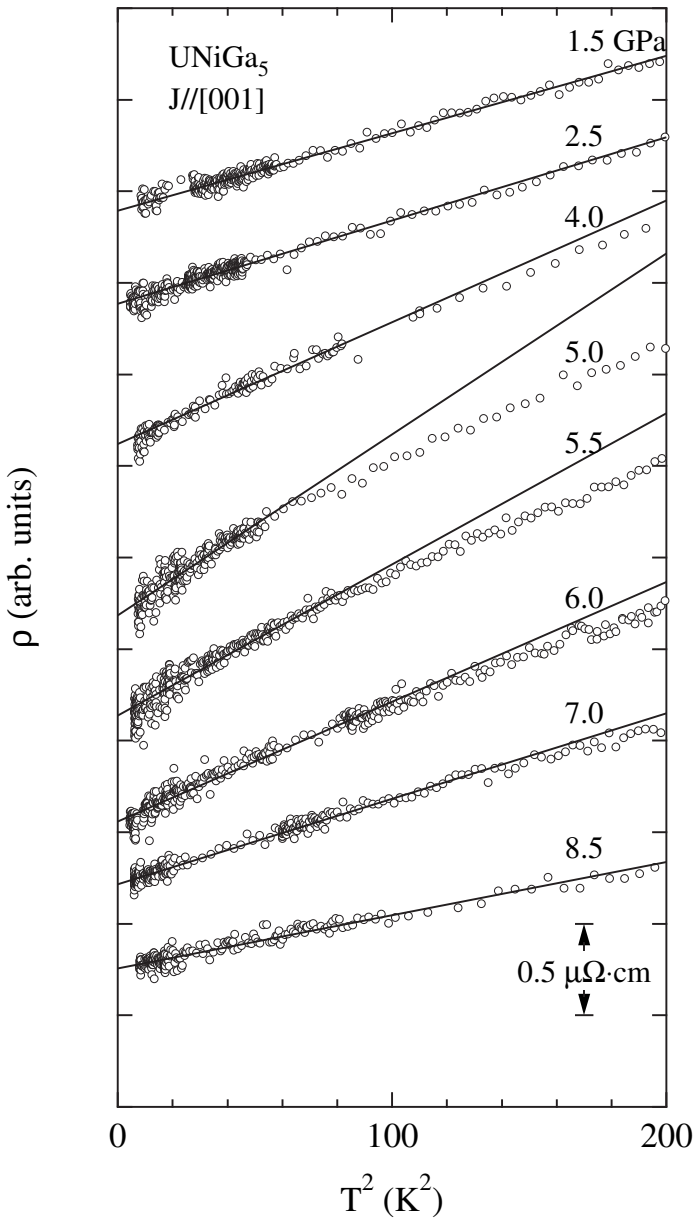

Fig. 4.27 T^2 dependence of ρ in $UNiGa_5$.

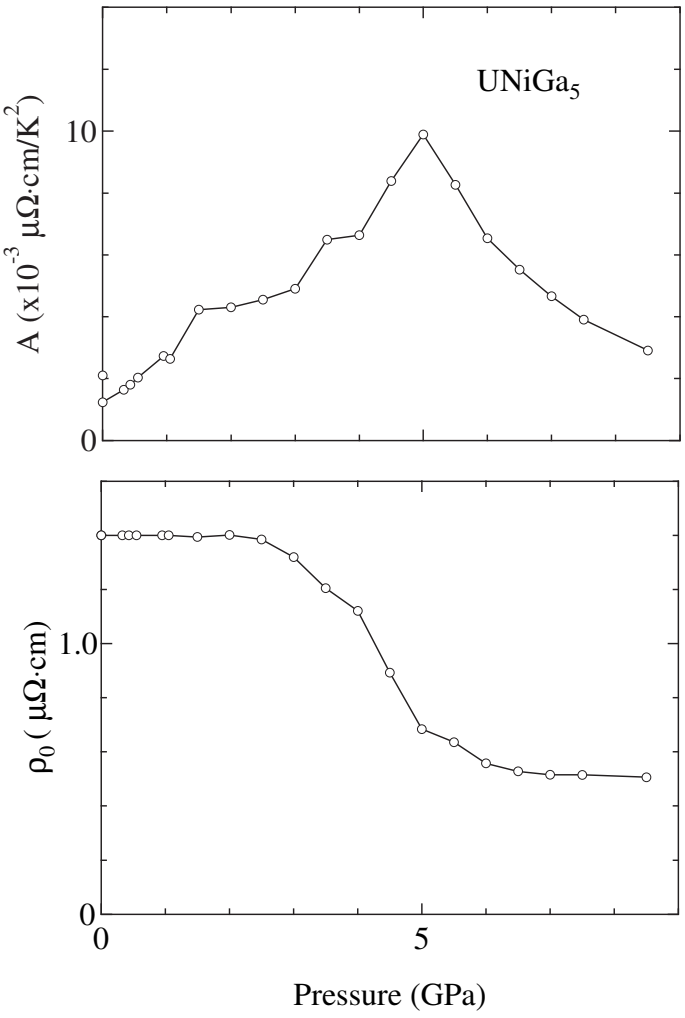

Fig. 4.28 Pressure dependence of A and ρ_0 values in $UNiGa_5$.

Figure 4.29 shows a temperature dependence of the electrical resistivity at ambient pressure and under pressures. At ambient pressure, the resistivity decreases steeply below T_N. With increasing presure, the Néel temperature decreases smoothly as shown by arrows in Fig. 4.29. We show in Fig. 4.30 the pressure dependence of the Néel temperature, where a solid line of $T_N(P) = T_N(P=0)\left(1-\frac{P}{P_c}\right)^n$ with $T_N(P=0) = 23$ K and $n = 0.35$ is a guideline. A critical pressure P_c is estimated as 3.2 GPa. We will discuss these resistivity data from a viewpoint of the Fermi liquid nature, namely following a relation of $\rho = \rho_0 + AT^2$. From 3.2 to 4.0 GPa, the slopes of T^2-dependence become steep, or the T^2-dependence of the electrical resisivity is doubtful. With further increasing pressure, the Fermi liquid nature fully recovers and is satisfied in a wide temperature range, as seen at 5.0 GPa.

These characteristic features are the same as those of $UNiGa_5$.

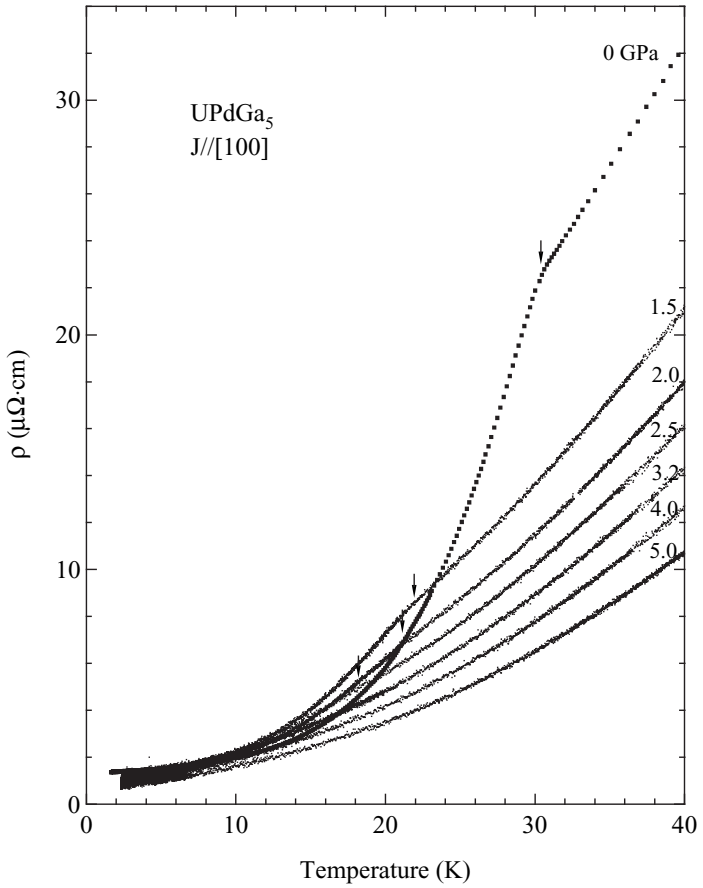

Fig. 4.29 Temperature dependence of the electrical resistivity ρ under pressure in $UPtGa_5$.

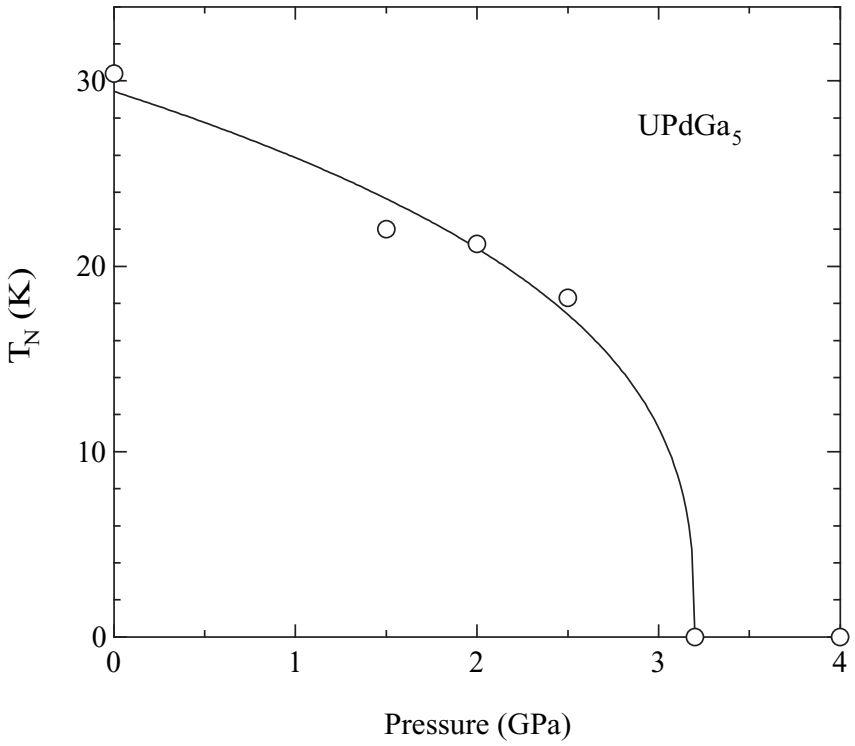

Fig. 4.30 Pressure dependence of T_{N} $UPdGa_5$.

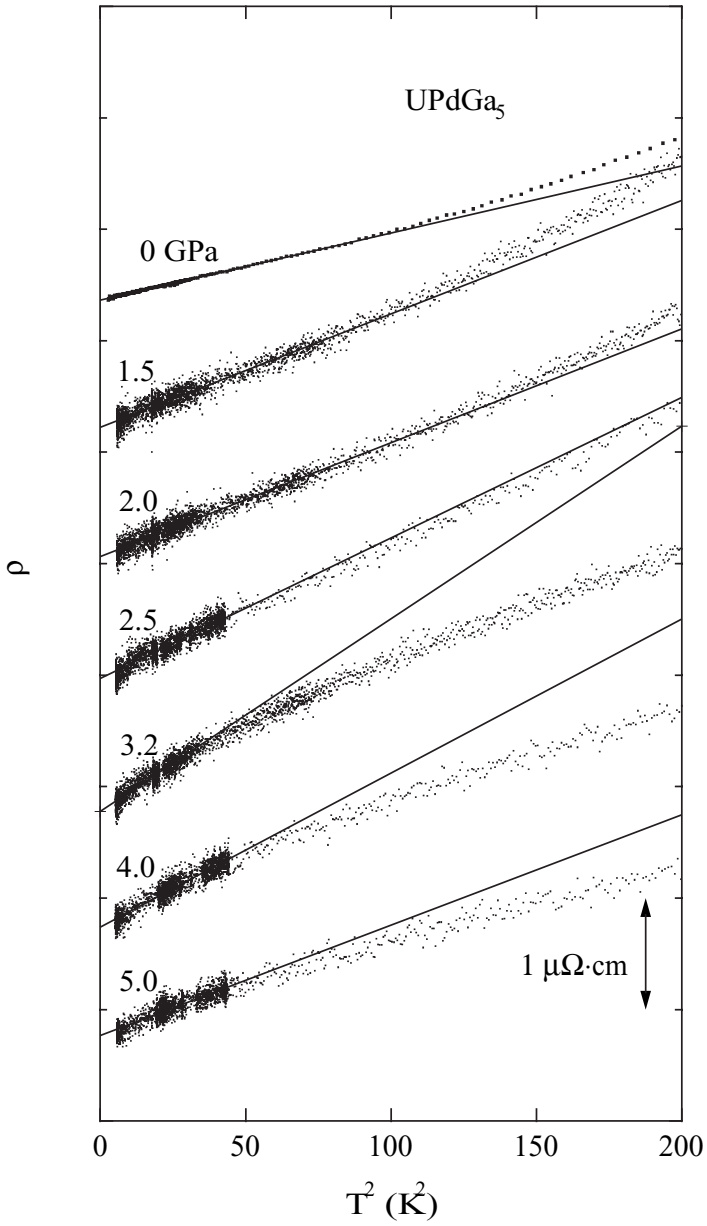

Fig. 4.31 T^2 dependence of ρ in $UPdGa_5$.

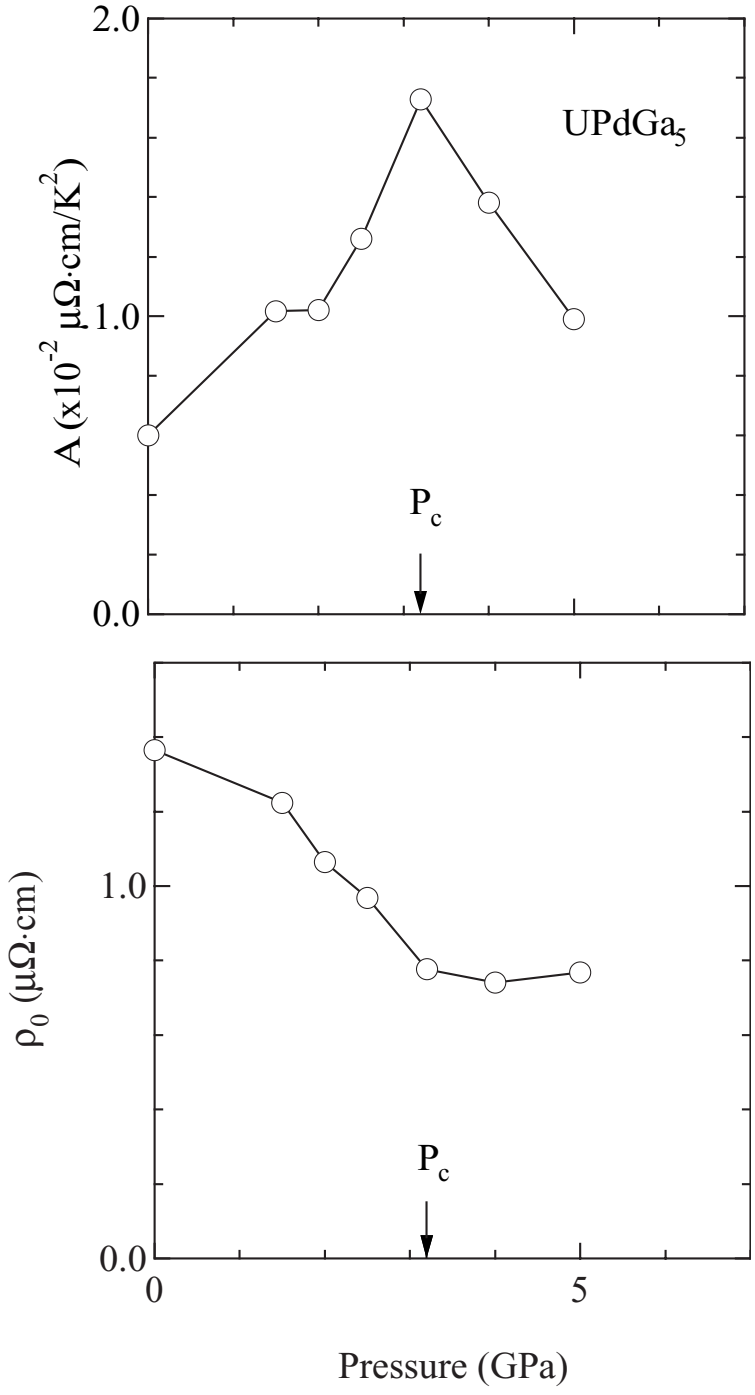

Fig. 4.32 Pressure dependence of A and ρ_0 values in $UPdGa_5$.

Figure 4.33 shows a temperature dependence of the electrical resistivity at ambient pressure and under pressures in $UPtGa_5$. At ambient pressure, the resistivity decreases steeply below T_N. With increasing presure, the Néel temperature decreases smoothly as shown by arrows in Fig. 4.33. We show in Fig. 4.34 the pressure dependence of the Néel temperature, where a solid line of $T_N(P) = T_N(P=0)\left(1-\frac{P}{P_c}\right)^n$ with $T_N(P=0) = 23$ K and $n = 0.53$ is a guideline. A critical pressure P_c is estimated as 8 GPa. Here we note that the low temperature resisvitity follows a Fermi liquid relation of $\rho = \rho_0 + AT^2$ below 5 K. The A and ρ_0 values are approximately unchanged against pressure. We determined a critical pressure P_c as 8.0 GPa in $UPtGa_5$. The low-temperature resisvitity follows the Fermi liquid relation, but the relation of the A and ρ_0 values vs. pressure is not simple. The A and ρ_0 values are unchanged against pressure in $UPtGa_5$, as shown in Fig. 4.35

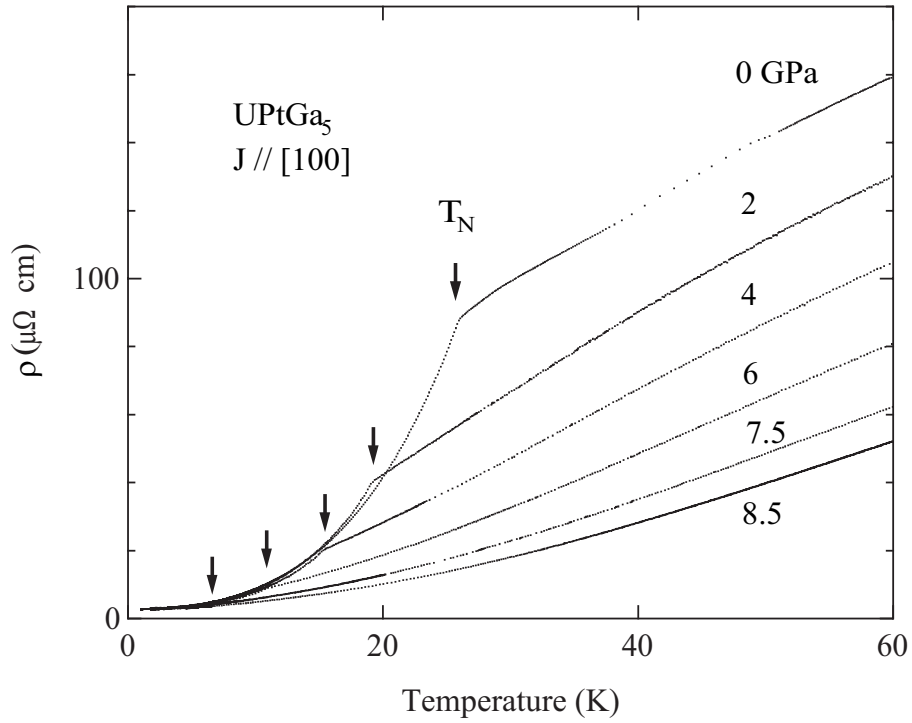

Fig. 4.33 Temperature dependence of the electrical resistivity ρ under pressure in $UPtGa_5$.

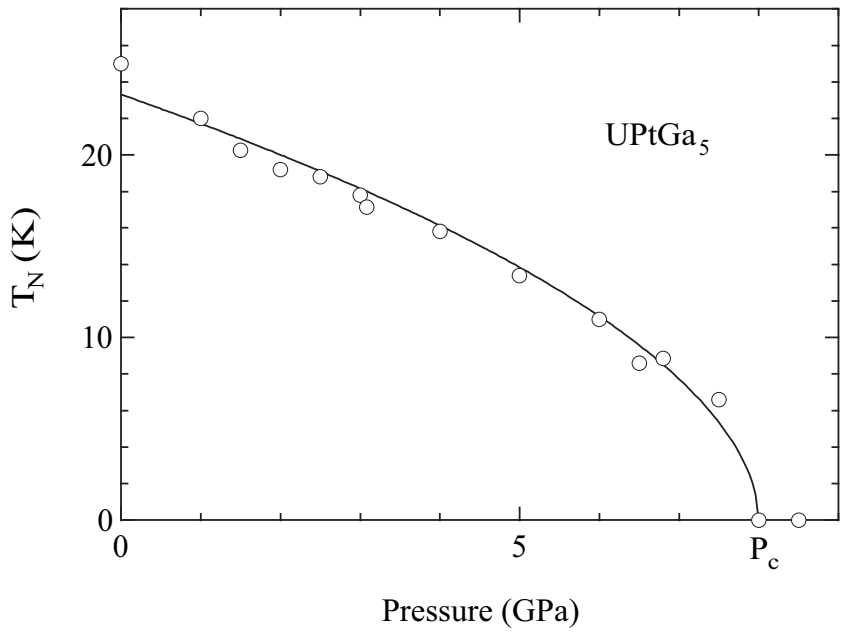

Fig. 4.34 Pressure dependence of $T_{\rm N}$ in $UPtGa_5$.

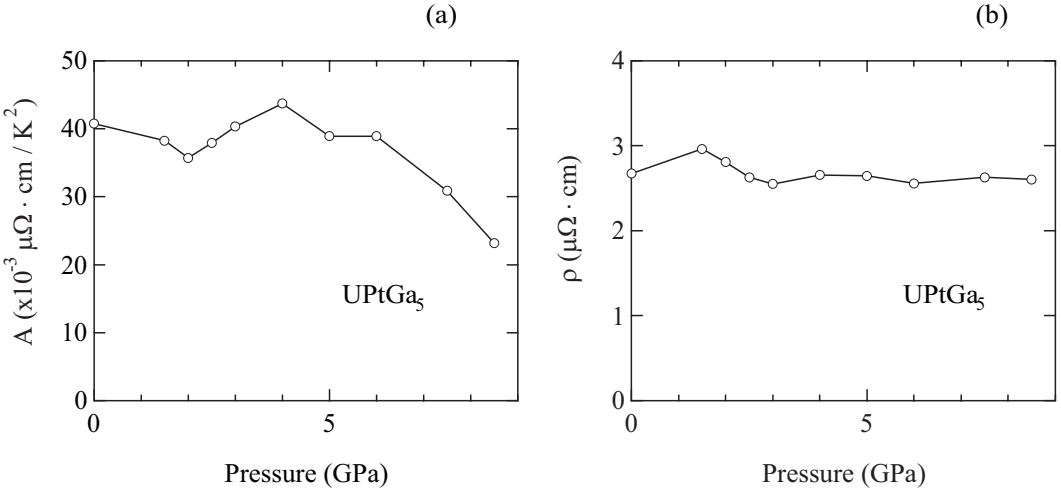

Fig. 4.35 Pressure dependence of A and ρ_0 values in $UPtGa_5$.

4.2.2 UN

We measured the resistivity of UN under pressure, as shown in Fig. 4.36. At ambient pressure, a small but sharp hump is observed at $T_N = 53$ K. With applying pressure, the hump becomes broad but can be observed up to 3 GPa. Figure 4.37 shows the pressure dependence of the Néel temperature, where a solid line of $T_N(P) = T_N(P=0)\left(1 - \frac{P}{P_c}\right)^n$ with $T_N(P=0) = 50$ K and $n = 0.65$ is a guideline. A critical pressure P_c is estimated as 3.5 GPa. The resisvivity follows the Fermi liquid relation of $\rho = \rho_0 + AT^2$ below 7 K. Figure 4.38 shows the pressure dependence of A and ρ_0 values. The A value has a maximum at 2 GPa, while the ρ_0 value decreases steeply below about 2 GPa.

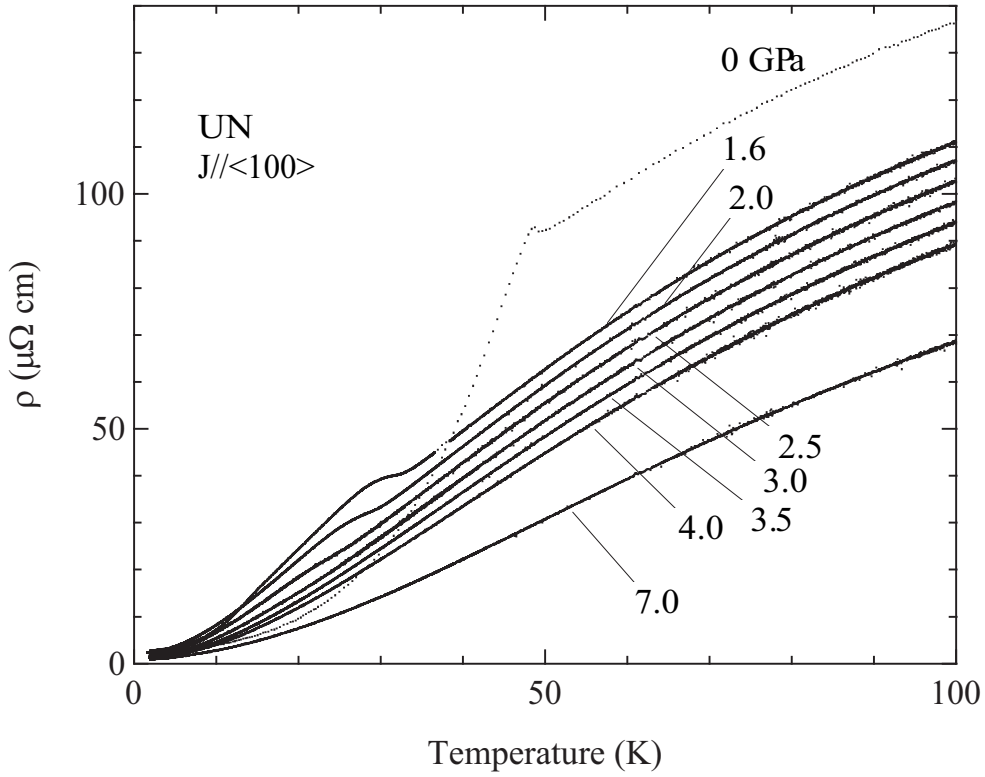

Fig. 4.36 Temperature dependence of the electrical resistivity ρ under pressure in UN.

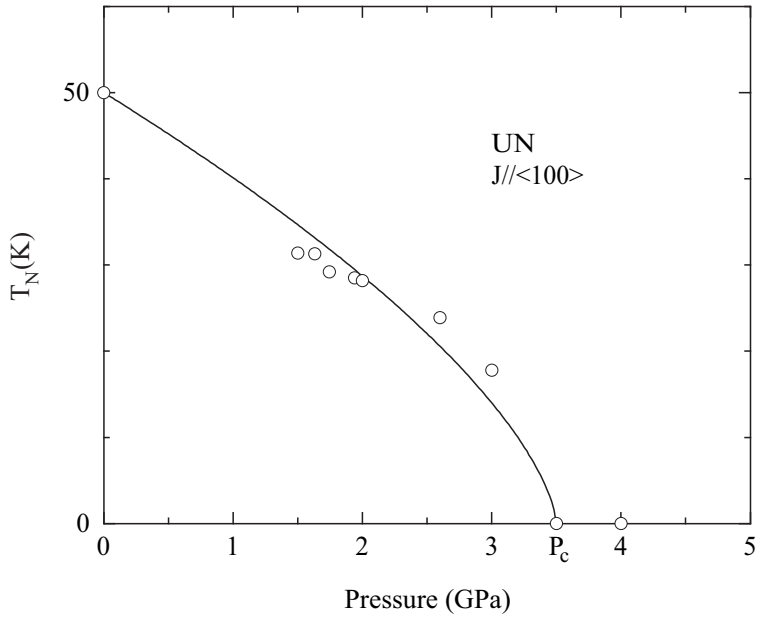

Fig. 4.37 Pressure dependence of T_{N} in UN.

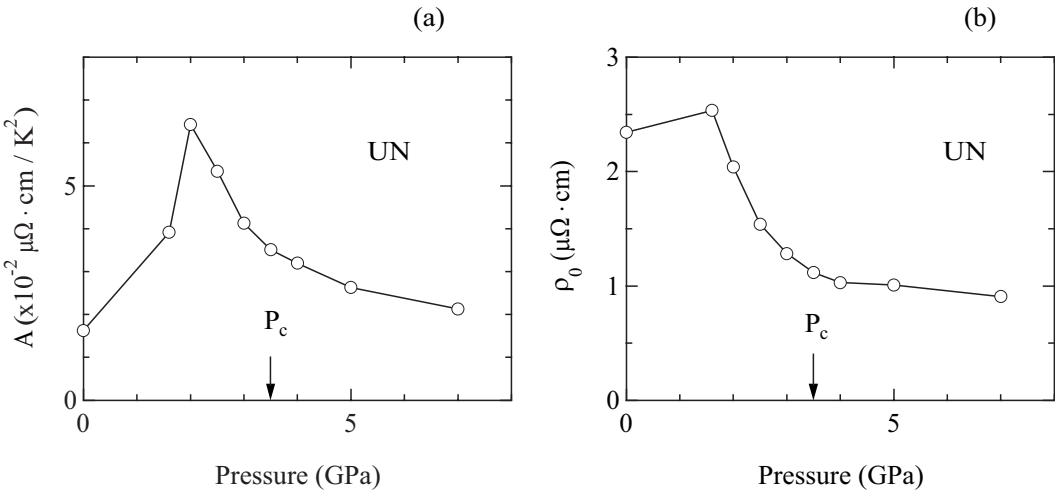

Fig. 4.38 Pressure dependence of A and ρ_0 values in UN.

4.2.3 UGa_3

In the present study the pressure was applied to the sample of UGa_3 up to 8.5 GPa . The Néel temperature $T_N = 67$ K was observed to disappear above 2.5 GPa. In this pressure region we found the non-Fermi liquid nature, not following a T^2-dependence of the electrical resistivity but indicating a linear T-dependence of the resistivity.

Single crystals of UGa_3 was grown by the so-called self-flux methods. Ga was used as flux. The residual resistivity ratio ρ_{RT}/ρ_0 was about 80. See ref. [72] in details. Pressure up to 8.5 GPa was applied by a cubic anvil apparatus in the temperature region from 2 K to 300 K and by a Bridgman anvil apparatus at lower temperatures down to 80 mK. We used two different samples for two corresponding measuring systems.

Figure 4.39 shows the temperature dependence of the $d\rho/dT$ curve under pressure. In an inset we show the temperature dependence of the electrical resistivity ρ at ambient pressure, namely 0 GPa. A small hump in the resistivity at $T_N = 67$ K in the inset of Fig. 4.39 corresponds to a Néel temperature. At 3 GPa, a signature for the antiferromagnetic ordering is not detected. corresponds to a Néel temperature. The Néel temperature is found to decrease steeply with increasing pressure, as shown by arrows in Fig. 4.39. Figure 4.40 shows a T_N vs pressure phase diagram. A critical pressure P_c is about 2.6 GPa, where T_N becomes zero. A solid line in Figure 4.40 indicates a guideline: $T_N(P) = T_N(P = 0)\left(1 - \left(\frac{P}{P_c}\right)^n\right)$ with $T_N(P = 0) = 65.4$ K, $P_c = 2.6$ GPa and $n = 0.45$.

The electrical risistivity at ambient pressure in UGa_3 is known to follow a T^2 - dependence of the electrical resistivity below about 20 K [72]. Namely, the electrical resistivity ρ follows a Fermi liquid nature of $\rho = \rho_0 + AT^2$. The $\sqrt{A}$ value correlates with a Pauli susceptibility $\chi \simeq \chi_0$ and a constant γ-value. This Fermi liquid nature is found at 2.0 GPa below about 15K, as shown in Fig. 4.41. At 2.5 and 3.0 GPa, the T^2-dependence of the electrical resisivity is doubtful because a slope in the ρ vs T^2 curve is changed with decreasing the temperature. With further increasing pressure, it fully recovers and is satisfied in a wide temperature range, as seen at 5.0 and 6.0 GPa.

Figure 4.42 shows the pressure dependence of the coefficient A and the residual resistivity ρ_0. The A value suggests a maximum around $P_c = 2.6$ GPa, although the residual resistivity does not follow the same pressure dependence, having a maximum atabout 1.5 GPa.

We measured the electrical resistivity at lower temperatures under pressure ranging from 1.5 to 3.1 GPa. Figure 4.43 shows the temperature dependence of the resistivity under pressure. A linear T-dependence is found: $\rho = \rho_0 + A'T$ below 1.6 K at 2.5 GPa and below 2.0 K at 2.8 GPa, which are compared to the resistivity data under 1.8 and 3.1 GPa. It is clear that the Fermi liquid nature is broken around $P_c = 2.6$ GPa.

Finally, we measured the transverse magnetoresistance $\Delta\rho/\rho = \{\rho(H) - \rho(H = 0)\}/\rho(H = 0)$ at 4.2K, where the current and magnetic field were applied along the [100] and [001] directions, respectively. The magnetoresistance increases as a function of $\Delta\rho/\rho \sim H^n (n > 1)$. This is consistent with the previous result indicating a compensated metal with closed Fermi surfaces [72]. The value of $\Delta\rho/\rho$ decreases with increasing pressure. This means that the mobilities of electrons and holes, μ_e and μ_h, decrease

with increasing pressure because $\Delta\rho/\rho \simeq \mu_e\mu_h H^2$ at high fields. In other words, the cyclotron effective mass, which is inversely properties to the mobility, increases with increasing pressure. The decrease of $\Delta\rho/\rho$ thus corresponds to the increase of the A value in Fig. 4.42(a).

We will discuss the non-Fermi nature in UGa_3 around the magnetic quantum critical region. Namely, the electrical resistivity indicates a T^n $(n = 1)$-dependence at low temperatures around $P_c = 2.6$ GPa.

The non-Fermi liquid nature has been discussed as a diverging linear coefficient of the specific heat C for temperatures $T \to 0 : \gamma = C/T = -\log(T/T_0)$ and a strong temperature dependence of the magnetic susceptibility χ as $T \to 0$. Furthermore, the electrical resistivity ρ deviates from the T^2-dependence, indicating a linear T-dependence, for example ref. [100].

Experimentally a non-Fermi liquid relation was observed in several compounds: a quasi-linear resistivity of $\rho \propto T^{1.2}$ from a superconducting transition temperature $T_c \simeq 0.4$ K to high temperatures up to 40 K under $P = 3.05$ GPa in $CePd_2Si_2$ [97] and a linear T-dependence of $\rho \propto T$ from $T_c \simeq 2$ K to 15 K under $P = 15.6$ GPa in $CeCu_2Ge_2$ [98]. Not by pressure but by chemical pressure of alloying in $CeCu_{2.9}Au_{0.1}$, a linear T-dependence of the resistivity was also observed in the temperature region from 0.3-0.4 K to the lowest measured temperature of 15 mK [101].

One of the theories for non-Fermi liquid around the magnetic quantum critical point is based on the self-consistent renormalization (SCR) theory, taking into account the effect of couplings among the spin fluctuation modes (mode-mode coupling) [102, 103, 104]. This does not, however, explain the linear T-dependence of the resistivity for three-demensional magnetic systems. The linear temperature dependence of the resistivity is still an open question.

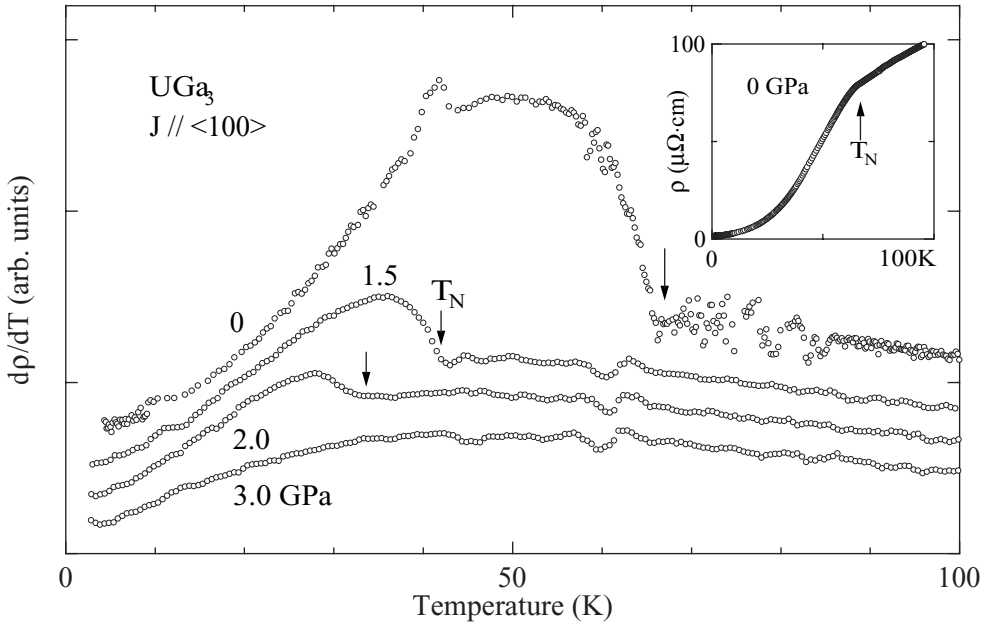

Fig. 4.39 Temperature dependence of $d\rho/dT$ under pressure in UGa_3. The inset shows low-temperature resistivity.

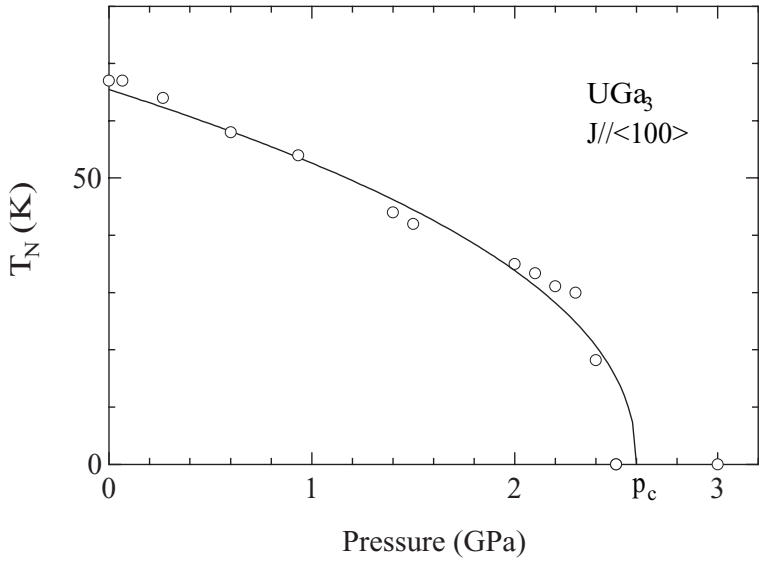

Fig. 4.40 T_N vs pressure phase diagram in UGa_3.

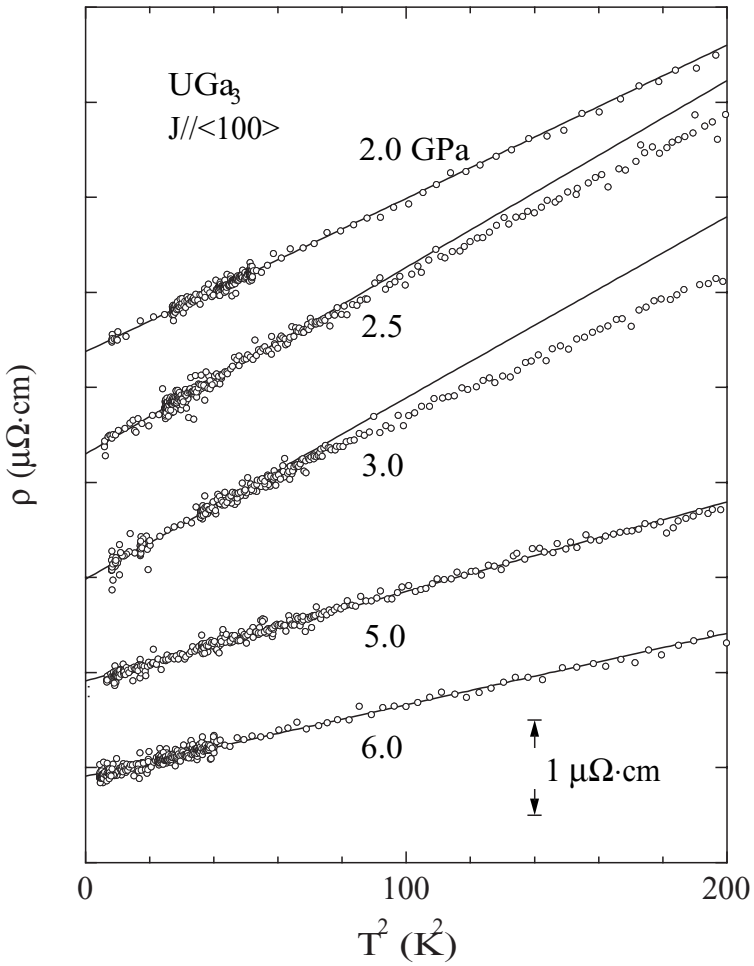

Fig. 4.41 T^2-dependence of the electrical resistivity under pressure in UGa_3.

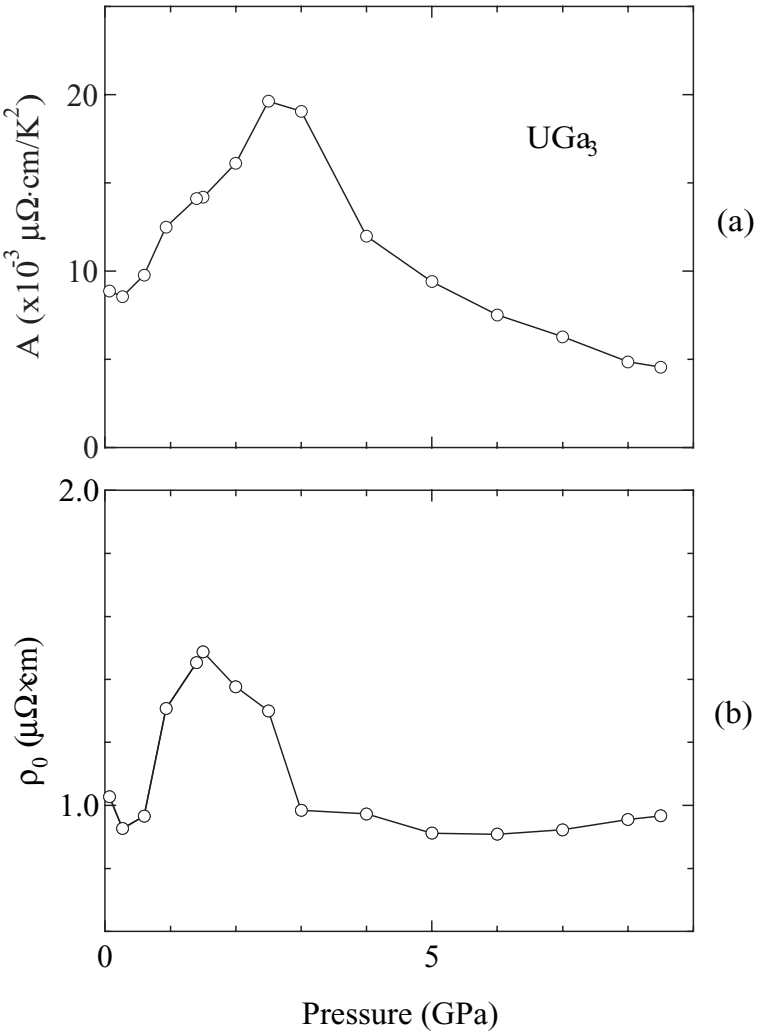

Fig. 4.42 Pressure dependence of A and ρ_0 values in UGa_3.

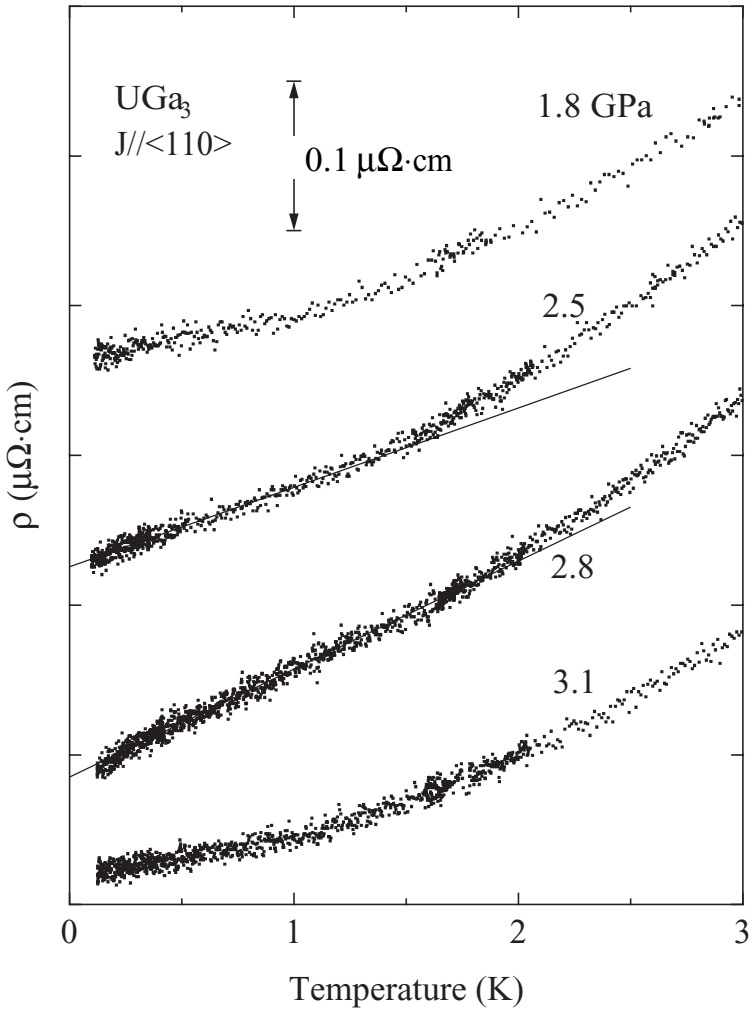

Fig. 4.43 Temperature dependence of the electrical resistivity under pressure in UGa_3.

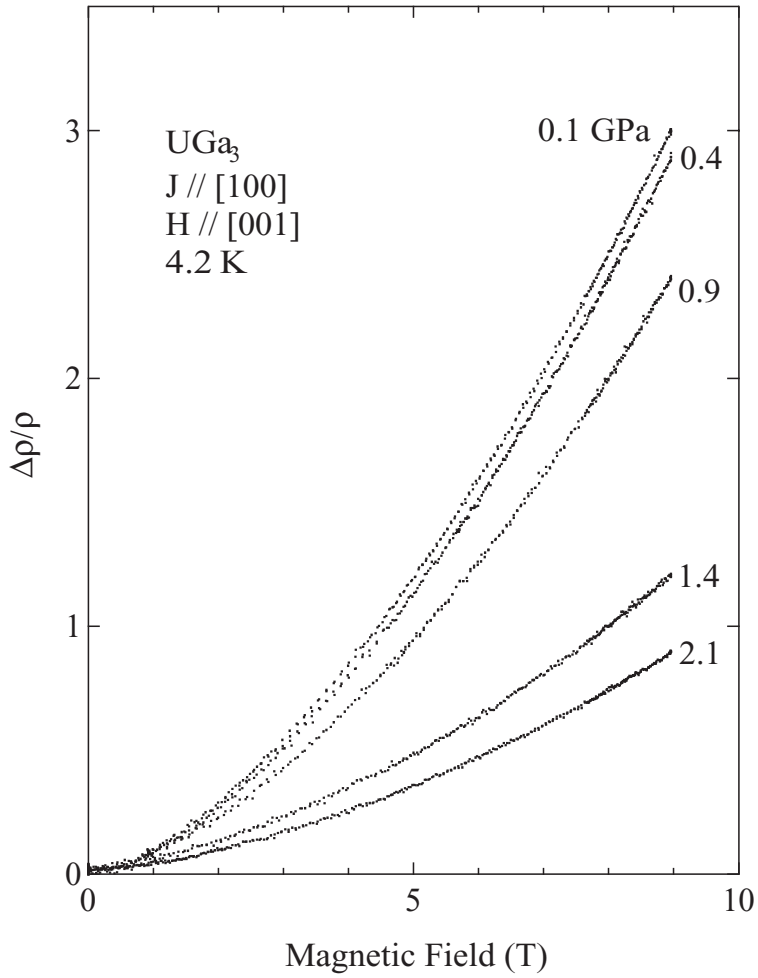

Fig. 4.44 Transverse magnetoresistance under pressure in UGa_3.

4.2.4 URu_2Si_2, UPt_3

(a)dHvA effect Under pressure in URu_2Si_2

The de Haas-van Alphen (dHvA) effect is the most powerful method to determine the topology of the Fermi surface, cyclotron effective mass and the Dingle temperature. Previously we studied the dHvA effect of URu_2Si_2 [74]. If the recent NMR experiment is right, the detected dHvA branch is mainly due to the paramagnetic region because the volume fractions of the paramagnetic and antiferromagnetic regions are about 99 and 1%, respectively, from the tiny moment of $0.03\mu_B$. The topology of the Fermi surface is generally influenced by the antiferromagnetic ordering. At 0.5 GPa we expect two kinds of dHvA branches based on the paramagnetic and antiferromagnetic regions. To clarify it we carried out dHvA experiment under pressure.

Figures 4.45, 4.46 show the dHvA oscillation in the field along [100] at 0.5 GPa (a) and [001] at 0.7 GPa (b) under pressure, and the corresponding fast Fourier transform (FFT) spectra, together with FFT spectra at different pressures. Detected dHvA branches are a branch named α and its higher harmonics, where the branch α is observed at ambient pressure and is known to be nearly spherical in shape. The fundamental branch is thus only one, unchanged against pressure. As shown in Fig. 4.47, the dHvA frequency for both field directions increases monotonously with increasing pressure and indicates no abrupt change at $P_c = 1.5$ GPa.

Figure 4.48 shows the pressure dependence of the cyclotron mass m_c^*. The cyclotron mass decreases considerably with increasing pressure. In the heavy fermion system, the magnetic specific heat of $5f$ electrons is partially changed into an electronic specific heat. The present result is consistent with the pressure dependence of the magnetic moment. Namely, the larger the magnetic moment is, the smaller the electronic specific heat coefficient or the cyclotron mass is. It is, however, noted that an abrupt change of the cyclotron mass at P_c is not observed within an experimental error, together with no abrupt change of the dHvA frequency mentioned above.

We also determined the Dingle temperature and estimated the mean free path for branch α for the field along [100]. The mean free path is 1100 Å ($\pm$ 50 Å), approximately independent on the pressure.

It is concluded from the present dHvA experiment that the dHvA frequency is unchanged against pressure, with a slight increase, while the cyclotron mass under pressure changes considerably, reflecting a change of the magnetic moment. The present dHvA experiment under pressure is thus inconsistent with the phase-separated proposal based on the NMR experiment, although there is a possibility that the Fermi surface is approximately the same between paramagnetic and antiferromagnetic regions.

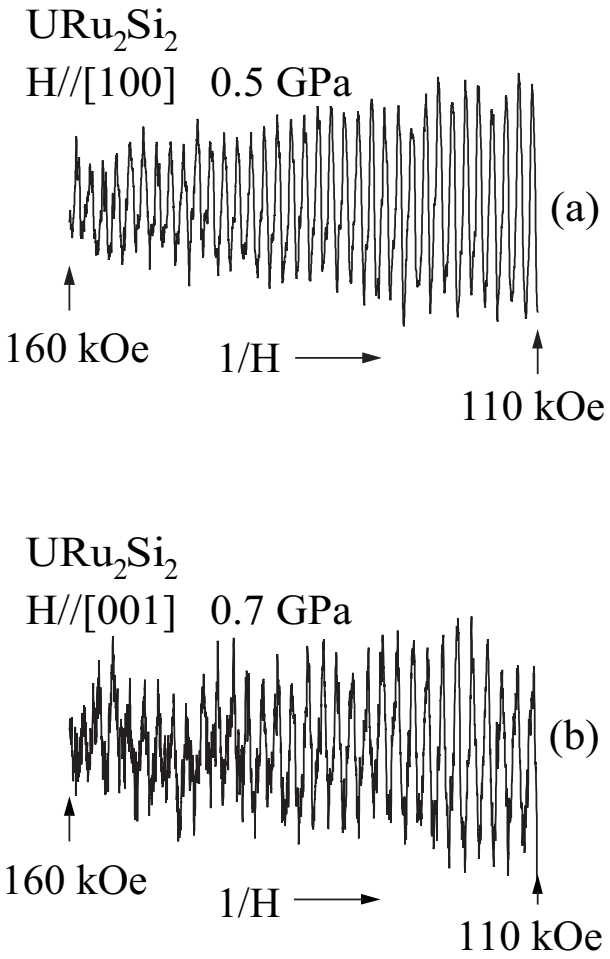

Fig. 4.45 (a) the dHvA oscillation in the field along [100] at 0.5 GPa, (b) along [001] at 0.7 GPa.

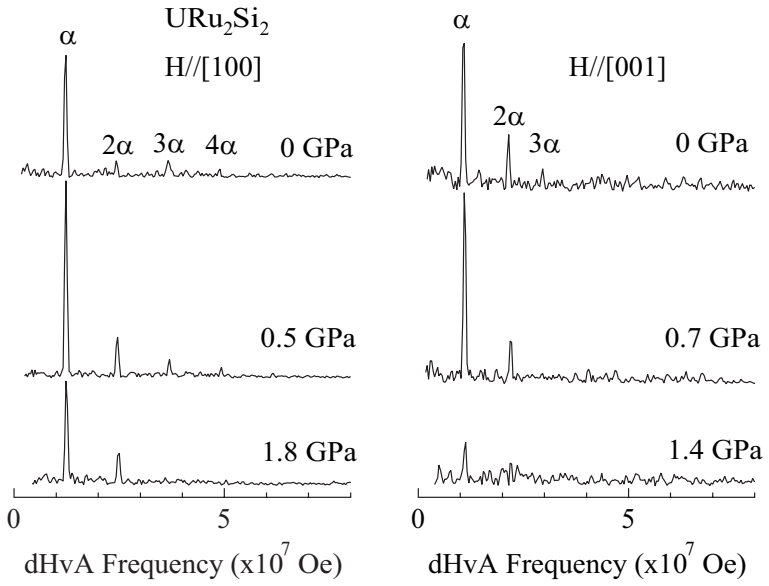

Fig. 4.46 (a) the FFT spectra of dHvA oscillation in the field along [100] at 0, 0.5, 1.8 GPa (b) along [001] at 0, 0.7 and 1.4 GPa.

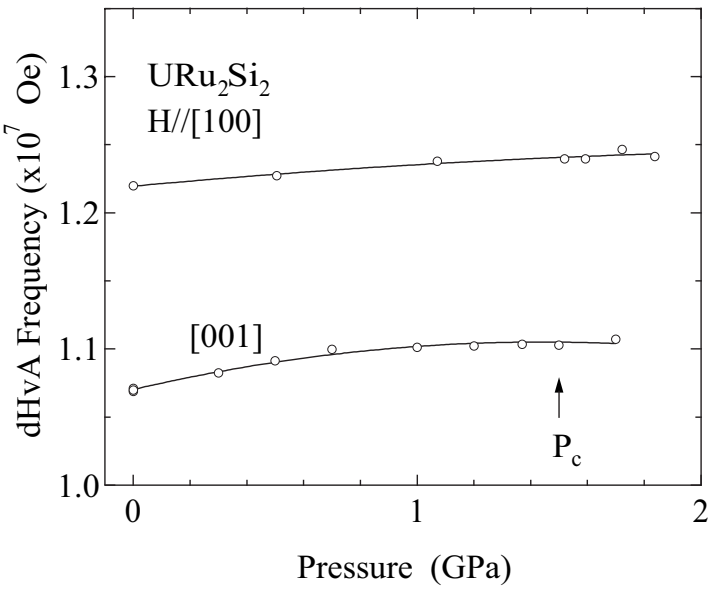

Fig. 4.47 Pressure dependence of the dHvA frequency for branch α in URu_2Si_2.

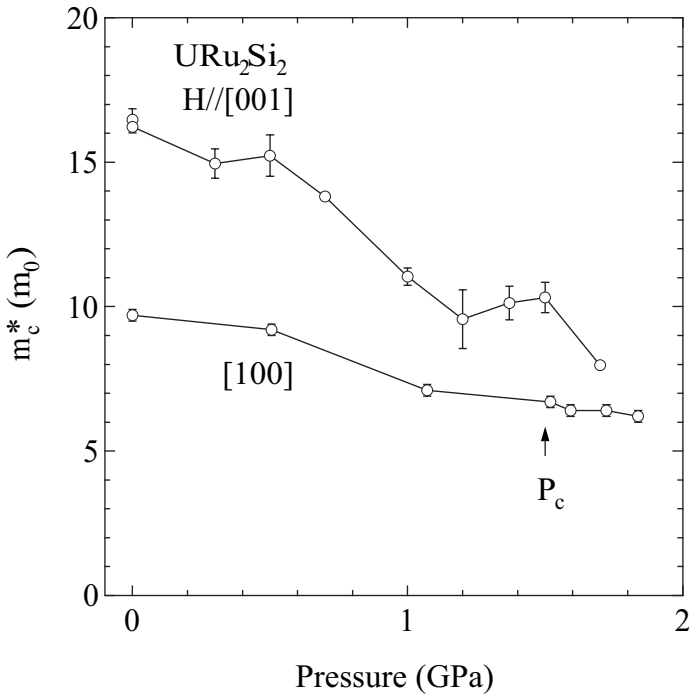

Fig. 4.48 Pressure dependence of the cyclotron mass for branch α in URu_2Si_2.

(b) Magnetization of URu_2Si_2 and UPt_3 in high magnetic fields

We have studied the high-field magnetization transition of URu_2Si_2 in a wide temperature range from 1.3 to 77 K. Figure 4.49 shows the typical magnetization curves at 1.3 K, 30 K and 77 K. At 1.3 K, the lowest measured temperature, the magnetization increases linearly and shows a three-step metamagnetic transition from 35 to 40 T. After the transitions, the magnetization curve becomes linear above 40T. The metamagnetic transition becomes broad at 30 K. It is interesting that the metamagnetic transition was observed at 30 K, namely, above T_N. The metamagnetic transition was, however, not observed at 77 K.

We show again the precise metamagnetic transition in Fig. 4.50, expanding it around the transition field. To clarify the metamagnetic transition, we show the the differential magnetization (dM/dH) curves at each temperature in Fig. 4.51. The metamagnetic transition can be defined as the peak of the dM/dH curve. The sharp three peaks corresponding to the metamagnetic transitions were observed from 1.3 K to 14 K. Above 14 K, the three peaks were change into two peaks, which were observed up to 16 K. Above $T_N = 17$ K, the metamagnetic transition is changed into one broad peak, which was observed up to 60 K. The temperature of 60 K is just above the characteristic temperature $T_{\chi max}$ (=55 K), where the magnetic susceptibility has a maximum in the temperature dependence.

In order to shed more light on the $5f$-electronic state, we replot the temperature dependence of the magnetization in the temperature range from 1.3 to 77 K under several constant magnetic fields, as shown in Fig. 4.53. The characteristic features are highly different between the high-field and low-field magnetization. The magnetization at the high field of 50 T increases monotonously with decreasing temperature, while the magnetization below 35 T shows a maximum and decreases with decreasing temperature.

We note the high-field magnetization at 50 T. The inverse susceptibility χ^{-1} ($= H/M$), where M is the magnetization at $H = 50$ T, is connected continuously with the usual inverse susceptibility obtained at 2 T, as shown in Fig. 4.54. These data follow the same Curie-Weiss law, indicating that the high-field state is approximately identical with the high-temperature $5f$-localized state. Usually the $5f$ electrons have dual nature with localized and itinerant. It is noted that the $5f$electrons are almost localized at uranium sites at high temperatures.

These susceptibility and magnetization data are approximately explained on the basis of the CEF-model of the localized $5f^2$ or $5f^3$ configurations with the doublet ground state. The characteristic temperature $T_{\chi max}$ in the magnetic susceptibility indicates the crossover from the localized $5f$-electronic state to the itinerant $5f$-electronic state with a large mass. Furthermore, the metamagnetic transition, which occurs below $T_{\chi max}$, is a change of the $5f$-electronic state from itinerant to localized.

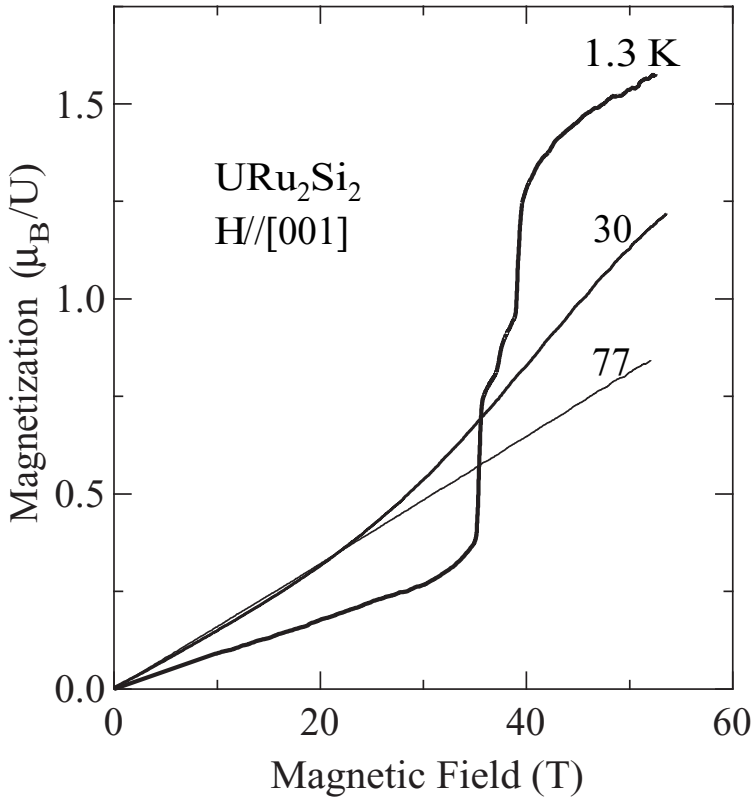

Fig. 4.49 Magnetization curves of URu_2Si_2 at 1.3, 30 and 77K.

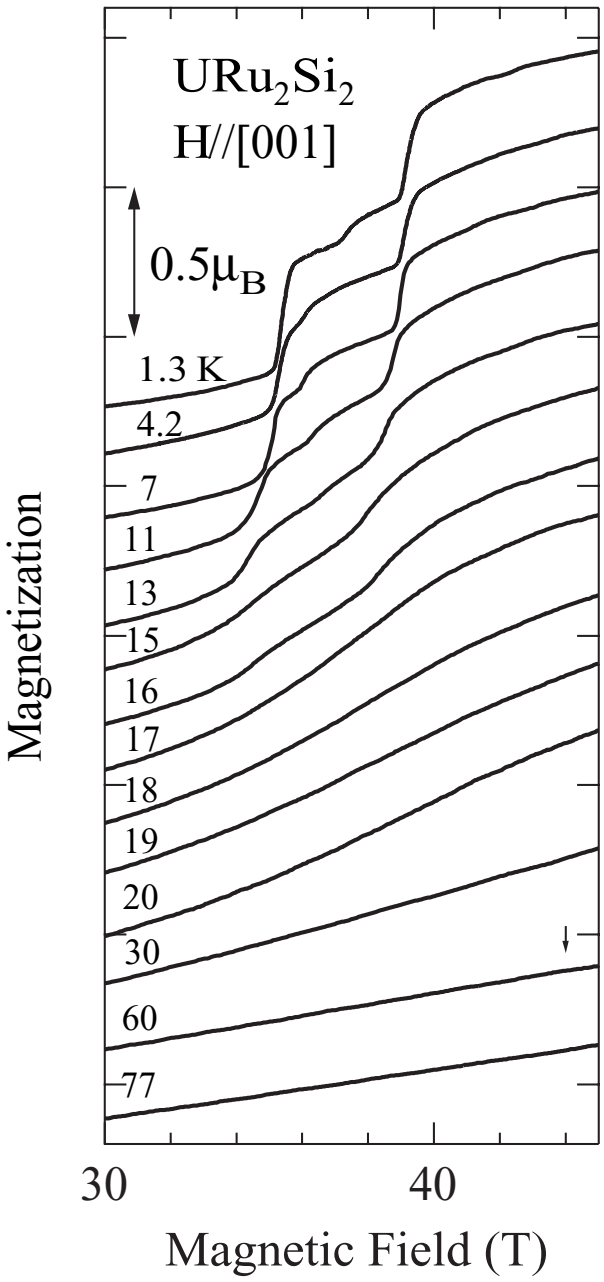

Fig. 4.50 Magnetization curves of URu_2Si_2, ranging from 30 to 44 T.

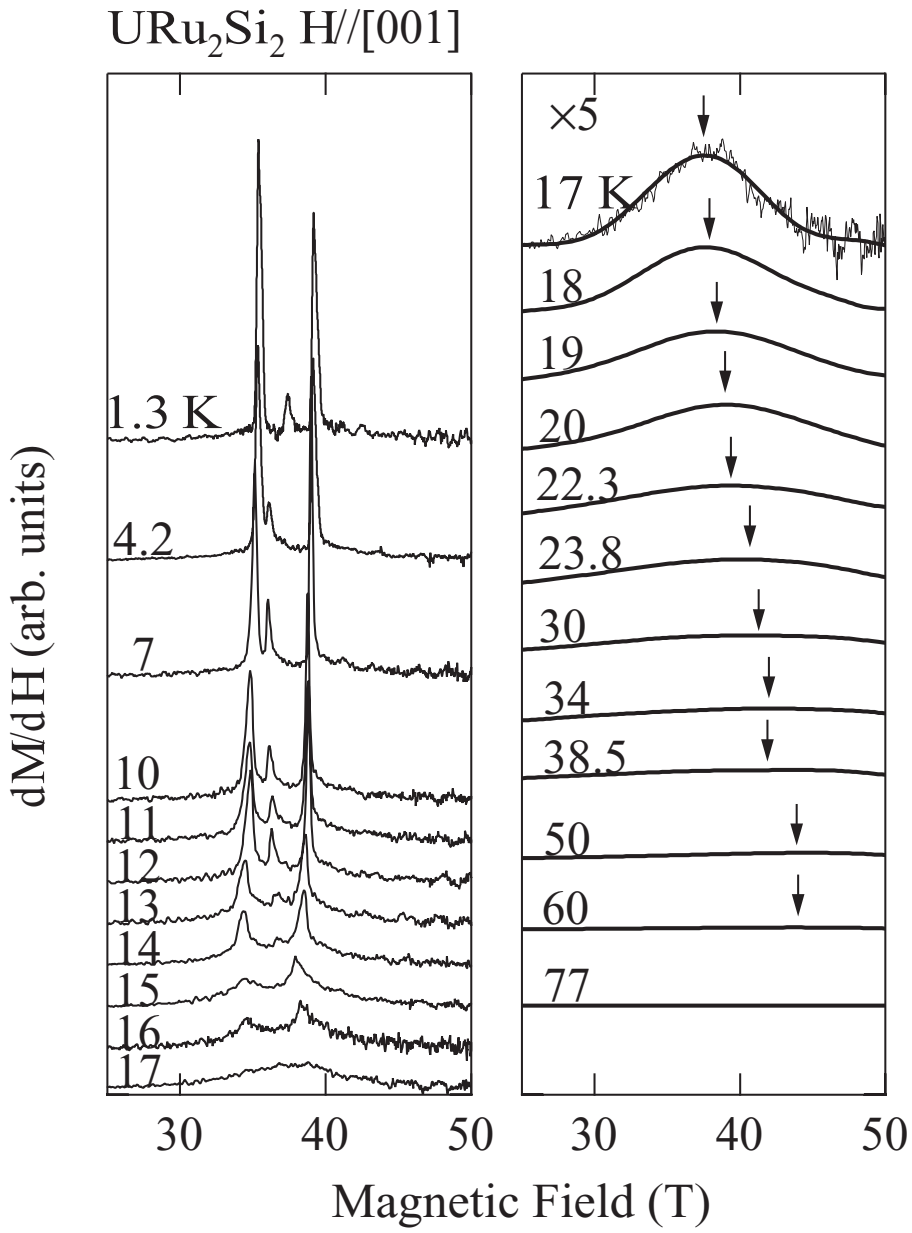

Fig. 4.51 dMdH curve at each tempreature with fitting curves in URu_2Si_2.

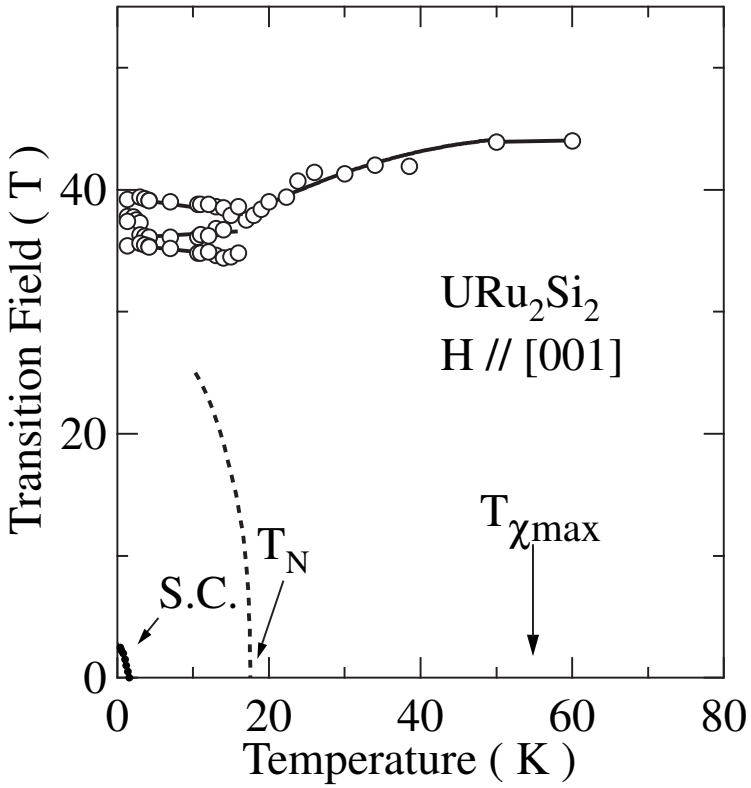

Fig. 4.52 Phase diagram of URu_2Si_2.

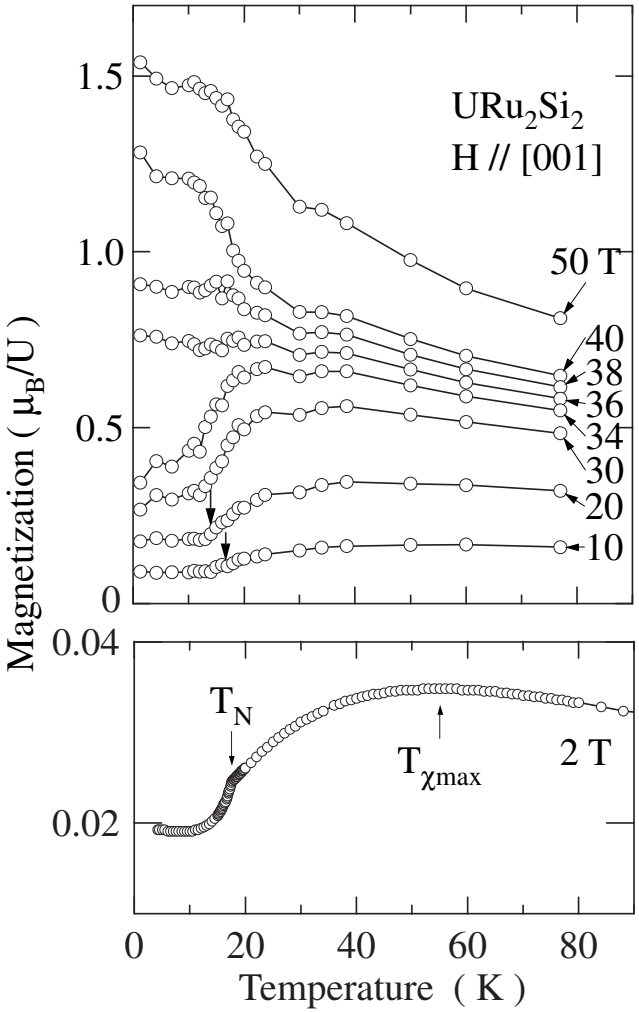

Fig. 4.53 Temperature dependence of the magnetization in URu_2Si_2 for the field along [001] below 80 K at various magnetic fields.

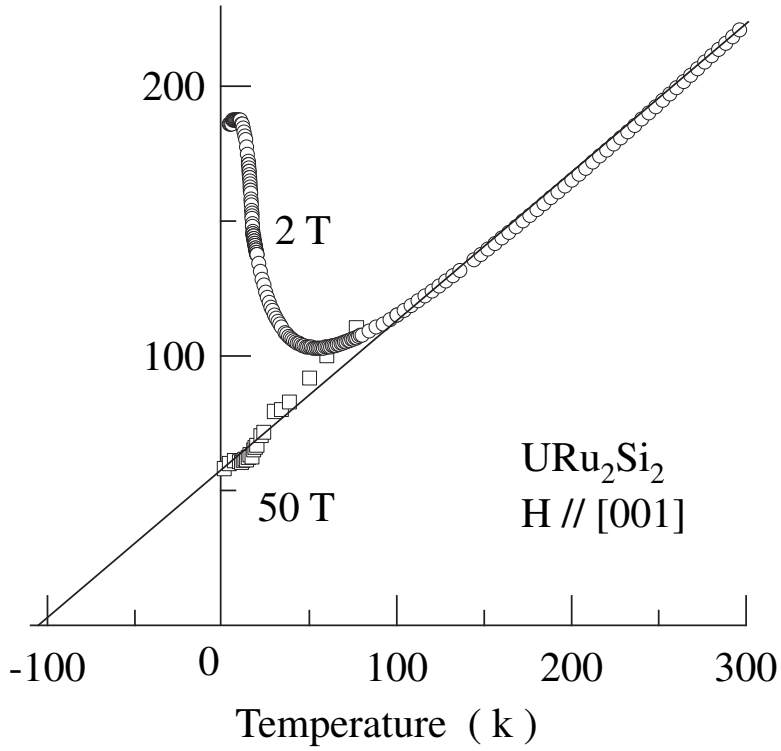

Fig. 4.54 Temperature dependence of the inverse magnetic susceptibility in URu_2Si_2. The data at 2 and 50 T are shown by circles and squares, respectively. A thick solid line shows the Curie-Weiss law.

We also studied the metamagnetic transitionof UPt_3 at various temperatures as shown in Fig. 4.55. Figure. 4.56 shows the the differential magnetization (dM/dH) curves at each temperature. The observed metamagnetic transition is broad even below $T_N \simeq$ 5 K and it persists up to about 30 K, which is close to the characteristic temperature $T_{\chi max}$ ($\simeq$ 20 K). This is in contrast with the URu_2Si_2 behavior, where the metamagnetic transition is sharp below T_N and becomes broad above T_N. This result indicates that the antiferromagnetically ordered state in UPt_3 is different from those of URu_2Si_2. That is to say, there is no static ordering but dynamic spin fluctuations are dominant in UPt_3.

The metamagnetic tarnsition is thus one of the important characteristics in the heavy fermion compounds such as URu_2Si_2 and UPt_3. It is based on the hybridization effect between the conduction electrons with a wide energy band and almost localized f-electrons. As a consequence, the almost localized f-electrons become itinerant with decreasing temperature through the many-body Kondo effect. The crossover from localized to itinerant occurs at a characteristivc tempretaure $T_{\chi max}$, where the magnetic susceptibity has a maximum, as mentioned above. $T_{\chi max}$ corresponds approximately to the Kondo temperature T_K. At temperatures lower than $T_{\chi max}$, the metamagnetic transition occurs at a magnetic field H_m such that $k_B T \simeq g_{eff}\mu_B H_m$. Figure 4.58 shows the relation of H_m versus $T_{\chi max}$ in cerium and uranium compounds, where the data of URu_2Si_2 and UPt_3 are shown by large circles.

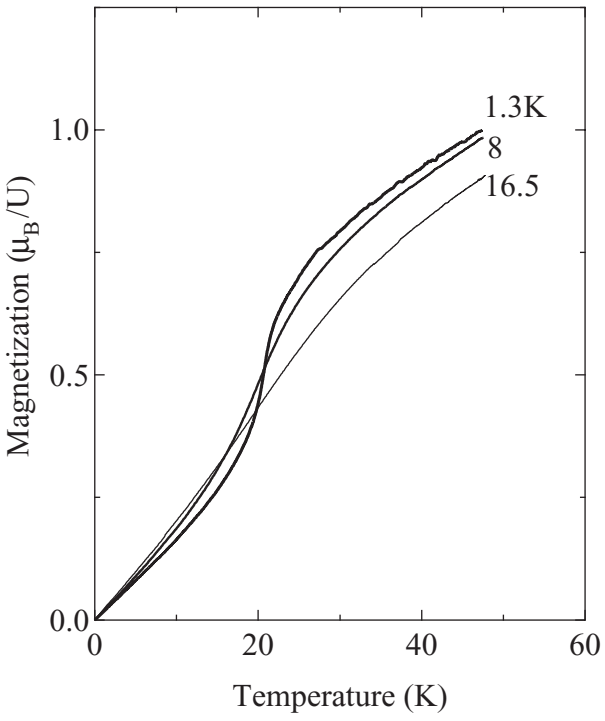

Fig. 4.55 Typical magnetization curves of UPt_3 at 1.3, 8 and 16.5 K.

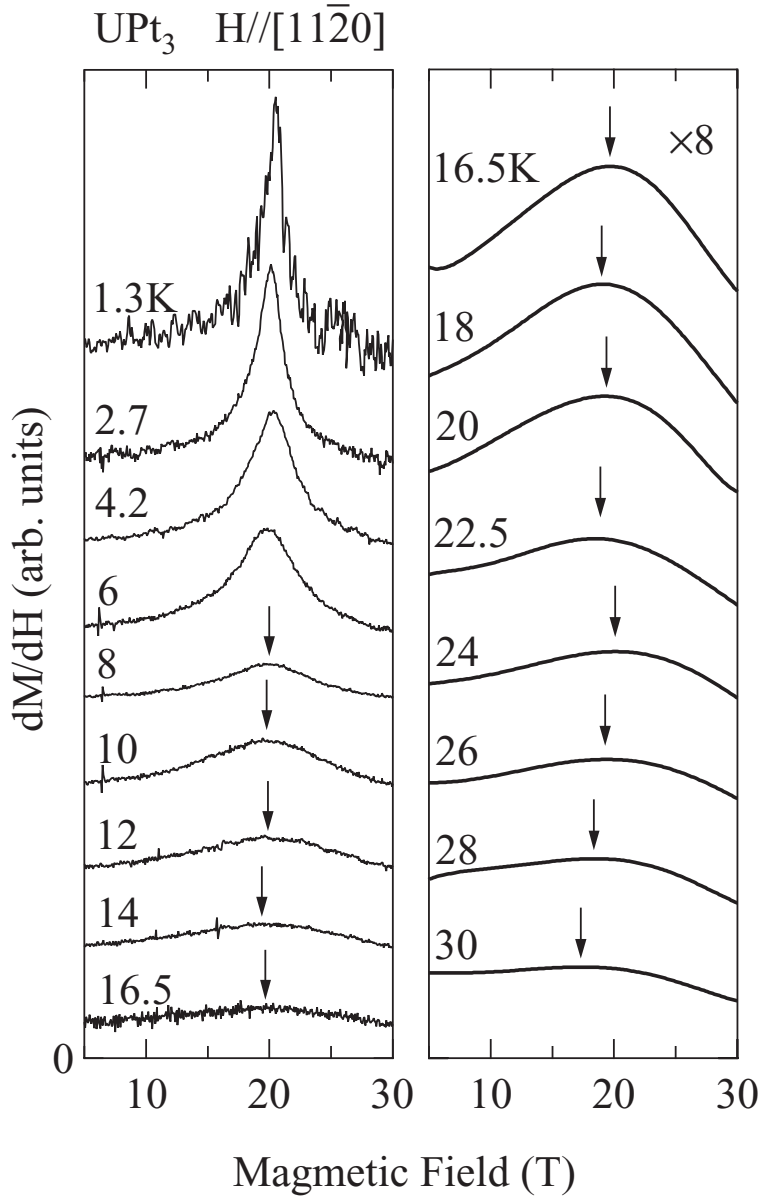

Fig. 4.56 *dMdH* curves at several tempreatures in UPt_3.

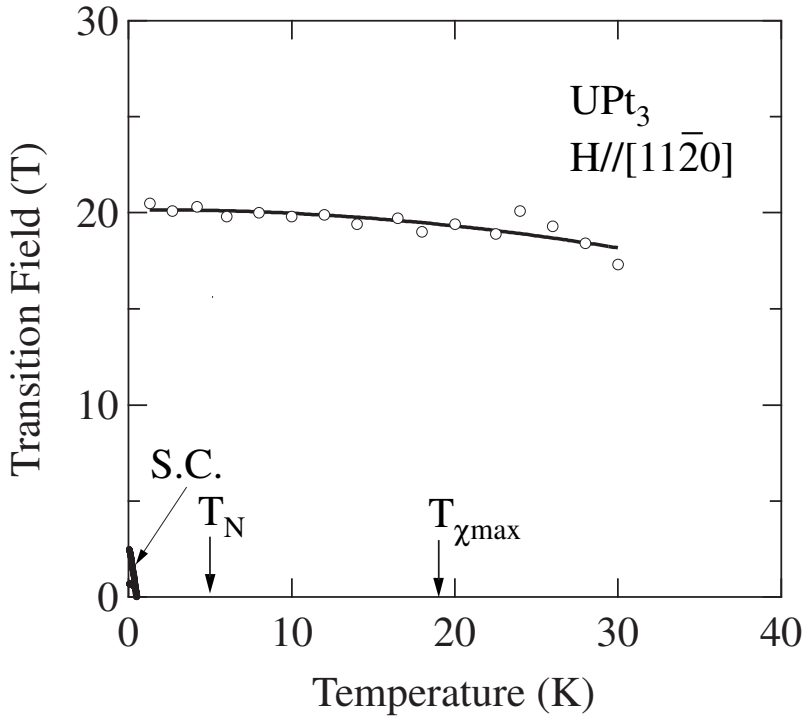

Fig. 4.57 Phase diagram of UPt_3.

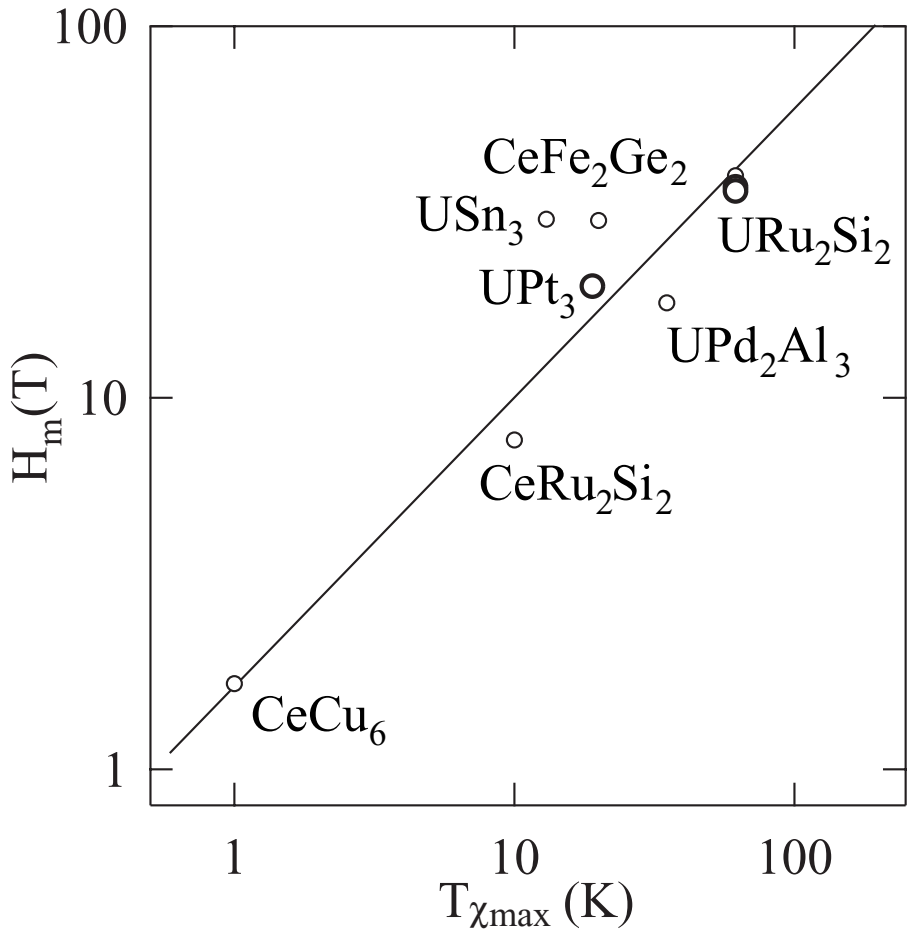

Fig. 4.58 H_{m} versus $T_{\chi\mathrm{max}}$ in heavy fermions of cerium and uranium compounds.

5 Conclusion

In the present study we have measured the electrical resistivity, dHvA effect and magnetization in cerium and uranium compounds under high pressure. The present experimental results are summarized as follows:

$CeNiGe_3$

We have measured the electrical resistivity of an antiferromagnet $CeNiGe_3$ up to 8.0 GPa in the temperature range of 2 to 300 K.

1) T_N increases with increasing pressure, has a maximum at 3.7 GPa, decreases with furthur increasing pressure above 3.7 GPa, and becomes zero around 5.5 GPa ($\simeq P_c$).

2) The residual resistivity ρ_0 and the A value of the resistivity $\rho = \rho_0 + AT^2$ has a maximum around P_c. The characteristic temperauture, corresponding to the maximum ρ-value, has a minimum around P_c.

These experimental results indicate that the antiferromagnet $CeNiGe_3$ with a f-localized nature is changed into a non-magnetic $4f$-itinerant compound, passing through the heavy fermion state at a critical pressure $P_c \simeq 5.5$ GPa. The crossover from localized to itinerant is tuned by applying pressure.

$CeNi_2Al_5$

We have measured the electrical resistivity of an antiferromagnet $CeNi_2Al_5$ up to 7.0 GPa in the temperature range of 2 to 300 K.

1) T_N increases with increasing pressure, has a maximum at 3.9 GPa, decreases with further increasing pressure above 3.9 GPa, and becomes zero around 6.0 GPa ($= P_c$).

2) The overall behavior is similar to that of $CeNiGe_3$.

$CeAgSb_2$

We have measured the electrical resistivity of a ferromagnet $CeAgSb_2$ up to 4.2 GPa in the temperature range of 0.1 to 300 K.

1) T_C decreases with increasing pressure. The critical pressure P_c was determined at $P_c \simeq 3.3$ GPa.

2) When the pressure crosses P_c, a huge residual resistivity was observed, changing from 1.0 $\mu\Omega$·cm at P_c=2.6 GPa to 55 $\mu\Omega$·cm at P_c. The electronic state is changed into another one with a different character above P_c.

$UNiGa_5$

We have measured the electrical resistivity of an antiferromagnet $UNiGa_5$ up to 8.0 GPa in the temperature range of 2 to 300 K.

1) T_N decreases with increasing pressure. The critical pressure P_c was determined at $P_c \simeq 4.5\,\mathrm{GPa}$.

2) Around P_c, the A value of the resistivity $\rho = \rho_0 + AT^2$ has a maximum.

T_N becomes zero above $P_c \simeq 4.5$ GPa. This phenomenon is similar to that of the antiferromagnetic cerium compounds such as $CeNiGe_3$. The temperature dependence of the electrical resistivity is , however, highly different between $UNiGa_5$ and $CeNiGe_3$. In $UNiGa_5$, the resistivity above P_c increases almost linearly with increasing temperature. On the other hand, the resistivity has a clear peak in $CeNiGe_3$, although the peak moves to higher temperatures with increasing pressures.

$UPdGa_5$

We have measured the electrical resistivity of an antiferromagnet $UPdGa_5$ up to 5.0 GPa in the temperature range of 2 to 300 K.

1) T_N decreases with increasing pressure. The critical pressure was determined at $P_c \simeq 3.2\,\mathrm{GPa}$.

2) Around P_c, the A value of the resistivity $\rho = \rho_0 + AT^2$ has a maximum.

$UPtGa_5$

We have measured the electrical resistivity of an antiferromagnet $UPtGa_5$ up to 8.5 GPa in the temperature range of 2 to 300 K.

1) T_N decreases with increasing pressure. The critical pressure P_c was determined at $P_c \simeq 8.0\,\mathrm{GPa}$.

2) The A value and ρ_0 values are unchanged against pressure. These are different from those of $UNiGa_5$ and $UPdGa_5$.

UN

We have measured the electrical resistivity of an antiferromagnet UN up to 7.0 GPa in the temperature range of 2 to 300 K.

1) T_N decreases with increasing pressure. The critical pressure P_c was determined at $P_c \simeq 3.0\,\mathrm{GPa}$.

2) The A value has a maximum at 2 GPa below P_c.

UGa_3

We have measured the electrical resistivity of an antiferromagnet UGa_3 up to 8.5 GPa, in the temperature range of 2 to 300 K.

1) T_N decreases with increasing pressure. The critical pressure P_c was determined at $P_c \simeq 2.6\,\mathrm{GPa}$.

2) The A value has a maximum at 2 GPa below P_c.

URu_2Si_2

We have measured the dHvA effect of URu_2Si_2 up to 2 GPa.

1) The detected dHvA frequency increases monotonously with increasing pressure and indicates no abrupt change at $P_c = 1.5$ GPa.

2) The cyclotron mass decreases considerably with increasing pressure and also indicates no abrupt change at P_c.

The present dHvA experiment under pressure is thus inconsistent with the phase-separated proposal based on the NMR experiment.

Next, we have measured the high-field magnetization of URu_2Si_2 up to 50 T in a wide temperature range of 1.3 to 77 K.

3) The sharp metamagnetic transition with three-steps is observed from the lowest measured temperature of 1.3 K to 14 K, which is close to the Néel temperature of 17.5 K.

4) The sharp metamagnetic transition is changed from three steps to two steps above 14 K. The metamagnetic transition with the two steps is observed in a very narrow temperature range from 14 to 16 K.

5) Above the Néel temperature of 17.5 K, the metamagnetic transition is changed into one broad peak, which is observed up to 60 K.

6) The inverse susceptibility χ^{-1} ($= H/M$), where M is the magnetization at $H =$ 50 T, is connected continuously with the usual inverse susceptibility obtained at 2 T. This indicates that the metamagnetic transition is a change of the $5f$-electronic state from itinerant to localized.

UPt_3

We have also measured the high-field magnetization of UPt_3 up to 50 T in a wide temperature range of 1.3 to 77 K.

1) The observed metamagnetic transition is broad even below $T_N \simeq 5$ K and it persists up to about 30 K, which is close to the characteristic temperature $T_{\chi max}$ ($\simeq$ 20 K). This result is different from those of URu_2Si_2, and indicates that there is no static ordering in UPt_3 but dynamic spin fluctuations are dominant in a strongly correlated compound of UPt_3.

The metamagnetic transition occurs at a critical field H_m, holding a relation of $k_B T \simeq g_{\rm eff}\mu_B H_m$. This relation is satisfied in heavy fermion compounds including URu_2Si_2 and UPt_3 The crossover from itinerant to localized is thus tuned by applying high magnetic fields.

Acknowledgments

I would like to express my sincere gratitude to Prof. Yoshichika Ōnuki for the guidance to physics, and helpful supports and suggestions for the present research. I would also like to express my sincere gratitude to Prof. Kiyohiro Sugiyama, Prof. Rikio Settai, Dr. Yoshinori Haga, Dr. Yoshihiko Inada, Dr. Tetsuya Takeuchi and Dr. Arumugam Thamizhavel for advice and experimental supports.

The present research was performed by various experimental methods, especially high-pressure experiments. Among them, many experiments were performed by the cubic anvil cell and bridgeman anvil cell at Institute for Solid State Physics, University of Tokyo (ISSP). I am grateful to Prof. Nobuo Môri and Prof. Yoshiya Uwatoko for providing these pressure apparatus and advising for the experimental technique. I am grateful to Dr. Masato Hedo for his help and advice throughout the study at ISSP. I am also grateful to Dr. Nao Takeshita and Dr. Takeshi Nakanishi for advice on high-pressure technique and measurements.

I also grateful to Prof. Tatsuo C. Kobayashi for valuable advice and providing the indenter cell, which was another important method of high-pressure in the present study.

The measurements of the magnetization were performed at Research Center for Materials Science at Extreme Conditions, Osaka University. I am grateful to Prof. Koichi Kindo for the measurements.

Uranium compounds were provided from Japan Atomic Energy Research Institute. I am grateful to Dr. Tatsuma D. Matsuda, Dr. Yoshihumi Tokiwa, Dr. Etsuji Yamamoto and Mr. Shugo Ikeda for sample preparation and fruitful discussions.

It was extremely difficult for me to carry out the dHvA experiments under pressure. Deep appreciation should be directed to Dr. Shingo Araki for his help and valuable advice on this measurement.

I also thank to Mr. Ryoichi Koki, Mr. Hiroaki Shishido, Mr. Hirokazu Nakawaki, Mr. Rihito Asai, Mr. Shingo Kirita, and other friends in Ōnuki group in Graduate School of Science, Osaka University for their helpful assistance and discussion.

I wish to express my thanks to Dr. Osamu Shimoe and other friends in Hitachi Metals, Ltd., who encouraged me to take a doctor course. I would like to thank my family for their support and encouragement.

References

1) Y. Ōnuki, T. Goto, and T. Kasuya, Materials Science and Technology **3A**, 545 (1991).

2) S. Doniach, Physica B & C **91**, 231 (1977).

3) N. D. Mathur, F. M. Grosche, S. R. Julian, I. R. Walker, D. M. Freye, R. K. W. Haselwimmer, and G. G. Lonzarich, Nature **394**, 39 (1998).

4) D. Jaccard, K. Behnia, and J. Sierro, Phys. Lett. A **163**, 475 (1992).

5) H. Hegger, H. G. Moshopoulou, M. F. Hundley, J. L. Sarmo, Z. Fisk, and J. D. Thompson, Phys. Rev. Lett. **84**, 4986 (2000).

6) S. S. Saxena, P. Agarwal, K. Ahilan, F. M. Grosche, R. K. W. Haselwimmer, M. J. Steiner, E. Pugh, I. Walker, S. Julian, and et Monthoux, Nature **406**, 587 (2000).

7) N. Tateiwa, T. C. Kobayashi, K. Hanazono, K. Amaya, Y. Haga, R. Settai, and Y. Ōnuki, J. Phys. Condens. Matt. **13**, 475 (2001).

8) Y. Ōnuki and A. Hasegawa, in *Handbook on the Physics and Chemistry of Rare Earths*, edited by J. K. A. Gschneidner and L. Eyring (North-Holland, Amsterdam, 1995), Vol. 20, p. 1.

9) M. A. Ruderman and C. Kittel, Phys. Rev. **96**, 99 (1954).

10) T. Kasuya, Prog. Theor. Phys. **16**, 45 (1956).

11) K. Yosida, Phys. Rev. **106**, 893 (1957).

12) J. Kondo, Prog. Theor. Phys. **32**, 37 (1964).

13) K. H. J. Buschow, H. J. van Daal, F. E. Maranzana, and P. B. van Aken, Phys. Rev. B **3**, 1662 (1971).

14) A. Sumiyama, Y. Oda, H. Nagano, Y. Ōnuki, K. Shibutani, and T. Komatsubara, J. Phys. Soc. Jpn. **55**, 1294 (1986).

15) K. Yamada, K. Yosida, and K. Hanzawa, Prog. Theor. Phys. **71**, 450 (1984).

16) K. Yamada and K. Yosida, Prog. Theor. Phys. **76**, 621 (1986).

17) K. Satoh, T. Fujita, Y. Maeno, Y. Ōnuki, and T. Komatsubara, J. Phys. Soc. Jpn. **58**, 1012 (1989).

18) H. Aoki, S. Uji, A. K. Albessard, and Y. Ōnuki, J. Phys. Soc. Jpn. **61**, 3457 (1992).

19) H. Aoki, S. Uji, A. K. Albessard, and Y. Ōnuki, Phys. Rev. Lett. **71**, 2110 (1993).

20) C. D. Bredl, J. Magn. Magn. Mater. **63-64**, 355 (1987).

21) J. Etourneau, J.-P. Mercurio, R. Naslain, and P. Hagenmuller, J. Solid State Chem. **2**, 332 (1970).

22) G. R. Stewart, Rev. Mod. Phys. **56**, 755 (1984).

23) K. Kadowaki and S. B. Woods, Solid State Commun. **58**, 507 (1986).

24) P. A. Lee, T. M. Rice, J. W. Serene, L. J. Sham, and J. W. Wilkins, Comments Condens. Matter Phys. **12**, 99 (1986).

25) K. Miyake, T. Matsuura, and C. M. Varma, Solid State Commun. **71**, 1149 (1989).

26) S. Doniach, in *Valence Instabilities and Related Narrow-Band Phenomena*, edited by R. D. Parks (Plenum, New York, 1977), p. 169.

27) N. B. Brandt and V. V. Moshchalkov, Adv. Phys. **33**, 373 (1984).

28) J. Rossat-Mignod, L. P. Regnault, J. L. Jacoud, C. Vettier, R. Lejay, J. Flouquet, E. Walker, D. Jaccard, and A. Amato, J. Magn. Magn. Mater. **76-77**, 376 (1988).

29) A. Schröder, H. G. Schlager, and H. v. Löhneysen, J. Magn. Magn. Mater. **108**, 47 (1992).

30) P. Haen, J. Flouquet, F. Lapierre, P. Lejay, and G. Remenyi, J. Low Temp. Phys. **67**, 391 (1987).

31) G. G. Lonzarich, J. Magn. Magn. Mater. **76-77**, 1 (1988).

32) Y. Ōnuki, I. Umehara, A. K. Albessard, T. Ebihara, and K. Satoh, J. Phys. Soc. Jpn. **61**, 960 (1992).

33) H. Yamagami and A. Hasegawa, J. Phys. Soc. Jpn. **62**, 592 (1993).

34) I. Umehara, Y. Kurosawa, N. Nagai, M. Kikuchi, K. Satoh, and Y. Ōnuki, J. Phys. Soc. Jpn. **59**, 2848 (1990).

35) A. Hasegawa, H. Yamagami, and H. Johbettoh, J. Phys. Soc. Jpn. **59**, 2457 (1990).

36) F. Steglich, J. Aarts, C. D. Bredl, W. Lieke, D. Meschede, and W. Franz, Phys. Rev. Lett. **43**, 1892 (1979).

37) R. Movshovich, T. Graf, D. Mandrus, M. F. Hundley, J. D. Thompson, R. A. Fisher, N. E. Phillips, and J. L. Smith, Physica B **223-224**, 126 (1996).

38) R. Movshovich, T. Graf, D. Mandrus, J. D. Thompson, J. L. Smith, and Z. Fisk, Phys. Rev. B **53**, 8241 (1996).

39) A. Das, L. Menon, A. K. Nigam, and S. K. Malik, Physica B **230-232**, 165 (1997).

40) P. Salamakha, M. Konyk, O. Sologub, and O. Bodak, J. Alloy. Compd. **236**, 206 (1996).

41) B. Chevalier and J. Etourneau, J. Magn. Magn. Mater. **196-197**, 880 (1999).

42) L. Durivault, E. Bouree, B. Chevalier, G. Andre, F. Weill, and J. Etourneau, Appl. Phys. A **74**, S677 (2002).

43) L. Durivault, F. Bouree, B. Chevalier, G. Andre, F. Weill, J. Etourneau, P. Martinez-Samper, J. Rodrigo, H. Suderow, and S. Vieira, J. Phys. Condens. Matter **15**, 77 (2003).

44) A. P. Pikul, D. Kaczorowski, T. Plackowski, A. Czopnik, H. Michor, E. Bauer, G. Hilscher, P. Rogl, and Y. Grin, Phys. Rev. B **67**, 224417 (2003).

45) O. S. Zarechnyuk, T. I. Yanson, and R. M. Rykhal', Russian Metallurgy 192 (1983).

46) E. Parthé and B. Chabot, in *Handbook on the Physics and Chemistry of Rare Earths*, edited by K. G. Jr and L. Eyring (North-Holland, Amsterdam, 1984), Vol. 6, p. 113.

47) Y. Isikawa, T. Mizushima, J. Sakurai, K. Mori, A. Monoz, F. Givord, J. X. Boucherle, J. Voiron, I. Oliveira, and J. Flouquet, J. Phys. Soc. Jpn. **63**, 2349 (1994).

48) J. X. Boucherle, P. Burlet, F. Givord, Y. Isikawa, R. Neudert, D. Schmitt, and H. Schober, J. Phys. Condens. Matter **7**, 8337 (1995).

49) F. Givord, J. X. Boucherle, and Y. Isikawa, J. Phys. Soc. Jpn. Suppl.B **65**, 129 (1996).

50) F. Givord, J. X. Boucherle, J. Dreyer, Y. Isikawa, B. Ouladdiaf, S. Pujol, J. Schweizer, and F. Tasset, J. Phys. Condens. Matter **11**, 7327 (1999).

51) Y. Isikawa, T. Mizushima, K. Oyabe, K. Mori, K. Sato, and K. Kamigaki, J. Phys. Soc. Jpn. **60**, 1869 (1991).

52) D. Kaczorowski, R. Kruk, J. Sanchez, B. Malaman, and F. Wastin, Phys. Rev. B **58**, 9227 (1998).

53) M. Brylak, M. H. Moller, and W. Jeitschko, J. Solid State Chem. **115**, 305 (1995).

54) K. D. Myers, S. L. Bud'ko, I. R. Fisher, Z. Islam, H. Kleinke, A. H. Lacerda, and P. C. Canfield, J. Magn. Magn. Mater. **205**, 27 (1999).

55) G. Andre, F. Bouree, M. Kolenda, B. Lesniewska, A. Oles, and A. Szytula, Physica B **292**, 176 (2000).

56) K. D. Myers, S. L. Budko, V. P. Antropov, B. N. Harmon, P. C. Canfield, and A. H. Lacerda, Phys. Rev. B **60**, 13371 (1999).

57) Y. Muro, N. Takeda, and M. Ishikawa, J. Alloy. Compd. **257**, 23 (1997).

58) M. Houshiar, D. T. Adroja, and B. D. Rainford, J. Magn. Magn. Mater. **140-144**, 1231 (1995).

59) Y. Tokiwa, Y. Haga, N. Metoki, Y. Ishii, and Y. Ōnuki, J. Phys. Soc. Jpn. **71**, 725 (2002).

60) S. Ikeda, N. Metoki, Y. Haga, K. Kaneko, T. D. Matsuda, A. Galatanu, and Y. Ōnuki, J. Phys. Soc. Jpn. **72**, 2622 (2003).

61) Y. Tokiwa, Y. Haga, E. Yamamoto, D. Aoki, N. Watanabe, R. Settai, T. Inoue, K. Kindo, H. Harima, and Y. Ōnuki, J. Phys. Soc. Jpn. **70**, 1744 (2001).

62) Y. Tokiwa, S. Ikeda, Y. Haga, T. Okubo, T. Iizuka, K. Sugiyama, A. Nakamura, and Y. Ōnuki, J. Phys. Soc. Jpn. **71**, 845 (2002).

63) S. Ikeda, Y. Tokiwa, Y. Haga, E. Yamamoto, T. Okubo, M. Yamada, N. Nakamura, K. Sugiyama, K. Kindo, Y. Inada, H. Yamagami, and Y. Ōnuki, J. Phys. Soc. Jpn. **72**, 576 (2003).

64) N. A. Curry, Proc. Phys. Soc. **86**, 1193 (1965).

65) P. de V. du Plessis and C. F. V. Doorn, Physica B & C **86-88**, 993 (1977).

66) J. M. Fournier, J. Beille, and C. H. de Novion, Journal de Physique Colloque **40**, C4/32 (1979).

67) J. M. Fournier, J. Beille, A. Boeuf, C. Vettier, and A. Wedgwood, Physica B & C **102**, 282 (1980).

68) D. Kaczorowski, R. Troc, D. Badurski, A. Bohm, L. Shlyk, and F. Steglich, Phys. Rev. B **48**, 16425 (1993).

69) D. Kaczorowski, R. Hauser, and A. Czopnik, Physica B **230-232**, 35 (1997).

70) A. Murasik, J. Leciejewicz, S. Ligenza, and A. Zygmunt, Physica Status Solidi A **23**, K147 (1974).

71) A. C. Lawson, A. Williams, J. L. Smith, P. A. Seeger, J. A. Goldstone, J. A. O'Rourke, and Z. Fisk, J. Magn. Magn. Mater. **50**, 83 (1985).

72) D. Aoki, N. Suzuki, K. Miyake, Y. Inada, R. Settai, K. Sugiyama, E. Yamamoto, Y. Haga, Y. Ōnuki, T. Inoue, K. Kindo, H. Sugawara, H. Sato, and H. Yamagami, J. Phys. Soc. Jpn. **70**, 538 (2001).

73) C. Broholm, H. Lin, P. T. Matthews, T. E. Mason, W. J. L. Buyers, M. F. Collins, A. A. Menovsky, J. A. Mydosh, and J. K. Kjems, Phys. Rev. B **43**, 12809 (1991).

74) H. Ohkuni, Y. Inada, Y. Tokiwa, K. Sakurai, R. Settai, T. Honma, Y. Haga, E. Yamamoto, Y. Ōnuki, H. Yamagami, S. Takahashi, and T. Yanagisawa, Philos. Mag. B **79**, 1045 (1999).

75) K. Sugiyama, H. Fuke, K. Kindo, K. Shimohata, A. A. Menovsky, J. A. Mydosh, and M. Date, J. Phys. Soc. Jpn. **59**, 3331 (1990).

76) H. Amitsuka, M. Sato, N. Metoki, M. Yokoyama, K. Kuwahara, T. Sakakibara, H. Morimoto, S. Kawarazaki, Y. Miyako, and J. A. Mydosh, Phys. Rev. Lett. **83**, 5114 (1999).

77) K. Matsuda, Y. Kohori, T. Kohara, K. Kitwahara, and H. Amitsuka, Phys. Rev. Lett. **87**, 087203/1 (2001).

78) G. Motoyama, Y. Ushida, T. Nishioka, and N. K. Sato, Physica B **329-333**, 528 (2003).

79) P. Chandra, P. Coleman, J. A. Mydosh, and V. Tripathi, Nature **417**, 831 (2002).

80) P. Chandra, P. Coleman, and J. A. Mydosh, Physica B **312-313**, 397 (2002).

81) K. Matsuda, Y. Kohori, T. Kohara, H. Amitsuka, and T. Matsumoto, Physica B **312-313**, 504 (2002).

82) G. Motoyama, T. Nishioka, and N. K. Sato, Phys. Rev. Lett. **90**, 166402/1 (2003).

83) H. Tou, Y. Kitaoka, I. Asayama, N. Kimura, Y. Ōnuki, E. Yamamoto, and K. Maezawa, Czechoslovak Journal of Physics **46**, 779 (1996).

84) H. Tou, Y. Kitaoka, K. Ishida, K. Asayama, N. Kimura, Y. Ōnuki, E. Yamamoto, Y. Haga, and K. Maezawa, Phys. Rev. Lett. **80**, 3129 (1998).

85) G. Aeppli, E. Bucher, C. Broholm, J. K. Kjems, J. Baumann, and J. Hufnagl, Phys. Rev. Lett. **60**, 615 (1988).

86) P. H. Frings, J. J. M. Franse, F. R. de Boer, and A. Menovsky, J. Magn. Magn. Mater. **31-34**, 240 (1983).

87) Y. Koike, N. Metoki, N. Kimura, E. Yamamoto, Y. Haga, Y. Ōnuki, and K. Maezawa, Jpn. J. Appl. Phys. **series11**, 44 (1983).

88) N. Môri, T. Nakanishi, M. Ohashi, N. Takeshita, H. Goto, S. Yomo, and Y. Okayama, Physica B **265**, 263 (1999).

89) Y. Ōnuki, T. Goto, and T. Kasuya, in *Materials Science and Technology*, edited by K. H. J. Buschow (VCH, Weinheim, 1992), Vol. 3A, p. 545.

90) W. Assmus, M. Herrmann, U. Rauchschwalbe, S. Riegel, W. Lieke, H. Spille, S. Horn, G. Weber, F. Steglich, and G. Cordier, Phys. Rev. Lett. **52**, 469 (1984).

91) S. Araki, R. Settai, Y. Inada, Y. Ōnuki, and H. Yamagami, J. Phys. Soc. Jpn. **68**, 3334 (1999).

92) M. Nakashima, K. Tabata, A. Thamizhavel, T. C. Kobayashi, M. Hedo, Y. Uwatoko, K. Shimizu, R. Settai, and Y. Ōnuki, J. Phys. Condens. Matter **16**, L255 (2004).

93) H. Shishido, R. Settai, D. Aoki, S. Ikeda, H. Nakawaki, T. Takeuchi, T. C. Kobayashi, Y. Haga, H. Harima, Y. Aoki, T. Namiki, H. Sato, and Y. Ōnuki, J. Phys. Soc. Jpn. **71**, 162 (2002).

94) K. Miyake and H. Maebashi, J. Phys. Soc. Jpn. **71**, 1007 (2002).

95) D. Jaccard, E. Vargoz, K. Alami-Yadri, and H. Wilhelm, Rev. High Pressure Sci. Technol. **7**, 412 (1998).

96) T. Muramatsu, N. Tateiwa, T. C. Kobayashi, K. Shimizu, K. Amaya, D. Aoki, H. Shishido, Y. Haga, and Y. Ōnuki, J. Phys. Soc. Jpn. **70**, 3362 (2001).

97) F. M. Grosche, S. R. Julian, N. D. Mathur, and G. G. Lonzarich, Physica B **223-224**, 50 (1996).

98) D. Jaccard, A. Link, E. Vargoz, and K. Alami-Yadri, Physica B **230-232**, 297 (1997).

99) K. Miyake, O. Narikiyo, and Y. Onishi, Physica B **259-261**, 676 (1999).

100) O. Sakai, in *Physics of Strongly Correlated Electron Systems*, edited by T. Komatsubara, H. Fujii, Y. Ōnuki, and H. Shiba (JJAP, Tokyo, 1999), Vol. 11, p. 141.

101) H. Löhneysen, F. Huster, S. Mock, A. Neuvert, T. Pietrus, M. Sieck, O. Stockert, and M. Waffenschmidt, Physica B **230-232**, 550 (1997).

102) T. Moriya and T. Takimoto, J. Phys. Soc. Jpn. **64**, 960 (1995).

103) S. Kambe, S. Raymond, and L. P. Regnault, J. Phys. Soc. Jpn. **65**, 3294 (1996).

104) M. Hatatani, O. Narikiyo, and K. Miyake, J. Phys. Soc. Jpn. **67**, 4002 (1998).

Publication List

1) **M. Nakashima**, K. Tabata, A. Thamizhavel,T. C. Kobayashi, M. Hedo, Y. Uwatoko, K. Shimizu, R. Settai, and Y. Ōnuki
High-pressure effect on the electronic state in $CeNiGe_3$: pressure-induced superconductivity,
J. Phys. Condens. Matter **16**, L255 (2004).

2) **M. Nakashima**, H. Ohkuni, Y. Inada, R. Settai, Y. Haga, E. Yamamoto, and Y. Ōnuki,
The de Haas-van Alphen effect in URu_2Si_2 under pressure,
J. Phys. Condens. Matter **15**, S2011 (2003).

3) **M. Nakashima**, Y. Haga, E. Yamamoto, Y. Tokiwa, M. Hedo, Y Uwatoko, R. Settai, and Y. Ōnuki,
The high-pressure effect of an electronic state in uranium compounds: $UPtGa_5$ and UN,
J. Phys. Condens. Matter **15**, S2007 (2003).

4) **M. Nakashima**, S. Ikeda, T. Okubo, R. Settai, H. Ohkuni, E. Yamamoto, Y. Haga, and Y. Ōnuki,
De Haas-van Alphen effect under pressure in URu_2Si_2,
Physica B **329-333**, 566 (2003).

5) **M. Nakashima**, S. Kirita, R. Asai, T.C. Kobayashi, T. Okubo, M. Yamada, A. Thamizhavel, Y. Inada, R. Settai, A. Galatanu, E. Yamamoto, T. Ebihara, and Y. Ōnuki,
Huge residual resistivity in the quantum critical region of $CeAgSb_2$,
J. Phys. Condens. Matter **15**, L111 (2003).

6) S. Araki, **M. Nakashima**, R. Settai, T.C. Kobayashi, and Y. Ōnuki,
Superconductivity in $CeRh_2Si_2$ under pressure,
Act. Phys. Pol. B **34**, 439 (2003).

7) Y. Ōnuki, R. Settai, S. Araki, **M. Nakashima**, H. Ohkuni, H. Shishido, A. Thamizhavel, Y. Inada, Y. Haga, E. Yamamoto, and T.C. Kobayashi,
De Haas-van Alphen experiments in the quantum critical region of cerium and uranium compounds,
Act. Phys. Pol. B **34**, 667 (2003).

8) R. Settai, **M. Nakashima**, H. Shishido, Y. Haga, H. Yamagami, and Y. Ōnuki,
De Haas-van Alphen experiments under pressure in UGe_2,
Act. Phys. Pol. B **34**, 725 (2003).

9) **M. Nakashima**, Y. Tokiwa, H. Nakawaki, Y. Haga, Y. Uwatoko, R. Settai, and Y. Ōnuki,

Single crystal growth and the high-pressure effect of an electronic state in $UNiGa_5$, *J. Nucl. Sci. Technol.* **Supple. 3**, 214 (2002).

10) S. Araki, **M. Nakashima**, R. Settai, T.C. Kobayashi, and Y. Ōnuki,
Pressure-induced superconductivity in an antiferromagnet $CeRh_2Si_2$,
J. Phys. Condens. Matter **14**, L377 (2002).

11) S. Araki, R. Settai, **M. Nakashima**, H. Shishido, S. Ikeda, H. Nakawaki, Y. Haga, N. Tateiwa, T.C. Kobayashi, H. Harima, H. Yamagami, Y. Aoki, T. Namiki, H. Sato, and Y. Ōnuki,
Heavy fermions in cerium and uranium compounds studied by the de Haas-van Alphen experiment,
J. Phys. Chem. Solids **63**, 1133 (2002).

12) R. Settai, H. Shishido, S. Ikeda, **M. Nakashima**, D. Aoki, Y. Haga, H. Harima, and Y. Ōnuki,
Scattering rate of quasiparticles both in the normal and superconducting mixed states in $CeCoIn_5$ studied by the dHvA effect,
Physica B **312-313**, 123 (2002).

13) S. Araki, **M. Nakashima**, H. Nakawaki, R. Settai, H. Harima, and Y. Ōnuki,
De Haas-van Alphen effect in $CeRh_2Si_2$ under pressure,
Physica B **312-313**, 435 (2002).

14) Y. Haga, **M. Nakashima**, R. Settai, S. Ikeda, T. Okubo, S. Araki, T.C. Kobayashi, N. Tateiwa, and Y. Ōnuki,
A change of the Fermi surface across the metamagnetic transition under pressure in UGe_2,
J. Phys. Condens. Matter **14**, L125 (2002).

15) R. Settai, **M. Nakashima**, S. Araki, Y. Haga, T.C. Kobayashi, N. Tateiwa, H. Yamagami, and Y. Ōnuki,
A change of the Fermi surface in UGe_2 across the critical pressure,
J. Phys. Condens. Matter **14**, L29 (2002).

16) S. Ikeda, H. Shishido, **M. Nakashima**, R. Settai, D. Aoki, Y. Haga, H. Harima, Y. Aoki, T. Namiki, H. Sato, and Y. Ōnuki,
Unconventional superconductivity in $CeCoIn_5$ studied by the specific heat and magnetization measurements,
J. Phys. Soc. Jpn. **70**, 2248 (2001).

17) R. Settai, H. Shishido, S. Ikeda, Y. Murakawa, **M. Nakashima**, D. Aoki, Y. Haga, H. Harima, and Y. Ōnuki,
Quasi-two-dimensional Fermi surfaces and the de Haas-van Alphen oscillation in both the normal and superconducting mixed states of $CeCoIn_5$,
J. Phys. Condens. Matter **13**, L627 (2001).

18) Y. Tokiwa, K. Sugiyama, T. Takeuchi, **M. Nakashima**, R. Settai, Y. Inada, Y. Haga, E. Yamamoto, K. Kindo, H. Harima, and Y. Ōnuki,
Quadrupolar phase diagram and Fermi surface properties in the localized 5f-electron system UPd_3,
J. Phys. Soc. Jpn. **70**, 1731 (2001).

19) **M. Nakashima**, Y. Haga, F. Honda, T. Eto, G. Oomi, T. Kagayama, N. Takeshita, T. Nakanishi, N. Mori, D. Aoki, R. Settai, and Y. Ōnuki,
Non-Fermi-liquid behaviour around the magnetic quantum critical point in UGa_3,
J. Phys. Condens. Matter **13**, L569 (2001).

20) K. Sugiyama, **M. Nakashima**, M. Futoh, H. Ohkuni, T. Inoue, K. Kindo, N. Kimura, E. Yamamoto, Y. Haga, T. Honma, R. Settai, and Y. Ōnuki,
Metamagnetism of uranium heavy-fermion compounds UPd_2Al_3, URu_2Si_2 and UPt_3,
Physica B **281-282**, 244 (2000).

21) Y. Tokiwa, K. Sugiyama, T. Takeuchi, R. Settai, Y. Inada, Y. Haga, E. Yamamoto, T. Honma, K. Sakurai, **M. Nakashima**, K. Miyake, K. Kindo, and Y. Ōnuki,
Quadrupolar ordering and de Haas-van Alphen effect in UPd_3,
Physica B **281-282**, 604 (2000).

22) K. Sugiyama, **M. Nakashima**, H. Ohkuni, K. Kindo, Y. Haga, T. Honma, E. Yamamoto, and Y. Ōnuki,
Metamagnetic transition in a heavy fermion superconductor URu_2Si_2,
J. Phys. Soc. Jpn. **68**, 3394 (1999).

23) K. Sugiyama, **M. Nakashima**, D. Aoki, K. Kindo, N. Kimura, H. Aoki, T. Komatsubara, S. Uji, Y. Haga, E. Yamamoto, H. Harima, and Y. Ōnuki,
Metamagnetic transition in UPt_3 studied by high-field magnetization and de Haas-van Alphen experiments,
Physical Review B (Condensed Matter) **60**, 9248 (1999).

24) K. Sugiyama, **M. Nakashima**, Y. Yoshida, R. Settai, T. Takeuchi, K. Kindo, and Y. Ōnuki,
Metamagnetic transitions based on the quadrupole moment in RCu_2 single crystals,
Physica B **259-261**, 896 (1999).

25) K. Sugiyama, **M. Nakashima**, Y. Yoshida, Y. Kimura, K. Kindo, T. Takeuchi, R. Settai, and Y. Ōnuki,
High-field magnetization in $TbCu_2$ and $HoCu_2$ single crystals,
J. Phys. Soc. Jpn. **67**, 3244 (1998).

26) K. Sugiyama, **M. Nakashima**, A. Koyanagi, S. Araki, E. Kindo, T. Hata, R. Settai, and Y. Ōnuki,
High-field magnetization of $PrCu_6$ and $PrNi_5$ with the singlet ground state,
J. Phys. Soc. Jpn. **67**, 2553 (1998).